Modeling, Analysis, and Measurement of Passenger Vehicle Stability

by

Steven C. Peters

B.S., Mechanical Engineering
University of California, Davis 2004

Submitted to the Department of Mechanical Engineering
In Partial Fulfillment of the Requirements for the Degree of
Master of Science in Mechanical Engineering

at the

Massachusetts Institute of Technology

September 2006

Signature of Author.....
Department of Mechanical Engineering
August 15, 2006

Certified by.....
Karl Iagnemma
Principal Research Scientist
Thesis Supervisor

Accepted by.....
Professor Lallit Anand
Chairman, Committee on Graduate Studies

Modeling, Analysis, and Measurement of Passenger Vehicle Stability

by

Steven C. Peters

Submitted to the Department of Mechanical Engineering
On August 15, 2006, in Partial Fulfillment of the
Requirements for the Degree of
Master of Science in Mechanical Engineering

Abstract:

Vehicle rollover represents a significant percentage of single-vehicle accidents and accounts for over 9,000 fatalities and over 200,000 non-fatal injuries each year. Previous automotive research has studied ways for detecting and mitigating rollover on flat ground at high speed, and robotics research has studied the rollover stability of robots on rough terrain at low speed. Accident statistics show, however, that over 80% of rollovers occur when a vehicle departs the roadway and encounters sloped and rough terrain at high speed. This thesis investigates the stability limits imposed by off-road terrain conditions and techniques for measuring vehicle stability in the presence of off-road terrain factors.

An analysis of the effects of terrain slope, roughness, and deformability on vehicle rollover stability in road departure scenarios is presented. A simple model that captures the first-order effects of each of these terrain features is presented and used to compare the relative danger posed by each factor.

A new stability measure is developed that is valid in off-road conditions, which include sloped, rough, and deformable terrain. The measure is based on the distribution of wheel-terrain contact forces and is measurable with practical sensors. The measure is compared to existing stability measures and is able to detect wheel lift-off with greater accuracy in off-road conditions. The measure is experimentally validated with wheel lift-off detection as well. An uncertainty analysis of the measure is presented that assesses the relative importance of each sensor and parameter in the measure.

Thesis Supervisor: Karl Iagnemma
Title: Principal Research Scientist

ACKNOWLEDGEMENTS

I would like to thank Karl and Dr. D for their guidance in this research and choosing me for this project. Special thanks to Yoji, Sauro, and Jim Bobrow for their technical advice while visiting the lab and all the members of FSRL who have assisted me and put up with my antics. I would also like to thank my family and friends for supporting me in this adventure.

TABLE OF CONTENTS

1

CHAPTER 1: INTRODUCTION

1.1 The problem: rollover is a dangerous instability

Navigation of high-speed mobile robots has received a significant amount of recent research activity, highlighted by the interest in DARPA's Grand Challenge autonomous vehicle race [10]. Applications of high-speed robots include exploration, reconnaissance, and material delivery. These systems are designed to operate on natural terrain that may be sloped, slippery, deformable, and uneven. Unfortunately, these systems are susceptible to rollover, particularly while performing severe maneuvers. Despite the fact that many systems are designed with rugged chassis (and some are designed to be invertible), rollover accidents often disable the robot and/or damage its payload. Rollover accidents have been reported in the literature and have been experienced by this thesis's author during field experiments.

In addition to autonomous vehicles, rollover poses a danger to manned vehicles, which constitute an important mode of transportation in this country for people and cargo over short and long distances. A significant amount of research and testing effort over the past 40 years has been expended to improve the safety of vehicles, and significant gains have been made. Nevertheless, in 2004 more than 40,000 people were killed and 2.5 million injured in motor vehicle accidents at an estimated cost of $200 billion [35]. Of these accidents, rollover is particularly fatal, accounting for over 10% of traffic fatalities in 2004, while only constituting 2.3% of accidents. It trailed only head-on

collisions and collisions with pedestrians in fatality rate, as shown in Table 1.

Crash Type	Percent total accidents	Percent total fatalities	Ratio
Pedestrian collision	1.1%	11.3%	10.3
Head-on collision	1.9%	10.8%	5.7
Rollover	2.3%	10.6%	4.6

Table 1: Fatality Rates of Most Dangerous Accidents [35]

Colliding with pedestrians, other vehicles, and fixed objects is clearly dangerous and undesirable at any speed. Prevention or mitigation of these accidents would require substantial perceptive and planning capability. This is being addressed by current research in autonomous vehicles [10]. Some rollover accidents also involve collision with moving or fixed objects, but many are caused by properties of the terrain surface being traversed, such as inclination or friction coefficient. Improved understanding of the stability limits imposed by terrain conditions can provide direction to vehicle design, road design, and control system development to prevent or mitigate rollover accidents.

1.2 Trends in rollover crash statistics

Previous study of rollover crashes has led to the definitions of two types of rollover accidents based on the physical mechanism causing the rollover. The first type, known as untripped rollover, occurs on flat terrain when large frictional tire forces cause the vehicle to overturn during severe maneuvers. The second type, known as tripped rollover, occurs when other interactions between the vehicle and terrain contribute to the accident, such as a curb impact or tires sinking into soft soil.

Although substantial effort has been expended to understand the vehicle design parameters contributing to untripped rollover [18, 51], to develop safety tests to evaluate untripped rollover stability [16, 17], and to develop stability control systems to prevent

untripped rollover [5, 7, 28, 36], much less research has been conducted on tripped rollover, particularly in stability control system development. Interestingly, tripped rollovers account for a much larger percentage of total rollovers than on-road untripped rollovers. An analysis of crash statistics found that 83% of single-vehicle passenger car rollovers in 1989 occurred off the roadway, implying some form of tripping [47].

The primary physical mechanism causing these rollovers was listed as the "tire-soil forces" that act on sideslopes and ditches and was listed for 81% of rural and 72% of urban rollovers respectively [48]. Additionally, 67% of the rollovers in the study of Illinois state data occurred in a rural setting and 33% in an urban setting.

Of vehicles that leave the road at some point in a rollover accident, 98% of the overturns were found to occur off the roadway. Only 2% reentered the roadway to overturn [48]. This speaks to the potential danger of road shoulders. Possible destabilizing mechanisms that were noted include terrain slope, changes in terrain slope, soil cover, and tire plowing in soft soil.

Further study by Viner found that 75% of rollovers on a slope involved a single edgeline crossing, while 25% exited and reentered the road once then departed on the opposite side where the accident occurred [49]. Additionally 71% of vehicles involved in rollover on a slope departed the road in a lateral skid, which indicates the driver had likely lost control of the vehicle prior to road departure.

Information on the type of rollover is also available in the NASS-CDS accident database, illustrated in Figure 1. Parenteau determined the rates of each type of accident for passenger and light truck vehicles, which are shown in Figure 2 [38]. The accident type corresponding to untripped rollover is defined as turn-over, while the other accident

types fall into the more general category of tripped rollover. The most common accident type appears to be the trip-over, accounting for over half of both passenger and light truck rollovers. A trip-over occurs when an obstacle suddenly stops the vehicle's lateral motion. Fall-over is the second most common, which may also occur in a road departure situation.

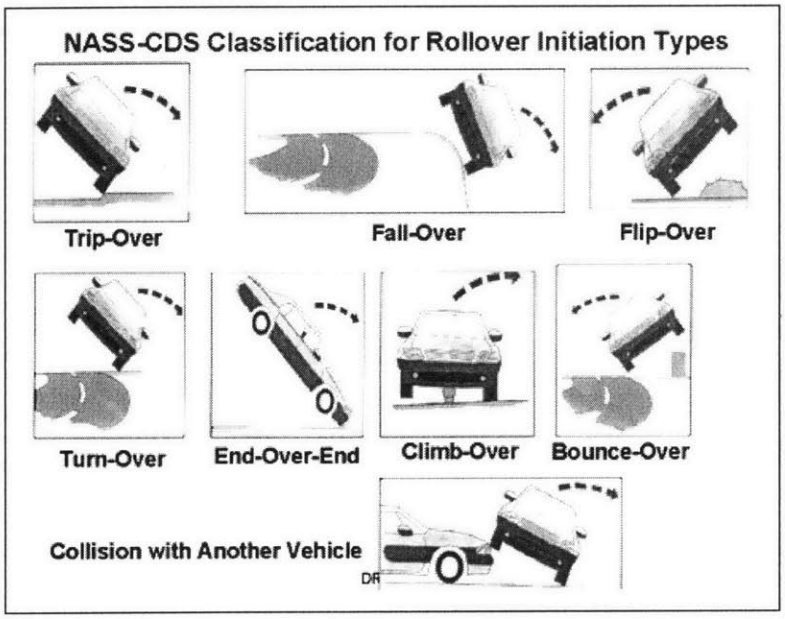

Figure 1: Types of Rollover Accidents [38]

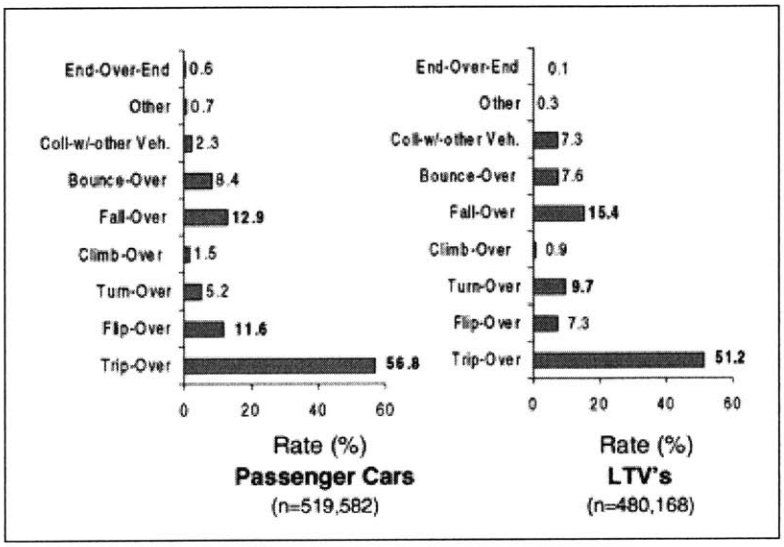

Figure 2: Rates of Each Type of Rollover [38]

Another study by Viano and Parenteau [46] focused on the scenarios leading to off-road rollovers. It examined a number of detailed accident case studies and proposed a new type of crash test to measure stability in road departure. Three dominant road departure rollover scenarios were found, illustrated in Figure 3. They include drifting off the road and rolling over on the shoulder; departing the roadway and recovering, only to depart the road on the opposite side and rollover there; and attempting to negotiate a curve at excessive speed, leading to road departure and rollover.

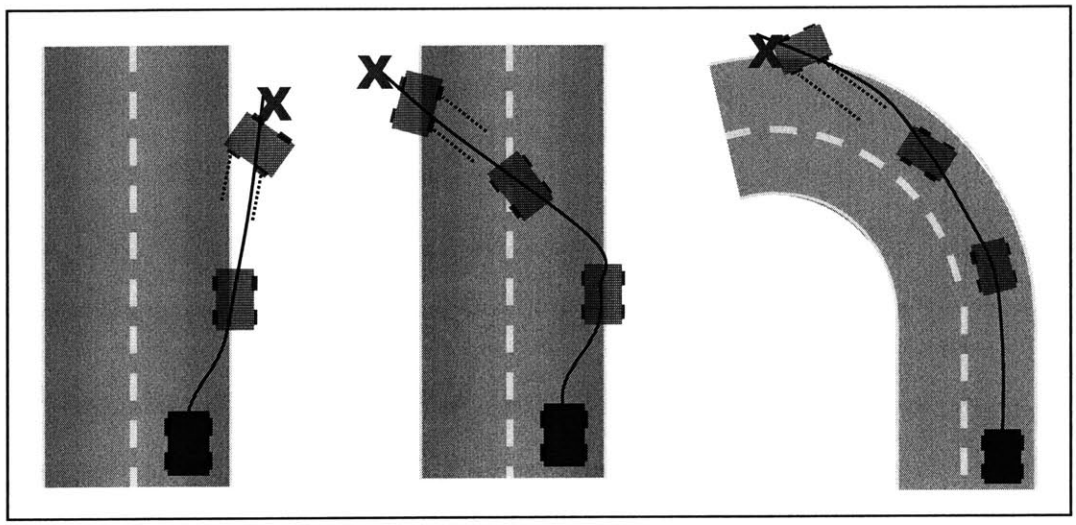

Figure 3: Common Road Departure Accident Scenarios [46]

Experimental testing of tripped rollovers has been conducted as well. Soil-tripped rollover tests were detailed in [9], which involved sliding a vehicle on a dolly laterally and releasing it onto soft soil. The minimum velocities needed to induce rollover were recorded as well as the distance traveled by the vehicle. A similar analysis was done for both soil and curb impacts at various angles of incidence with an experimentally validated computer model [14]. On average, the minimum velocity required to induce soil-tripped rollover was larger than the velocity required to induce curb-tripped rollover.

Garrott, et al. studied the effect of vehicle handling and design parameters on rollover rates in a statistical analysis of rollover and nonrollover accidents [18]. They attempted to find the handling and design parameters present in vehicles with high rates of rollover. For comparison, a number of non-vehicle accident parameters were included in the study, such as the location of the accident, age of driver, etc. Interestingly, the parameter with the strongest correspondence to high rates of rollover was not a vehicle design parameter, but the accident location, specifically whether the accident occurred in a rural setting. This agrees with Viner's findings in [48] mentioned above. The second strongest factor was the vehicle center of gravity (c.g.) position expressed as the Tilt Table Ratio, which is described in the next section.

1.3 Review of rollover stability measurement

During severe maneuvers, accurate monitoring of a vehicle's stability is important so that active control methods can be initiated to avoid loss of control and/or rollover. Many approaches for measuring the stability of mobile robots and vehicles have been developed in previous research. The stability measurement methods developed by automotive researchers are discussed in Section 1.3.1, and the methods developed by robotics researchers are discussed in Section 1.3.2.

1.3.1 Automotive research

The automotive community has studied the stability of high-speed wheeled vehicles on flat ground extensively. This has resulted in the definition of several categories of vehicle stability, including intrinsic stability and instantaneous stability. Measures of intrinsic stability relate the stability of a particular vehicle to alternative

designs of the same vehicle or different vehicles altogether. Measures of instantaneous stability concern the dynamic stability of a vehicle at a point in time during its operation. Instantaneous stability measures can be useful for online stability control systems if suitable sensors are available.

An extended NHTSA study on intrinsic stability led to the Federal rollover crash safety ratings, which are based on measurement of vehicle c.g. position and the results of high-speed aggressive maneuver tests, including the Fish Hook and Double Lane Change maneuver [16, 17]. The lateral velocity required to induce a curb-tripped or soil-tripped rollover measured in [9, 14] is another example of an intrinsic vehicle stability measure.

The measure of vehicle c.g. position used by the Federal rollover crash safety ratings is the Static Stability Factor (SSF), defined as the ratio between vehicle width and c.g. height. The SSF is computed with (1-1) and dimensions illustrated in the left portion of Figure 4. Larger values of the SSF imply greater stability.

$$SSF = \frac{TW}{2h} \tag{1-1}$$

A similar measure of c.g. position that considers the effect of suspension compliance is the Tilt-Table-Ratio (TTR), illustrated in the right portion of Figure 4. The name is drawn from the apparatus used to measure its value, a table that tilts the vehicle until its upper wheels lose contact with the ground. The measure is then defined as the slope of the table reached in the test. Note that the TTR of a rigid vehicle would be equal to its SSF, but most vehicles have suspension compliance that causes a measurable difference between the two values. Values of the SSF and TTR for production vehicles were measured by NHTSA and are publicly available [26].

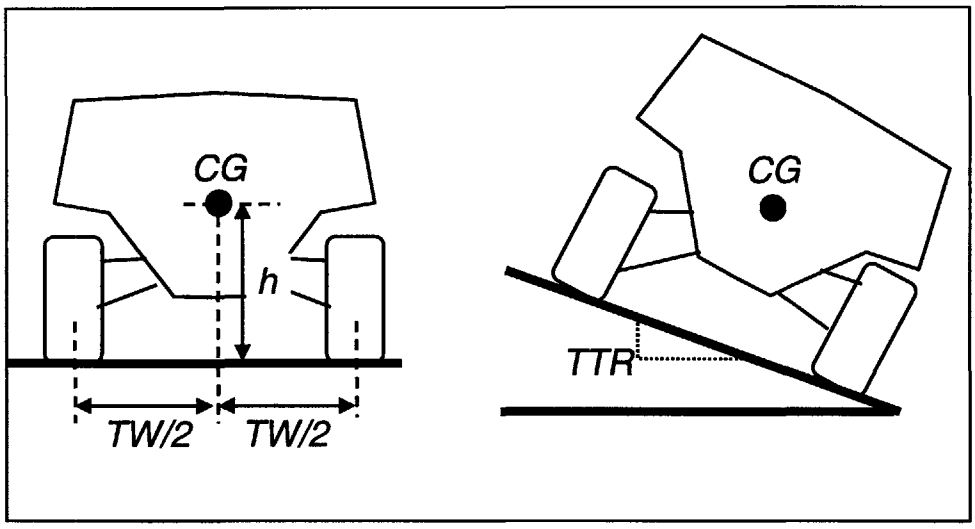

Figure 4: Measures of Vehicle Center of Gravity (c.g.)

Bernard provided a link between intrinsic and instantaneous stability measures in [2] by showing that the SSF corresponds approximately to the vehicle's critical lateral acceleration in g's, defined as the lateral acceleration of a maneuver on flat ground that causes wheel lift-off. The SSF neglects the effects of suspension compliance and other secondary factors. More accurate estimates of the critical lateral acceleration were provided by Bernard in [2] and later by Hac in [22]. A disadvantage of this measure is its dependence on the assumption of flat ground, since sloped terrain changes the critical lateral acceleration significantly.

Another group of instantaneous stability measures are based on the distribution of contact forces on the vehicle. The "load transfer metrics" quantify stability by the difference in tire normal forces acting on each side of the vehicle as computed in (1-2) and illustrated in Figure 5. Such a measure indicates the nearness to wheel lift-off on smooth terrain. Load transfer metrics have been used in a number of stability control systems [6, 7, 36]. In [7], forward simulations of a low-order linear model were used to

predict Time-To-Rollover, which was used as the basis of a control algorithm for rollover avoidance.

$$R = \frac{F_L - F_R}{F_L + F_R} \tag{1-2}$$

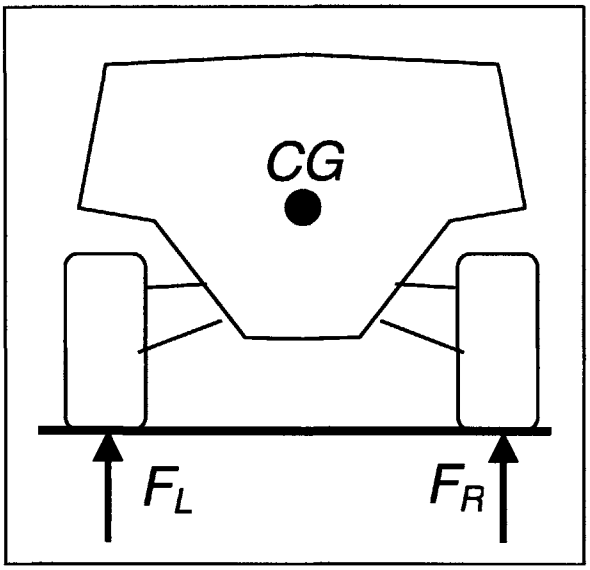

Figure 5: Contact forces in load transfer metric

An implicit property of rollover accidents is the large change in the roll angle of the vehicle. As such, some researchers have proposed to use the measured roll angle as an instantaneous stability measure [5, 23]. A critical roll angle can be defined that corresponds to wheel lift-off on flat ground, though this threshold changes for sloped terrain.

Another set of instantaneous stability measures is based on the energy of the vehicle. The tipover point is defined in Figure 6 as the point when the vehicle c.g. lies directly above the wheels. In this configuration, the vehicle has the maximum potential energy possible with wheels on the ground. Instability is defined as the point when the kinetic energy of the vehicle in a given state exceeds the potential energy required to reach tipover. Stability measures based on this principle were defined in [28, 34] that

consider only the kinetic energy stored in rotation about the vehicle roll axis. In [28] the measure was integrated into a stability control system.

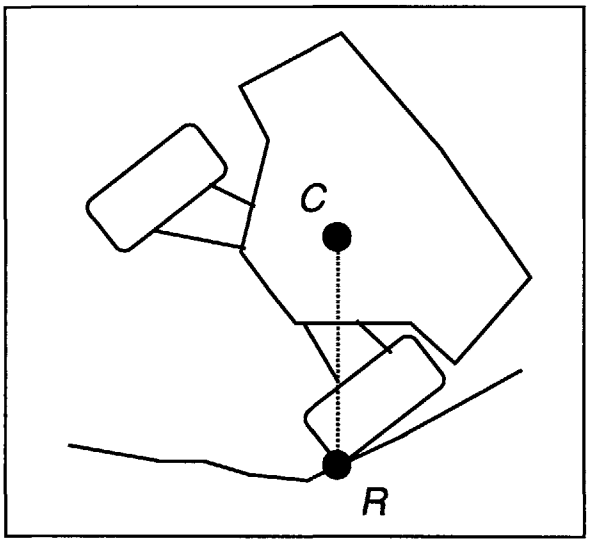

Figure 6: Tipover point

In summery, several stability measures have been developed in automotive research that are useful on flat ground at high speed, but they are not valid in the presence of terrain slope or roughness. This limits their applicability for measuring tripped rollover stability in road departure situations.

1.3.2 Robotics research

The robotics community has also studied the problem of tipover stability for mobile wheeled and legged robots on rough terrain, though usually at relatively low speed (cm/s).

Early methods by McGhee [32, 33] focused on measuring the instantaneous stability of a robot geometrically. A useful concept proposed is the stability polygon, which is formed by convex hull of terrain contact points projected onto a plane. If the projection of the vehicle c.g. onto that plane lies outside the polygon, the robot is deemed

unstable. Other similar work has not required a projection plane and made allowance for angular loads [11, 45]. This work is quasistatic and does not consider the effects of c.g. height.

Another approach to measuring the quasistatic stability of a robot that considers the effects of c.g. height is the Energy Stability Margin [31]. As the name implies, this measure is energy-based but is more general than the measures of [28, 34]. It utilizes the same concept of tipover point, shown in Figure 6, but on an arbitrary terrain surface.

The Energy Stability Margin was successfully applied to legged robots [50]. Subsequent work considered the effect of external inertial and manipulator loads [20]. While appropriate for low-speed vehicles, energy-based stability metrics are less useful for high-speed vehicles that are expected to operate at speeds that provide more than enough kinetic energy to cause a rollover.

Another instantaneous measure of dynamic robot stability, termed the force-angle stability measure, was proposed in [37]. A stability polygon is defined for the vehicle, drawing from previous work in robotics. Terrain contact forces acting at the nodes of the stability polygon are dubbed support forces, while the balance of forces acting on the system is deemed non-support forces. Non-support forces may include gravity, inertial force, and reactions from external manipulators. By transforming all non-support forces to the vehicle c.g. through force couples, a single resultant force can be found that is shown as $\mathbf{F}_c$ in Figure 7. The stability of the vehicle is defined by the direction of that force. If the line of action of $\mathbf{F}_c$ lies inside the stability polygon, as in the left portion of Figure 7, the robot is considered instantaneously stable. If the line of action points outside of the stability polygon as in the right portion of Figure 7, the robot is considered

instantaneously unstable, as a sustained application of the force in that direction would lead to a rollover. This metric has been applied to a number of robots, including interplanetary rovers [27], forestry vehicles with large manipulators [37], and a tall forklift [13].

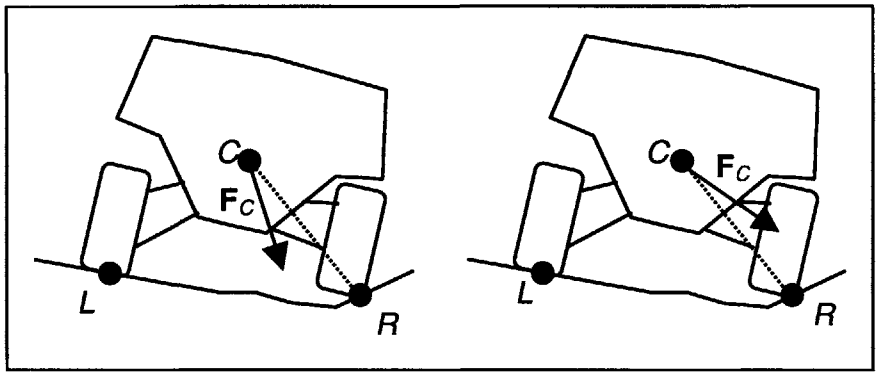

Figure 7: Force Angle Stability Measure

Prior work by this author has used a modified form of the force-angle stability measure to quantify the instantaneous stability of high-speed vehicles on rough terrain [39]. An extension of that work is presented in Chapter 3.

1.4 Sensing considerations for stability measurement

For practical reasons, it is important to consider the cost of sensors and the number of vehicle parameters required by an instantaneous stability measure. In Section 1.5.1, the practicality of measuring sensed quantities and estimating vehicle parameters is discussed. A set of practical sensors and vehicle parameters is defined. In Section 1.5.2, the practicality of the stability measures mentioned in the previous sections will be discussed.

1.4.1 Definition of practical sensors and vehicle parameters

In this discussion of stability measures, preference will be given to those that rely on physical quantities for which sensors are commercially available for low to moderate cost. Accelerometer output, angular velocity, wheel speed, and suspension displacement fit these requirements. Additionally, angular acceleration can be computed from angular velocity with appropriate filtering. Sensors are also commercially available for wheel contact forces but are prohibitively expensive. As such, accelerometers and sensors for angular velocity, wheel speed, suspension displacement, and angular acceleration will be considered reasonable for a stability measurement system.

Vehicle orientation, expressed as roll, pitch, and yaw angles, is more challenging to measure accurately. A simple method for measuring orientation is to use a compass for the yaw angle and an accelerometer for pitch and roll. For a non-accelerating vehicle, a body-fixed accelerometer measures the gravity vector, from which pitch and roll can be computed, but this is not appropriate for use during high-speed dynamic maneuvers. Estimates of pitch and roll can be made during dynamic maneuvers by fusing the accelerometer reading with measurements of angular velocity, though integration drift is a common problem with this approach. Increased accuracy can be obtained by fusing GPS position measurements or measuring orientation directly with multiple GPS antennas. While a number of systems that measure orientation in this manner are commercially available, they are complex and costly. It is not infeasible to use vehicle orientation in a stability measure, though preference is given to measures that use more practical sensors.

Many stability measures also require knowledge of vehicle c.g. position. This value can vary with changes in payload and fuel consumption. Isermann [19] developed an estimator of vehicle c.g. position based on a model of vehicle pitch dynamics. This estimator requires knowledge of suspension properties and suspension displacement sensors. Gerdes [42] developed a model-based estimator of c.g. position with knowledge of the suspension geometry and a measurement of roll angle from dual-GPS antennas. His method is also able to measure road slope. It will thus be assumed that vehicle c.g. position is available for stability measures.

1.4.2 Practicality of existing measurement techniques

In this section, the practicality of existing stability measures is discussed based on the discussion of practical sensors and parameters from the previous section.

In the previous section, accelerometer output, angular velocity, wheel speed, suspension displacement, and angular acceleration were deemed practical for use in stability measures, as well as estimates of c.g. position. Vehicle orientation is not infeasible to use, but preference is given to the other sensed quantities listed.

The critical lateral acceleration stability measure requires a single accelerometer and knowledge of vehicle c.g. position. It is attractive for its simplicity but is not valid in road departure. The critical roll angle and energy measure from [28] both require knowledge of body roll, which is more challenging to measure. Their dependence on the assumption of flat ground nullifies their validity in road departure situations however, and as such these stability measures will not be considered useful.

The load transfer stability measures are valid on sloped terrain, though they require knowledge of normal forces, which are not practical to measure directly with

force sensors. Several approaches have been proposed to estimate normal forces from vehicle models. Ray [40] used a vehicle pitch model to estimate normal forces at the front and rear of a vehicle, but did not consider the effects of side slope or lateral acceleration. Hahn, et al. [24] proposed the use of suspension spring force, damper force, and wheel mass acceleration, which requires significant calibration for the suspension parameters of each vehicle. Additionally, it neglects the effect of roll stabilizer bars, which are employed in many current passenger vehicles. An analysis of sensing considerations for this approach is given in Appendix E. Other work [36] has estimated the load transfer equation (1-2) directly with lateral acceleration, roll angle, and knowledge of suspension geometry. These quantities are more practical to obtain than contact force, but this model also is valid only on flat ground. Load transfer may be a useful stability measure, but a practical measurement approach has yet to be found.

The force-angle stability measure defined in [37] and its reformulation in [39] require knowledge of body forces and the position of the vehicle c.g. relative to the contact points. For vehicles with significant suspension travel, accurate stability measurement with these methods requires suspension displacement sensors. The exact location of the contact point on the wheel is not easily measurable, though it is bounded by the size of the wheel.

Most existing stability measures are challenging to measure on sloped and rough terrain, with the exception of the force-angle stability measure [37] and its reformulation [39].

1.5 Canonical vehicle maneuvers

To evaluate stability measurement techniques discussed throughout this thesis, several canonical high-speed maneuvers are defined. These include an aggressive maneuver on flat ground and on typical road profiles with sloped and rough shoulders. Simulations of a passenger utility vehicle executing these maneuvers were computed with an ADAMS vehicle model representative of a generic high-centered light truck. An isometric view of the model is shown in Figure 8. The model features a double wishbone suspension, passive roll stabilizer bars, rack and pinion steering, and a V8 engine. A summary of the vehicle parameters is given in Table 2, while more extensive information is provided in Appendix A.

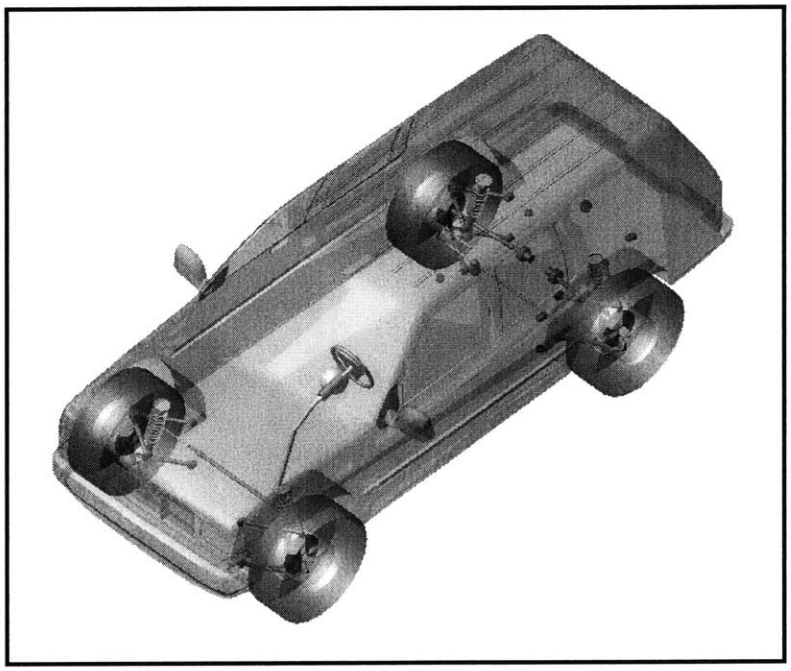

Figure 8: ADAMS Vehicle Model, Isometric View

Parameter	Value
Wheel base	2.85 m
Track width	1.62 m

Wheel diameter	0.79 m
Total mass	2450 kg
Wheel mass percent	10%
SSF	1.15
Suspension	Double wishbone

Table 2: ADAMS Model Parameters

Five canonical maneuvers are specified, which are summarized in Table 3. The aggressive maneuver chosen for these tests is the Fishhook maneuver, a standard governmental rollover test [16]. The maneuver requires an open-loop steering input detailed in Table 4 and no throttle or braking inputs. The steering input involves a step steer in one direction followed by a large countersteer in the opposite direction. The timing and amplitudes of the steering input are adjusted to coincide with the roll mode of the vehicle and accentuate the dynamic effect of the maneuver [16]. The test received its name from the similarity between a Fishhook and a typical trajectory of the vehicle, which can be seen in Figure 9 below.

Maneuver	Terrain	Roughness Standard Dev.	Initial speed	Result
1	Flat	0 mm	80 km/hr	Safe
2	Flat	0 mm	100 km/hr	Tip-up
3	Road departure	0 mm	100 km/hr	Rollover
4	Road departure	6.25 mm	100 km/hr	Rollover
5	Road departure	15 mm	100 km/hr	Rollover

Table 3: Canonical Maneuver Summary

Time	Steering input
0.0 s	0 deg
0.2 s	-60 deg

1.2 s	-60 deg
1.6 s	210 deg
5.6 s	210 deg

Table 4: Fishhook timing

Maneuver 1 is a Fishhook executed at 80 km/hr and illustrated in Figure 9. The road surface is flat with a friction coefficient of 1.0. Five points of interest during the maneuver are labeled A-E. Point A occurs at the beginning of the first steering input as the vehicle is driving straight, and point B occurs just before the countersteer as the vehicle is turning right. Points C, D, and E occur after countersteer as the vehicle turns left. This maneuver did not result in rollover.

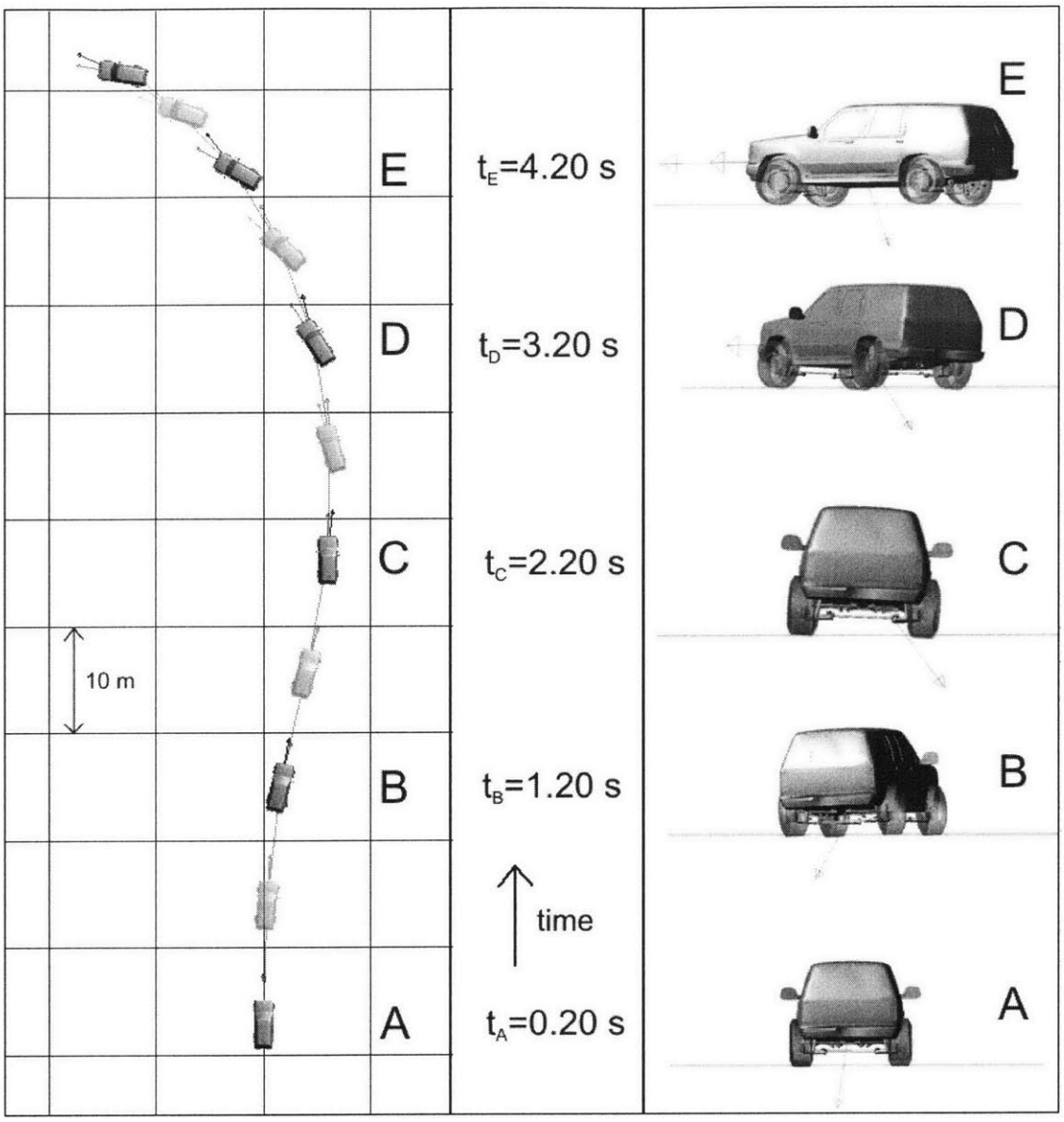

Figure 9: Maneuver 1 Safe on Flat Ground

Maneuver 2 is a Fishhook executed at 100 km/hr and illustrated in Figure 10. The road surface is flat with a friction coefficient of 2.0. Six points of interest during the maneuver are labeled A-F. Point A occurs as the vehicle is driving straight at the start of the maneuver. Points B and C occur as the vehicle is turning right, while D, E, and F occur after the counteresteer as the vehicle turns left. At point E the wheels lift-off the ground, but they return to the ground by point F and rollover does not occur.

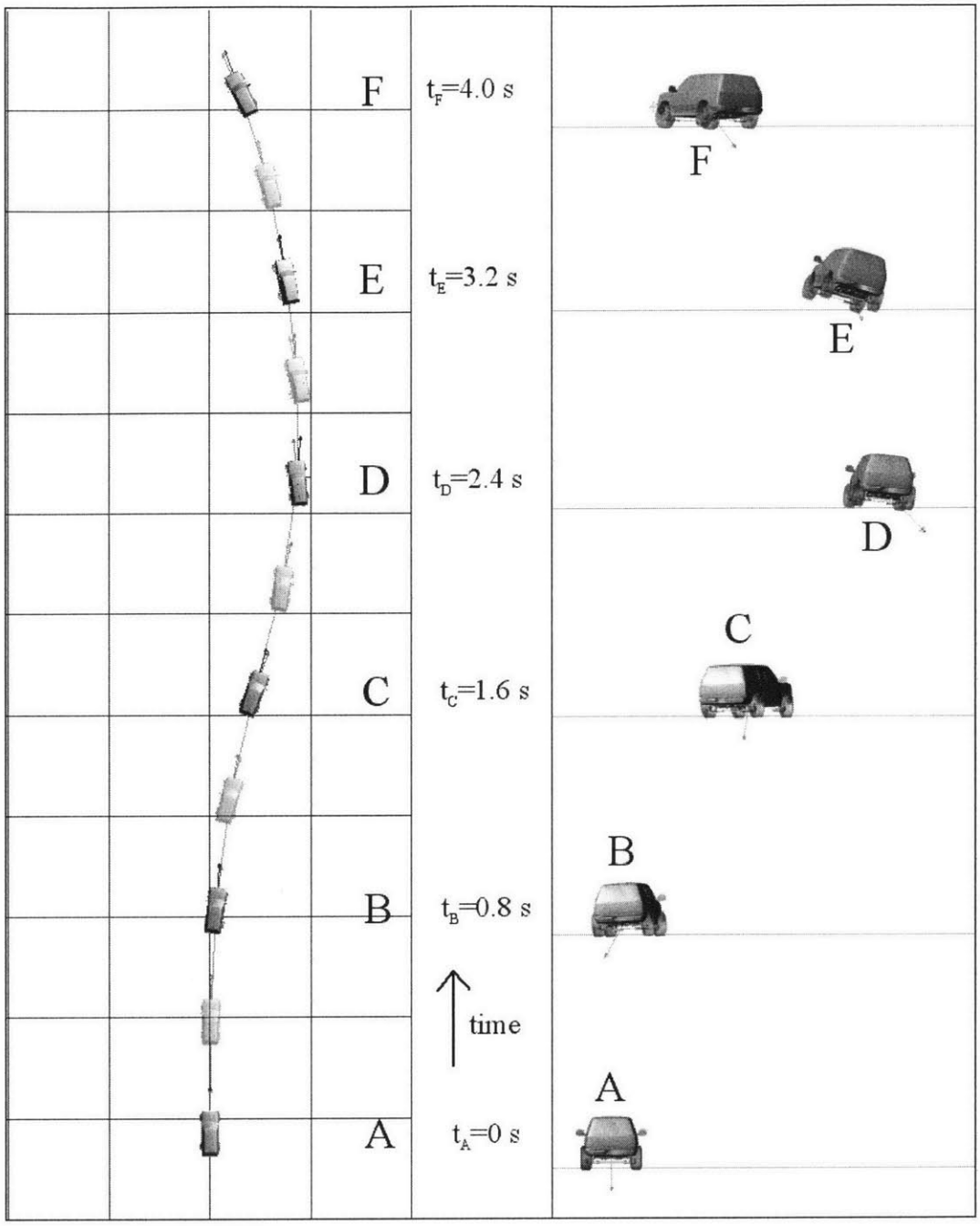

Figure 10: Maneuver 2 Tip-up on Flat Ground

Manuever 3 is a fishhook leading to road departure executed at 100 km/hr, illustrated in Figure 11. The road surface has a friction coefficient of 1.0, and the shoulder has a slope of 10 degrees, no roughness, and a friction coefficient of 2.0. The larger friction coefficient on the shoulder is intended to represent the effect of surface

deformability. Again, five points of interest are labeled A-E at one second intervals. Point A occurs at the beginning of the maneuver as the vehicle is driving straight on the road. Point B occurs during the first steer input as the vehicle turns right and is about to depart the roadway. Points C, D, and E occur during countersteer as the vehicle turns left in attempt to return to the road but proceeds to rollover.

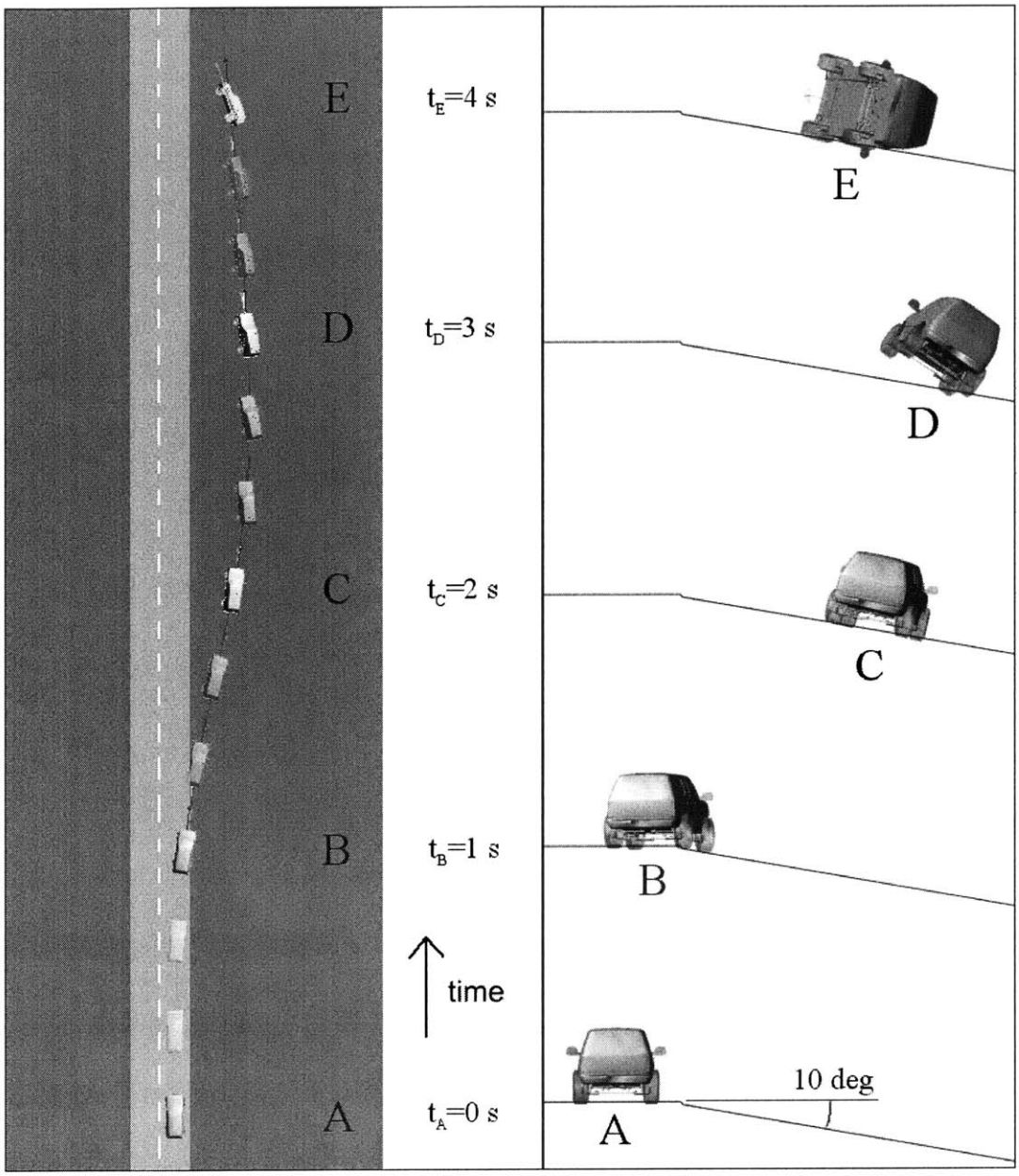

Figure 11: Maneuver 3 Rollover in Road Departure

Maneuvers 4 and 5 are fishhooks leading to road departure and rollover with roughness on the shoulder. As the trajectories of Maneuver 4 and 5 are very similar to that of Maneuver 3, they are not shown here. Roughness was superimposed onto the terrain profile used in the second maneuver, with a shoulder slope of 10 degrees and friction coefficient of 2.0. The shoulder surface was discretized into a triangular mesh of terrain patches, and Gaussian noise was added to the corner points of each triangular element. The discretization pattern is illustrated in Figure 12 with a node spacing of 600 mm in the x and y directions. Note that the wheel diameter is 790 mm. The variance of the roughness added was 6.25 mm^2 for Maneuver 4 and 15 mm^2 for Maneuver 5. The magnitude of this roughness in relation to the wheel diameter is illustrated in Figure 13.

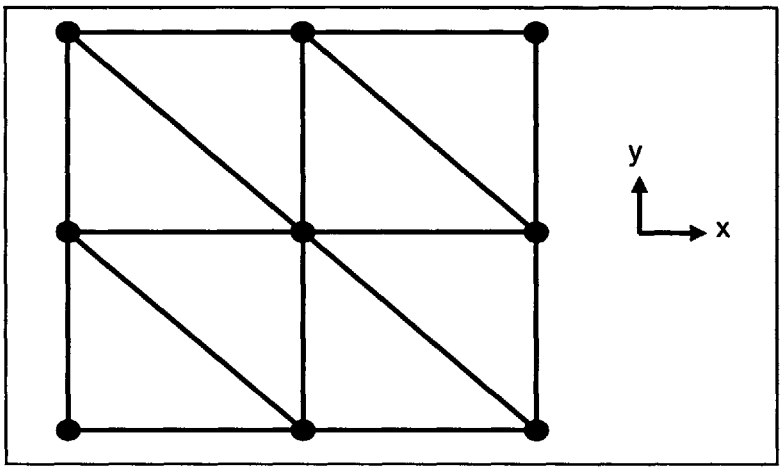

Figure 12: Grid discretization

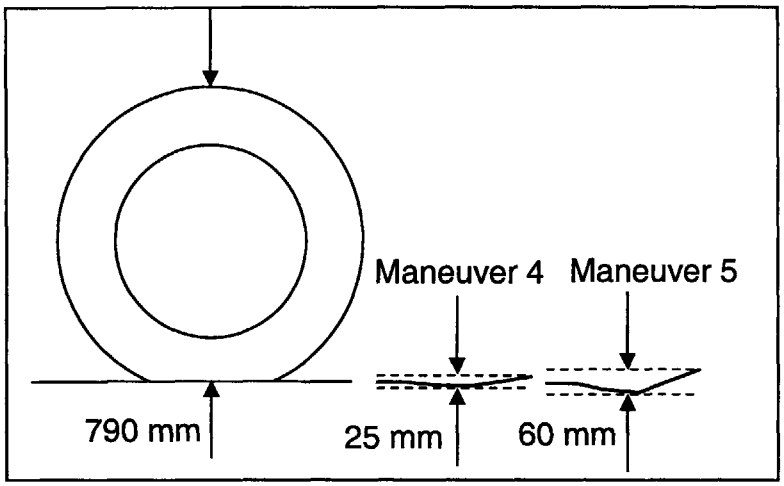

Figure 13: Roughness magnitude

Further details of the five maneuvers are included in Appendix B.

1.6 Contributions of this thesis

Tripped rollover is a very common form of rollover that has received little research attention. Since many tripped rollovers occur when a vehicle leaves the road and encounters sloped, rough, and deformable terrain, this thesis will investigate the stability limits imposed by terrain factors and develop a technique for stability measurement that is valid in tripped rollover situations.

In Chapter 2, an analysis of the effects of terrain slope, roughness, and deformability on vehicle rollover stability in road departure scenarios is presented. A simple rollover model that captures the first-order effects of each of these terrain features is presented and used to compare the relative danger posed by each factor.

In Chapter 3, an instantaneous stability metric is developed that is valid in road departure scenarios, which involve sloped, rough, and deformable terrain. An important design constraint of the metric is to not require prohibitively expensive sensors or calibration for an excessive number of vehicle parameters. The metric is compared to

those discussed in Sections 1.3 and 1.4 and is experimentally validated with wheel lift-off detection.

In Chapter 4, sensing strategies for tripped rollover are discussed. An uncertainty analysis of the stability metric presented in Chapter 3 is given and the relative importance of each sensor and parameter is assessed.

2

CHAPTER 2: TRIPPING MECHANISMS IN ROLLOVER

Road departure is a common incident in many rollovers, and terrain slope, roughness, and deformability are features of off-road surfaces that can reduce rollover stability. This chapter presents a simple rollover model and characterizes the destabilizing effects of terrain slope, roughness, and deformability.

2.1 Simple rollover model

In this section, a simple vehicle rollover model is developed to yield insight into the factors influencing vehicle rollover stability. A quasistatic planar vehicle model is analyzed to determine the first-order effects of road slope, roughness, and deformability on rollover stability.

The vehicle is modeled as a single rigid body in the plane perpendicular to the longitudinal vehicle axis, such that it can translate laterally and vertically and rotate about its roll axis as in Figure 14. The vehicle travels on an uneven terrain surface, and the position of its center of gravity (c.g.) at any point in time is specified by the angles $\theta_L \equiv \angle V_L LC$ and $\theta_R \equiv \angle V_R RC$, where points V_L and V_R are directly above points L and R.

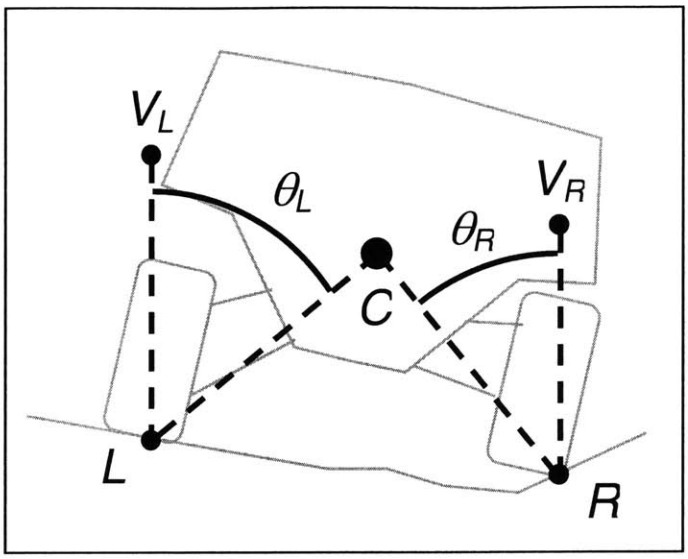

Figure 14: Planar Vehicle Model

A free body diagram of the vehicle is shown in Figure 15 with terrain contact forces $\mathbf{F}_L$ and $\mathbf{F}_R$ acting at terrain contact points L and R and the gravitational force $m\mathbf{g}$ and inertial force $-m\mathbf{a}$ acting at the system c.g. C. Gravitational and inertial force can be lumped into a single body force vector $\mathbf{F}_c = m(\mathbf{g}-\mathbf{a})$.

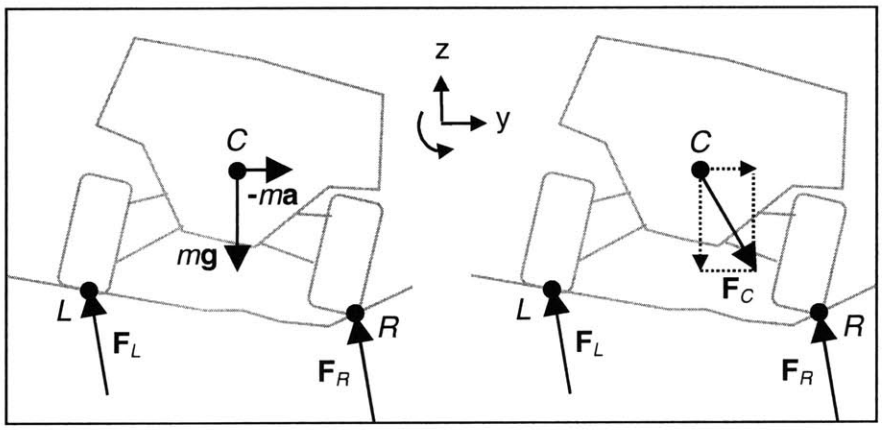

Figure 15: Free Body Diagram of Planar Vehicle Model

Newton's 2nd Law for the vehicle is shown in (2-1), (2-2), and (2-3).

$$\sum \mathbf{F} = m\mathbf{a} \tag{2-1}$$

$$\mathbf{F}_L + \mathbf{F}_R + m\mathbf{g} = m\mathbf{a} \tag{2-2}$$

$$\mathbf{F}_L + \mathbf{F}_R + \mathbf{F}_C = 0 \tag{2-3}$$

An intuitive measure of stability proposed by Papadopoulos in [37] defines stability by the direction of the body force vector $\mathbf{F}_c$ with respect to the wheel-terrain contact points. If the line of action of $\mathbf{F}_c$ points inside the wheels, as in the left side of Figure 16, it is a stabilizing force. If the line of action of $\mathbf{F}_c$ points outside the wheels, however, as in the right side of Figure 16, it is a destabilizing force that will lead to rollover.

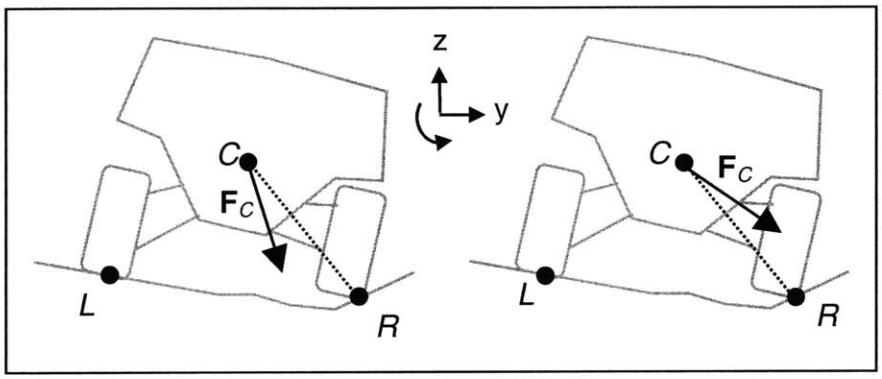

Figure 16: Illustration of Stable and Unstable Body Force

An alternative view of vehicle stability considers the angular momentum of the vehicle with respect to its c.g. The conservation of angular momentum principle, shown in (2-4), equates the moments $\mathbf{M}_C$ acting on the vehicle to the change in angular momentum $\dot{\mathbf{H}}_C$ of the vehicle with respect to point C. Moments are caused by wheel-terrain contact forces, computed with (2-5), where $\mathbf{L}_C$ and $\mathbf{R}_C$ are position vectors of points *L* and *R* relative to point *C*. The change in angular momentum, shown in (2-6), is composed of an angular acceleration term, where $\mathbf{I}_C$ is the inertia matrix of the body at point *C* and $\dot{\boldsymbol{\omega}}$ is the angular acceleration. By substituting (2-5) and (2-6) into (2-4), (2-

7) is obtained. In an example of the limiting case, the left wheel has lifted off the ground so that (2-7) becomes (2-8).

$$\mathbf{M}_C = \dot{\mathbf{H}}_C \tag{2-4}$$

$$\mathbf{M}_C = \mathbf{L}_C \times \mathbf{F}_L + \mathbf{R}_C \times \mathbf{F}_R \tag{2-5}$$

$$\dot{\mathbf{H}}_C = \mathbf{I}_C \dot{\boldsymbol{\omega}} \tag{2-6}$$

$$\mathbf{L}_C \times \mathbf{F}_L + \mathbf{R}_C \times \mathbf{F}_R = \mathbf{I}_C \dot{\boldsymbol{\omega}} \tag{2-7}$$

$$\mathbf{R}_C \times \mathbf{F}_R = \mathbf{I}_C \dot{\boldsymbol{\omega}} \tag{2-8}$$

The quantity · is very important for rollover stability, since it represents acceleration toward or away from rollover. In the limit case mentioned above, a positive · would accelerate the vehicle away from rollover to regain contact with the ground, while a negative · would accelerate the vehicle toward rollover. Clearly the sign of the angular acceleration term is important for vehicle stability, and according to (2-8), it is equal to the sign of the cross product $\mathbf{R}_C \times \mathbf{F}_R$. A geometric analysis of this cross product can yield insight into the terrain properties related to stability.

A simple model of terrain contact forces is illustrated in Figure 17. The surface normal at the contact point is specified by the angle β measured from the vertical. The component of the contact force normal to the surface is F_N and the component tangent to the surface is F_T. The angle between the force $\mathbf{F}_R$ and the surface normal is defined as ϕ and can be computed with (2-9).

$$\phi = \tan^{-1}\left(\frac{\mathbf{F}_T}{\mathbf{F}_N}\right) \tag{2-9}$$

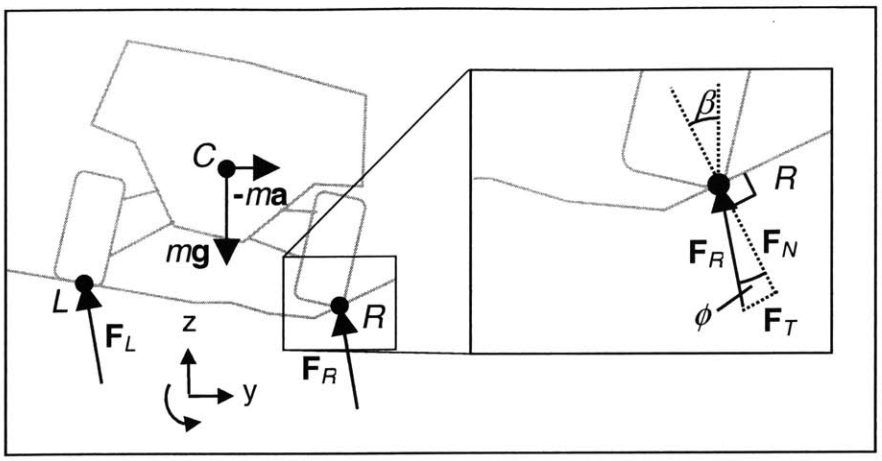

Figure 17: Terrain Force Direction

If it is assumed that the maximum tangential force is proportional to the normal contact force by the coefficient of friction μ, then the inequality (2-10) holds. Dividing (2-10) by F_N yields (2-11).

$$-\mu \mathbf{F}_N \leq \mathbf{F}_T \leq \mu \mathbf{F}_N \tag{2-10}$$

$$-\mu \leq \frac{\mathbf{F}_T}{\mathbf{F}_N} \leq \mu \tag{2-11}$$

This implies a constraint on the direction of physically attainable terrain contact forces, such that the direction of the total force must be within a fixed angle of the surface normal, as specified by (2-12) and illustrated in Figure 18. This limitation is often expressed in the literature as a friction cone [15, 29].

$$\tan^{-1}(-\mu) \leq \phi \leq \tan^{-1}(\mu) \tag{2-12}$$

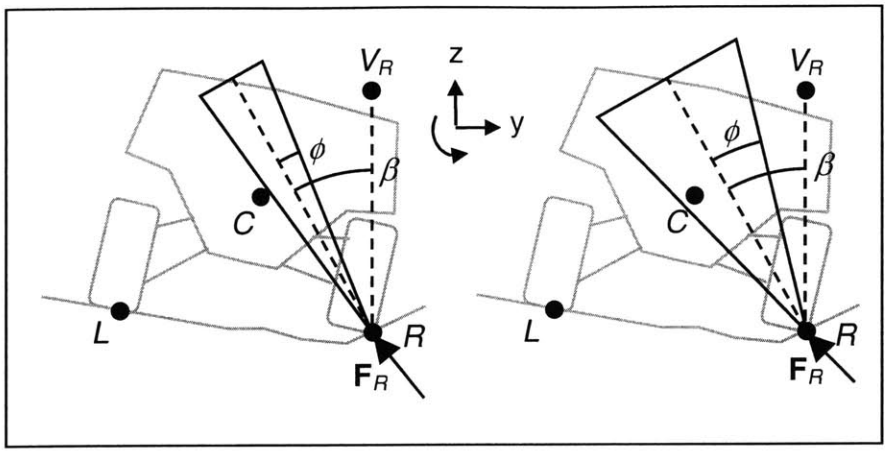

Figure 18: Physically Admissible Contact Forces

The limits on the direction of the terrain contact forces given in (2-12) and illustrated in Figure 18 impose bounds on the cross product $\mathbf{R}_C \times \mathbf{F}_R$ from (2-8). Since the cross product of parallel vectors is zero, the angular acceleration is zero when the force vector $\mathbf{F}_R$ is parallel to the moment arm vector $\mathbf{R}_C$. This represents a semistable state and is only physically possible if point C lies in the friction cone. In the left portion of Figure 18, point C is not in the friction cone, and only positive, stabilizing physical angular accelerations are physically attainable. In the right portion of Figure 18, however, point C lies within the friction cone indicating that positive, zero, and negative angular accelerations are physically possible. Recalling the definition of the c.g. position angle $\theta_R \equiv \angle V_R RC$, the physical conditions for a positive, stabilizing angular acceleration can be seen in (2-13).

$$\theta_R > \beta + \tan^{-1}\mu \tag{2-13}$$

The friction-based limit on the angular acceleration is not a strong guarantee of rollover stability, however. Note the left portion of Figure 19, in which the conditions of (2-13) are met. If a sufficiently large impulse of angular velocity ω_0 is imparted, the

vehicle will rotate so that the stability condition is no longer met, as in the right portion of Figure 19.

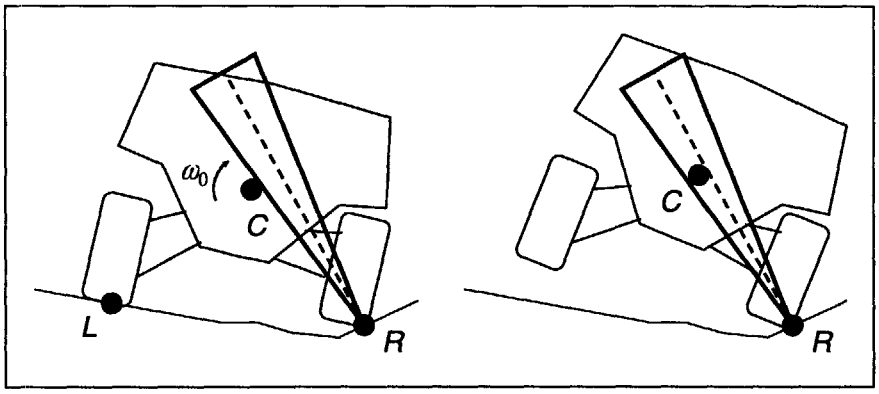

Figure 19: Rotation into Friction Cone

While this analysis does not provide a strong guarantee for the prevention of rollover, it does provide a physical basis for analyzing the effect of various terrain surface characteristics on vehicle rollover stability

2.2 Untripped rollover

As discussed in Chapter 1, untripped rollover occurs on a flat, smooth surface as a result of tire friction forces, while tripped rollover can be caused by a number of mechanisms, including impact with a curb, traversal of sloped or rough road surfaces, and tires skidding into soft soil.

To apply the stability constraint of the previous section to untripped rollover, $\beta=0$ (corresponding to flat ground) is substituted into (2-13), leading to (2-14). By considering typical values of the c.g. position of several vehicle classes (Table 5) and friction coefficient of typical road surfaces (Table 6), the likelihood of untripped rollover to occur can be assessed. The friction values are obtained from [25], and the c.g. position values from [26].

$$\theta_R > \tan^{-1} \mu \tag{2-14}$$

Vehicle Class	Static θ	Cornering θ
Passenger Car	50° – 55°	48° – 53°
SUV / Pickup	43° - 47°	41° - 45°

Table 5: Typical C.G. Position Angles on Flat Ground

Two ranges of c.g. position values are shown in Table 5 for static and cornering conditions. Suspension compliance allows the c.g. position to change during cornering maneuvers, which results in a smaller effective stability margin. A plot of c.g. position during Maneuver 1 is given in Figure 20, which illustrates this effect.

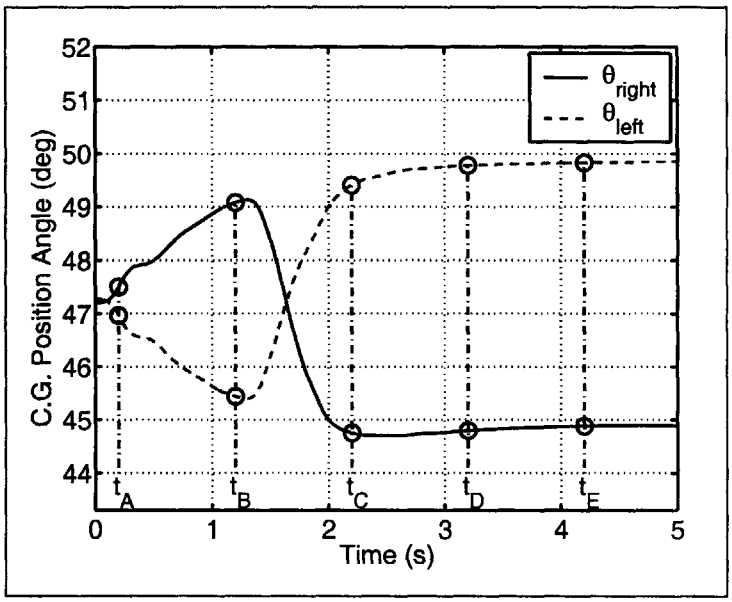

Figure 20: Maneuver 1 C.G. Position Angles

Typical friction values for several surfaces are given in Table 6. Illustrations of an example car and SUV with c.g. position angles and friction angles are given in Figure 21 and Figure 22. Only for asphalt with particularly large friction values is the typical

SUV unstable according to (2-14), while the typical car is stable for all the surfaces shown.

Surface Type	μ	$\tan^{-1}\mu$
Asphalt	0.75 – 1.10	37° – 48°
Wet Asphalt	0.25 – 0.65	14° – 33°
Gravel	0.40 – 0.55	22° – 29°
Ice	0.10 – 0.20	6° – 11°

Table 6: Typical Road Surface Friction Values

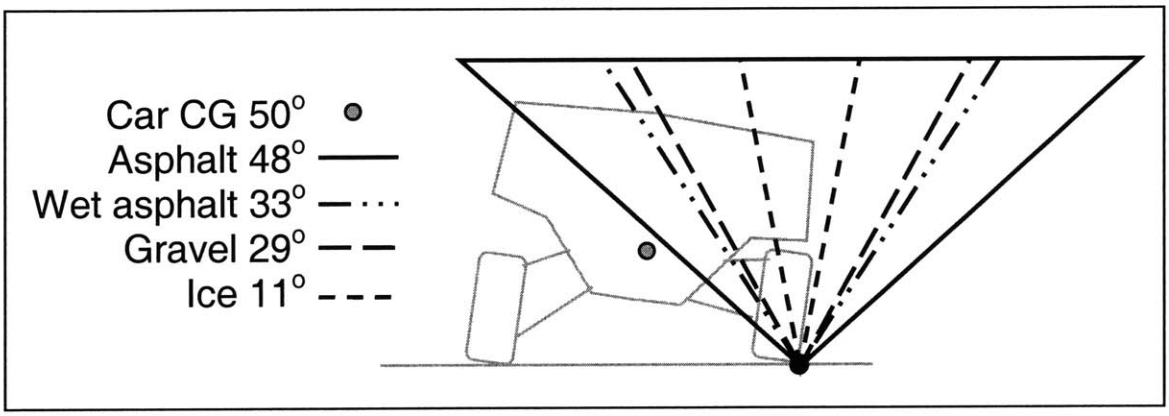

Figure 21: Car C.G. and Friction Angles

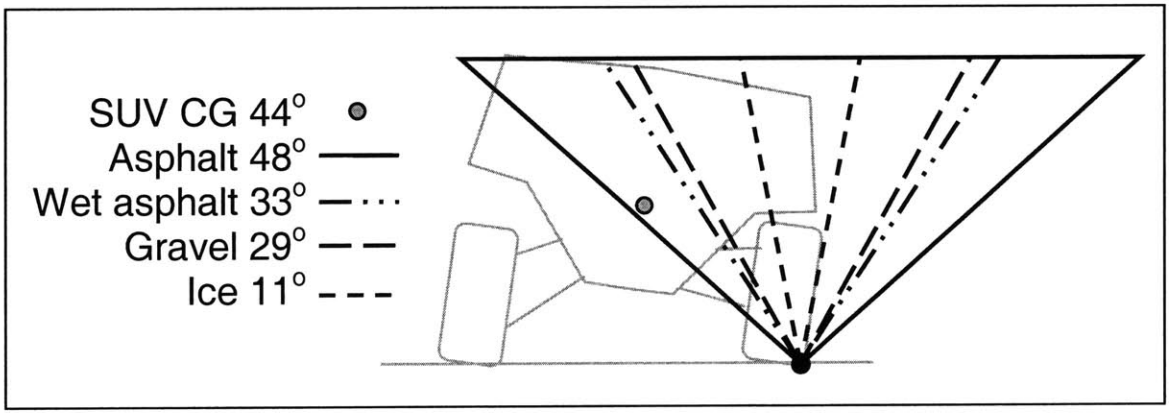

Figure 22: SUV C.G. and Friction Angles

It can be seen that the typical vehicle c.g. position angle is larger than the friction angle of most surfaces. This suggests that many vehicles are quasistatically stable in

untripped conditions. In road departure scenarios, however, off-road surfaces commonly have sloped, rough, and deformable terrain. The effect of these three factors will be analyzed with the simple model in the following sections.

2.3 Effects of deformable terrain

Deformable terrain, such as soft soil, is a characteristic of road shoulders that has been cited as a cause of rollover in numerous accident reports [48]. Terrain is considered deformable if it cannot support a vehicle without non-negligible wheel sinkage. For wheels traveling laterally on deformable terrain, resisting forces will act on the wheel sidewall via a bulldozing effect, in addition to the surface friction forces acting on the bottom of the wheel. Since terrain deformability affects both normal and tangential contact forces, its effect will be modeled as an effective friction coefficient that includes the effect of bulldozing. It is hypothesized that the magnitude of this effective friction coefficient will provide insight into its effect on vehicle rollover stability.

Several empirical measurements of the effective friction coefficient of deformable terrain have been conducted [8, 12]. The result of one of these studies is shown in Figure 23. These results suggest that soft soils could potentially cause tripped rollovers, since they can have a large effective coefficient of friction.

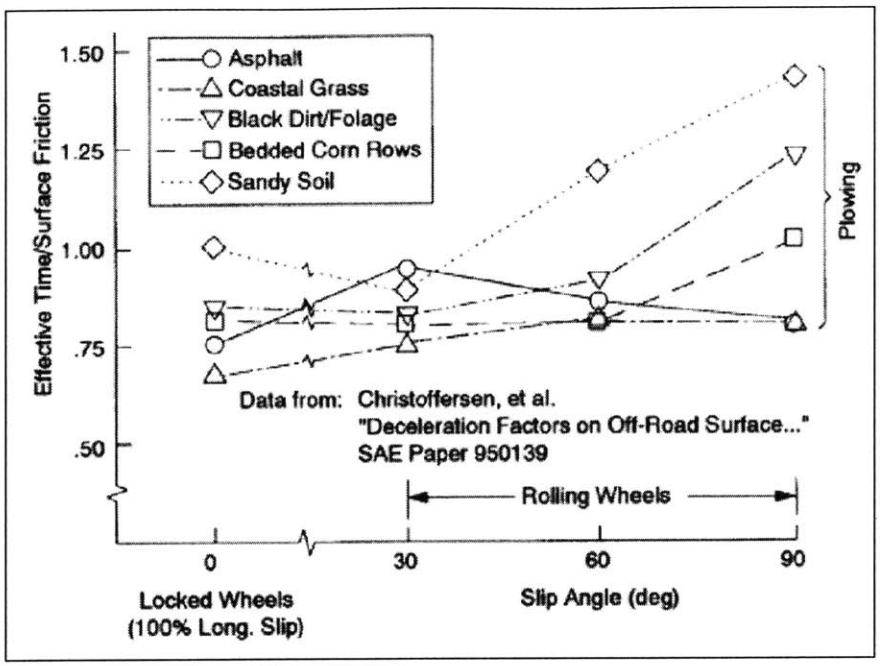

Figure 23: Experimental Soil Friction [30]

In order to gain a greater understanding of the terramechanics involved in the generation of tire/soil forces, the authors of [30] applied Bekker's semi-empirical sinkage models along with a soil strength model to estimate bulldozing forces. Their results indicated a wide variation in the capability of lateral force generation for the soils tested.

Bekker's equation relates steady-state sinkage of a wheel to the normal load on the wheel as in (2-15) and illustrated in Figure 24. The parameters n, k_c, and k_ϕ are intrinsic soil parameters and D, b, and b_{tr} are geometric properties of the wheel. By inverting (2-15), the normal force can be found as a function of sinkage z_r, as in (2-16).

$$z_r = \left[\frac{3F_z}{b_{tr} \cdot (3-n) \cdot \left(k_c / b + k_\phi \right) \cdot \sqrt{D}} \right]^{2/(2n+1)} \tag{2-15}$$

$$F_z = z_r^{(2n+1)/2}\left[\frac{(3-n)}{3} b_{tr} \cdot \left(k_c/b + k_\phi\right) \cdot \sqrt{D}\right] \tag{2-16}$$

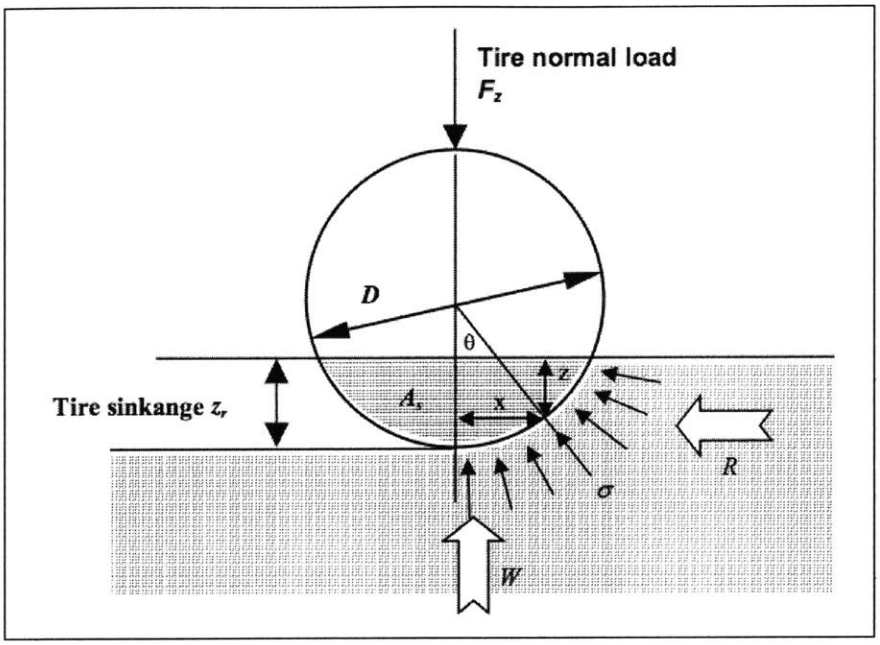

Figure 24: Wheel Sinkage [30]

Forces tangential to the surface are caused by surface friction and bulldozing resistance of the soil. The frictional force is computed with a typical friction coefficient μ, while the bulldozing force F_{yb} is a function of wheel sinkage z_r and slip angle α. The bulldozing force is illustrated in Figure 25 and is computed with (2-17) from [30]. The variables A_1 and A_2 are related to the area of the sidewall in contact with the soil, and the remaining parameters γ_s, N_ϕ, and c in (2-17) are intrinsic soil properties. The total tangential force is computed in (2-18).

$$F_{yb} = \left(\gamma_s N_\phi A_1 + 4c\sqrt{N_\phi} A_2\right) \sin^2 \alpha \tag{2-17}$$

$$F_T = \mu F_z(z_r) + F_{yb}(z_r, \alpha) \tag{2-18}$$

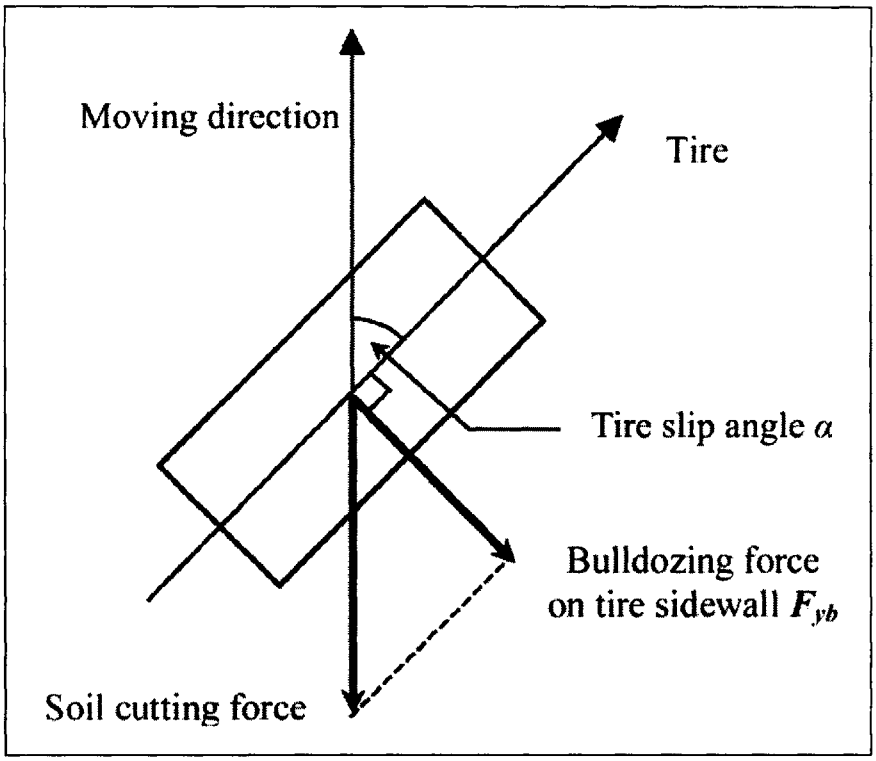

Figure 25: Tire Sideslip [30]

An effective friction coefficient is defined in (2-19) as the ratio of total tangential forces to normal forces. It is computed with (2-20) and is a function of wheel sinkage and slip angle.

$$\mu_{eff} \equiv \frac{F_T}{F_z} \tag{2-19}$$

$$\mu_{eff}(z_r, \alpha) = \mu + \frac{F_{yb}(z_r, \alpha)}{F_z(z_r)} \tag{2-20}$$

As seen in (2-20), the effect of bulldozing is to add a "surcharge" to the nominal friction coefficient of the soil. Note that the surcharge $\frac{F_{yb}(z_r, \alpha)}{F_z(z_r)}$ varies with sinkage and slip angle. Using (2-16) and (2-17) with soil parameters from [52, pg. 136], the magnitude of this bulldozing friction surcharge was estimated for several types of soils.

The friction surcharge for sinkages from 0"-6" and $\alpha = 90^o$ is shown Figure 26 for six types sand, loam, and clay. Any percents listed in Figure 26 correspond to water content of the soil. There is significant range of friction values among the soils tested, but it can be seen that the bulldozing surcharge can be substantial.

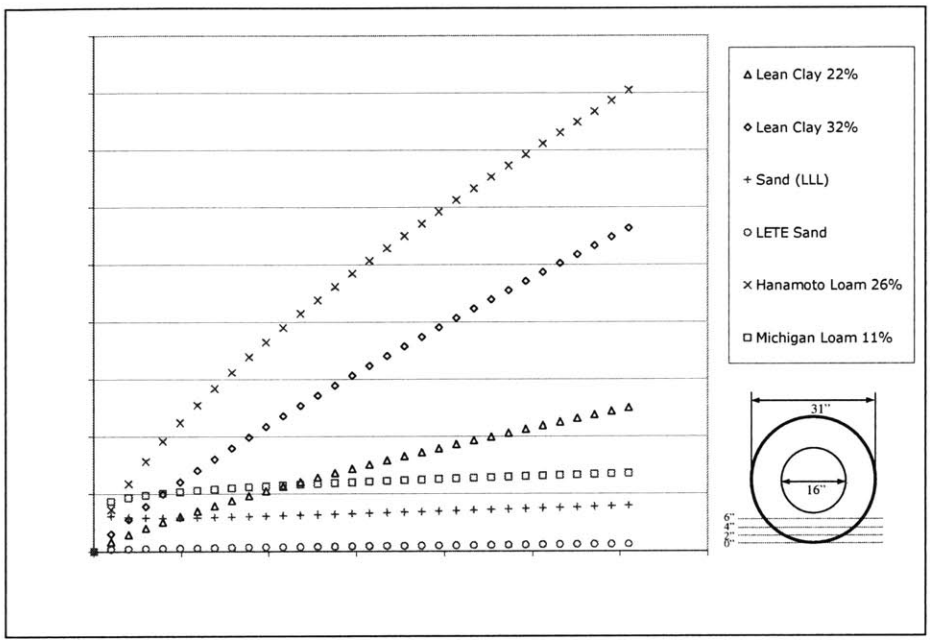

Figure 26: Bulldozing friction surcharge of 6 soils

The change in bulldozing surcharge with sinkage is shown in Figure 26, but according to (2-16), the sinkage is determined by the wheel load. This yields a single friction value for a given wheel load on a given soil. The total effective friction is plotted in Figure 27, Figure 28, and Figure 29 for wheel loads of 5 kN, 7.5 kN, and 10 kN respectively. These loads correspond to those of a passenger light utility vehicle. Note that these figures show the total effective friction, assuming a surface friction value of 0.7, and compares the total effective friction with a typical asphalt friction value of 0.9. It can be seen that most of the soils evaluated have a smaller effective friction value than asphalt.

Several surfaces were omitted from the plots below that were unable to support a 5 kN load without sinkage up to the hub of the wheel. This included two loams (LLL 22% and Hanamoto 32%) as well as three virgin snow surfaces (US Army, Harrison, Sweden). Data on compacted snow was not available, though snow banks were listed as cause of 0.4% of rural and 0.5% of urban rollovers [48]. A full set of sinkage and soil strength data for soils with organic matter (muskeg) was also not available.

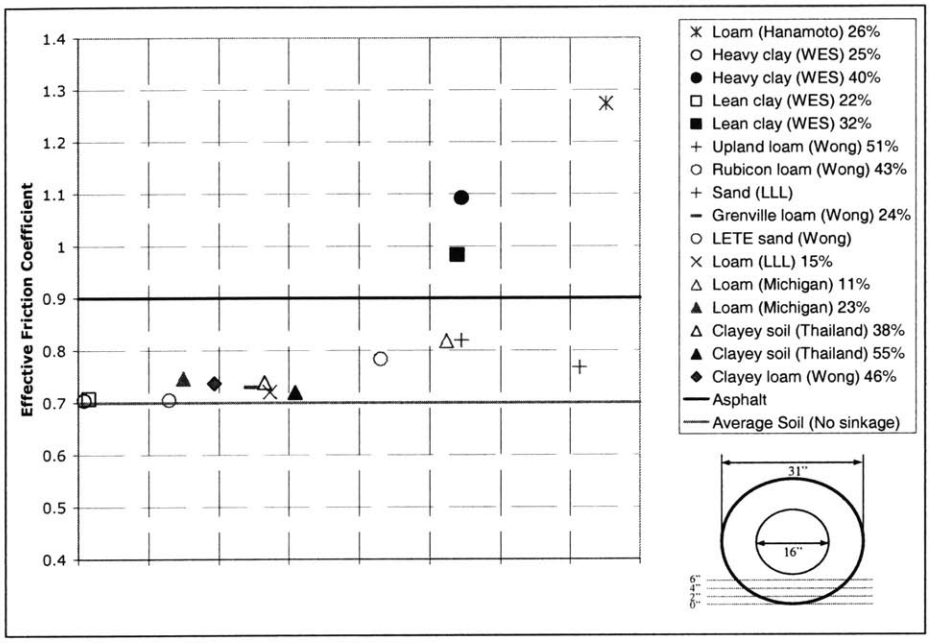

Figure 27: Effective friction for all soils at 5kN

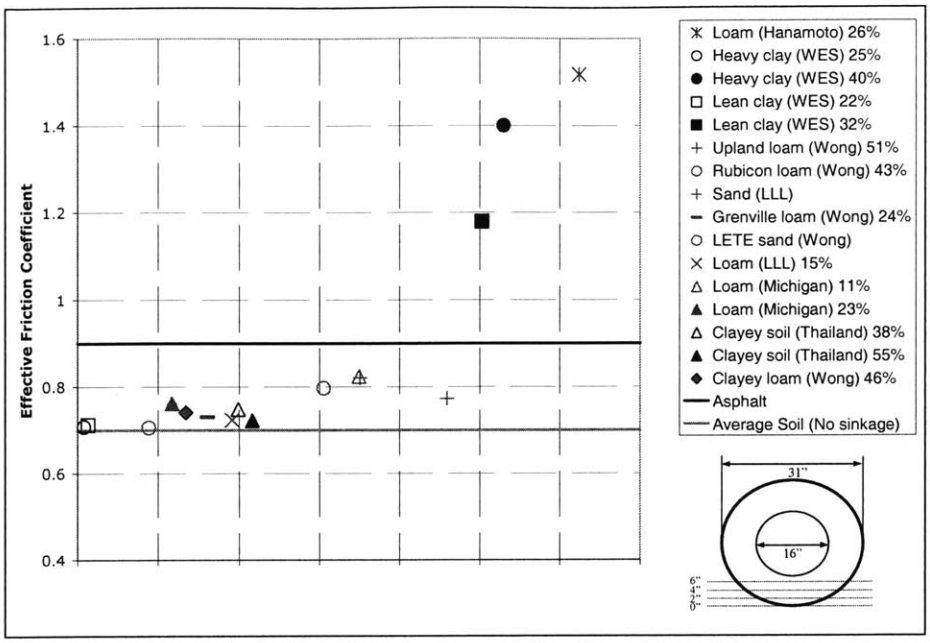

Figure 28: Effective friction for all soils at 7.5 kN

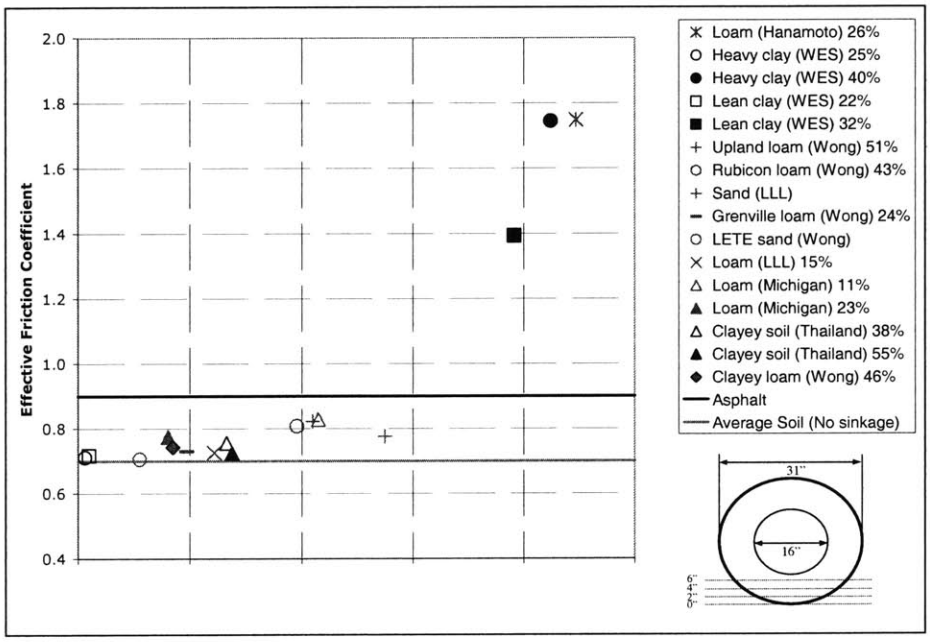

Figure 29: Effective friction for all soils at 10 kN

From this analysis, it can be concluded that most soils have an effective coefficient of friction comparable to typical road surfaces, with a few notable exceptions. The three soils that had exceptional effective friction coefficients also had very large sinkages and relatively large water contents. Since knowledge of correspondence that

these soils have to actual soils in use on the nation's roads is unclear, this does not implicate soil deformability as a "smoking gun" in rollover accidents.

An important effect that deformability can have on rollover stability that was not addressed here is in changing the handling characteristics of the vehicle traversing these surfaces. Changing the handling qualities of a vehicle can lead to loss of control, which was identified as a precursor to many rollover accidents in Chapter 1.

2.4 Effects of slope

Terrain slope is another factor in road departure accidents that is an important destabilizing factor in rollover. In this section, the effects of smooth slopes on vehicle stability are considered, as illustrated in Figure 30. The effect of terrain traversing a change in surface normal will be presented in the following section.

The angle β in the stability condition of the simple model (2-14) represents the surface inclination. Note, however, that frictional constraints governing the possibility of destabilizing angular accelerations to occur from (2-14) are independent of slope, if the surface is smooth and all vehicle wheels are in contact with the ground. This can be seen in Figure 30, where the change in the c.g. position angle on sloped ground is offset by the change in direction of the friction cone.

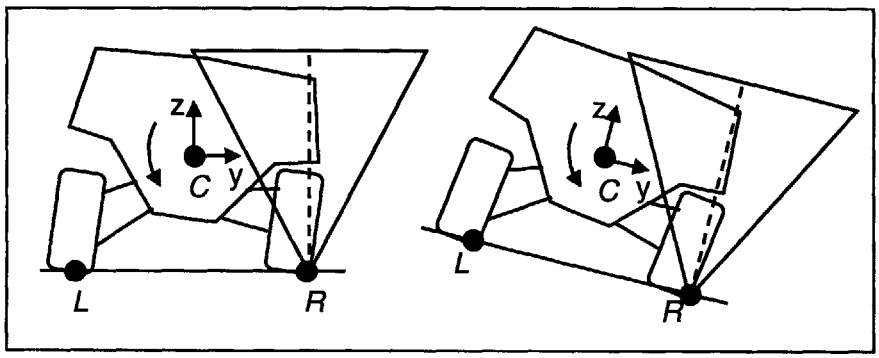

Figure 30: Friction Cone on Sloped Ground

This simple analysis illustrates that the effect of friction on rollover stability is independent of terrain inclination. For surfaces with sufficient friction to cause destabilizing angular accelerations, it has been shown that slope affects the range of safe maneuvers that can be executed on a given surface [43].

A simple maneuver to use in stability analysis is a turn of constant curvature. The lateral acceleration of a constant curvature turn increases with velocity squared, as in (2-21). The lateral acceleration acts via an inertial force at the c.g. to destabilize the vehicle at high speed. For an axisymmetric vehicle, the maximum safe lateral acceleration on flat ground is equal in both directions, as in the left side of Figure 31. On a slope, however, a component of gravity acts laterally as well, such that the range of safe curvatures is biased towards turning downhill, as in the right side of Figure 31. Some maneuvers that are safe on flat ground can lead to rollover on a slope, and conversely, some maneuvers can be performed on a slope that would be unsafe on flat ground, such as a high-speed banked turn.

$$\frac{a_T}{g} = \frac{V^2}{gR} \tag{2-21}$$

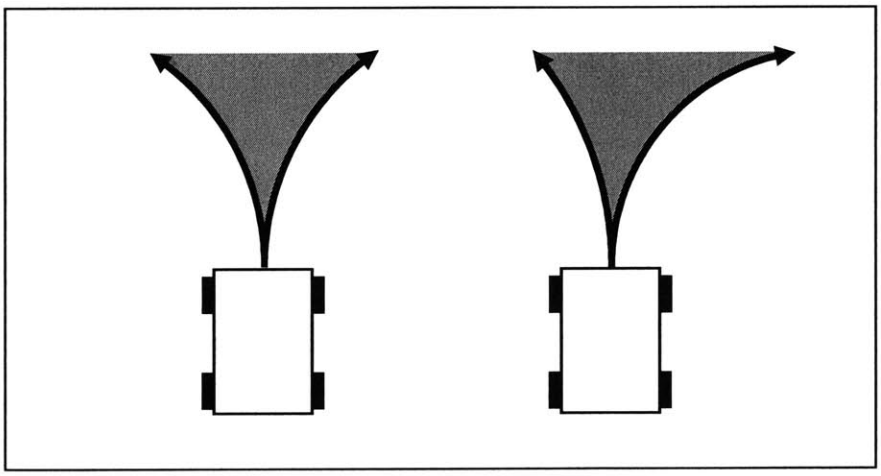

Figure 31: Safe Curvatures on Flat and Sloped Surface

Quasistatic limits of safety on sloped surfaces can be found by considering the angular momentum equation (2-8) when the angular acceleration is zero. When combined with Newton's second law (2-3), (2-22) and (2-23) are found. These quasistatic limits of stability occur when the body force vector $\mathbf{F}_c$ points directly at a contact point L or R.

$$\mathbf{L}_C \times \mathbf{F}_C = 0 \tag{2-22}$$

$$\mathbf{R}_C \times \mathbf{F}_C = 0 \tag{2-23}$$

Recalling that this body force vector $\mathbf{F}_c$ is composed of gravity and acceleration components, $m(\mathbf{g}-\mathbf{a})$, acceleration bounds can be derived from (2-22) and (2-23). The definitions of each vector in the frame shown in Figure 30 are given below. By substituting the vector definitions into (2-22) and (2-23), the acceleration limits in (2-24) and (2-25) can be derived. A plot of these limits is shown in Figure 32. Here increasing the ground slope increases the range of safe maneuvers in the downhill direction, while decreasing the range in the uphill direction.

$$m(\mathbf{g}-\mathbf{a}) = \begin{bmatrix} 0 \\ g\sin\beta - a_y \\ g\cos\beta_z \end{bmatrix} \qquad \mathbf{L}_C = \begin{bmatrix} 0 \\ -T \\ -h \end{bmatrix} \qquad \mathbf{R}_C = \begin{bmatrix} 0 \\ T \\ -h \end{bmatrix}$$

$$\frac{a_{yL}}{g} = \frac{T}{h}\cos\beta + \sin\beta \tag{2-24}$$

$$\frac{a_{yR}}{g} = \frac{T}{h}\cos\beta - \sin\beta \tag{2-25}$$

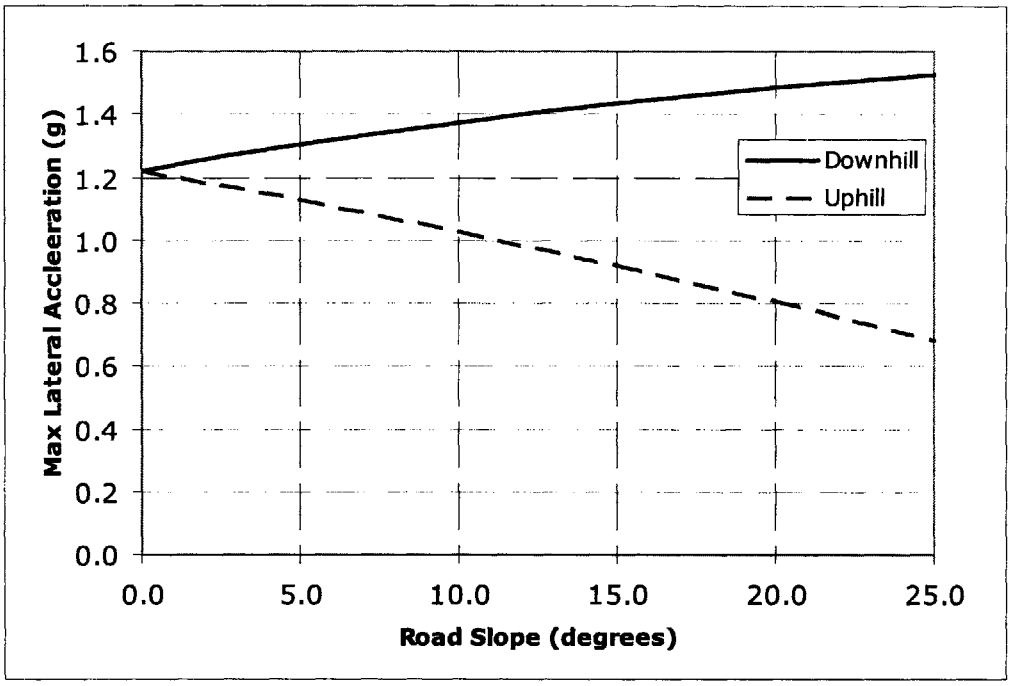

Figure 32: Maneuver Limits on Sloped Terrain

Sloped terrain is likely to be encountered on the shoulder of a road after a road departure. The inclination of U.S. road shoulders is recommended to be no steeper than 18° (3:1 slope) by AASHTO specification [1], which according to Figure 32 is enough to cause a 25% decrease in the safe lateral acceleration of road recovery maneuvers.

For the simple model presented in Section 2.1, the friction coefficient is the governing factor in stability, independent of surface inclination. Given sufficient friction, however, terrain inclination does impact rollover stability by changing the limits of safe maneuvers.

2.5 Effects of surface roughness

Surface roughness is another characteristic of road departure scenarios that can influence tripped rollover stability. Here, the roughness of a terrain patch is defined by the extent to which the elevation which deviates from a planar surface. This section

addresses three of the ways that rough terrain influences rollover stability: by causing variation in wheel-terrain contact forces, by causing variation in vehicle c.g. position, and by enabling destabilizing angular accelerations via changes in surface inclination.

The first effect of roughness is to cause variation in wheel-terrain contact forces, which has the potential to alter a vehicle's handling dynamics [3] and reduce the effective coefficient of friction of the surface [4]. This may lead to loss of control, which was cited by Viner as a common factor in many rollover accidents [49]. Maneuvers 3-5 all involved road departure with varying levels of roughness on the shoulder. The magnitude of the roughness is illustrated in Figure 33, and the effect on normal forces for each maneuver is shown in Figure 34 and Figure 35.

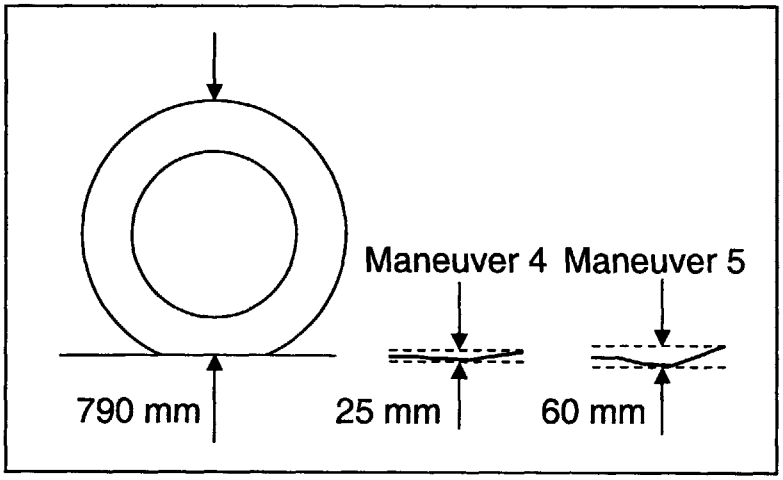

Figure 33: Roughness Magnitude

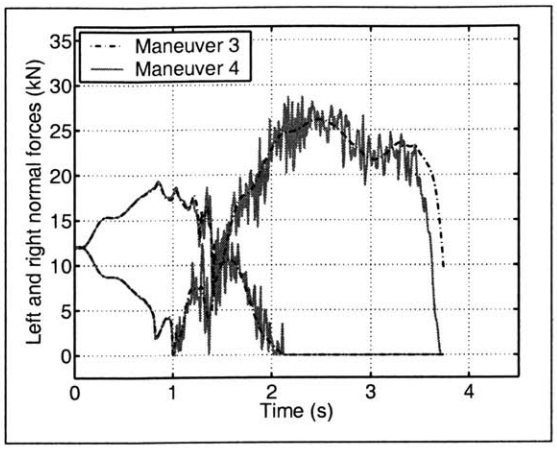

Figure 34: Normal Force Variation in Maneuvers 3 and 4

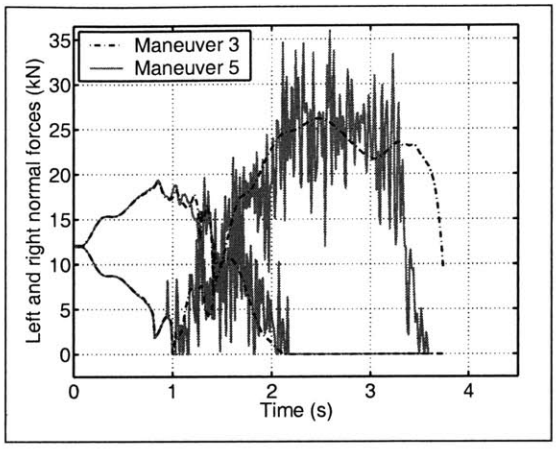

Figure 35: Normal Force Variation in Maneuvers 3 and 5

The second effect of roughness is to cause variation in c.g. position through excitation of suspension dynamics. To illustrate this, the c.g. position angles θ_L and θ_R defined in Figure 14 were computed from the canonical maneuver simulations. The position angles for Maneuver 3 are shown in Figure 36 and the differences in c.g. position angle during Maneuvers 4 and 5 from that of Maneuver 3 are shown in Figure 37.

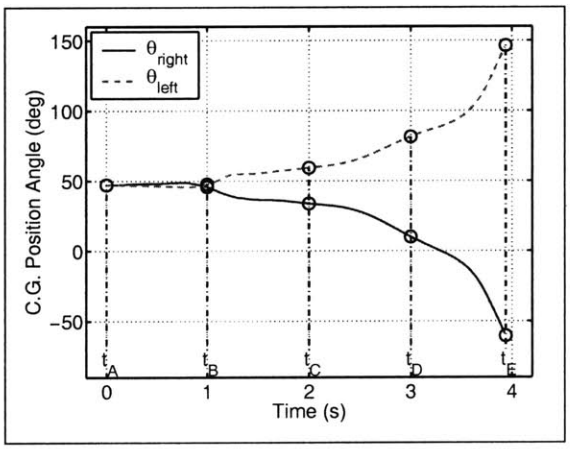

Figure 36: Maneuver 3 C.G. Position

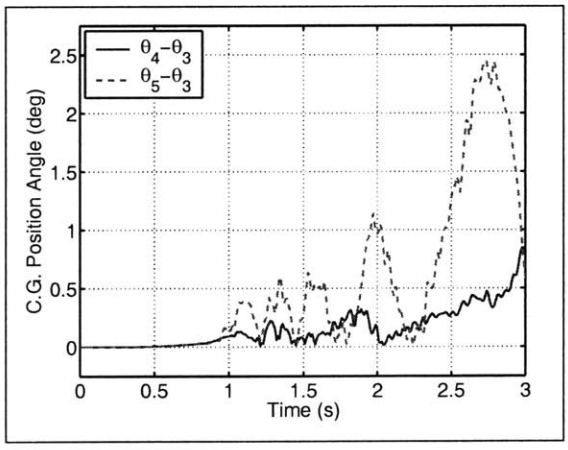

Figure 37: C.G. Position Angle Difference on Rough Terrain

In addition to reducing vehicle stability with variation in c.g. position, rough terrain can enable destabilizing angular accelerations with sudden changes in the direction of the surface normal. This effect is illustrated in Figure 38, in which a vehicle

is sliding sideways on rough terrain. In the left portion of Figure 38, the surface normal at contact point *R* points nearly vertically, and the c.g. is outside of the friction cone. In the right portion of the figure, the vehicle has moved to a terrain patch that has the same coefficient of friction but different inclination. This sudden change in surface normal causes the friction cone to be pointed toward the c.g. In this case, the change the change in inclination caused the c.g. to lie inside the friction cone, which is the condition previously mentioned for allowing destabilizing angular accelerations.

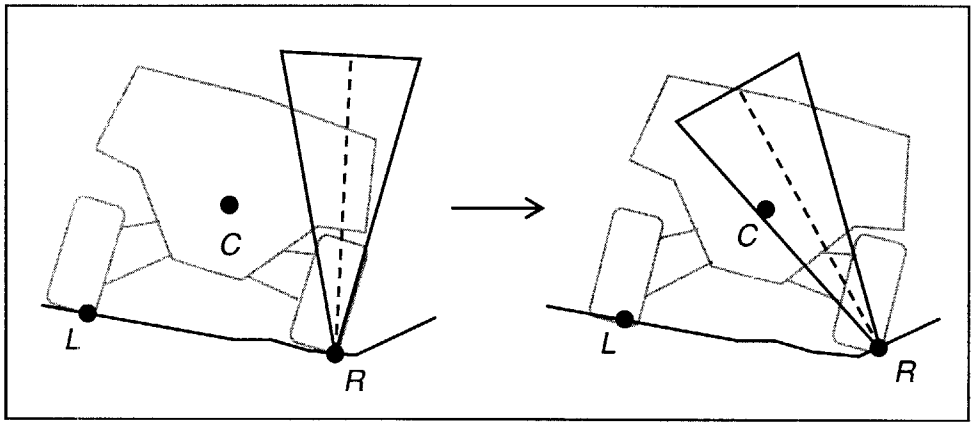

Figure 38: Change in Slope

Roughness impacts stability by causing variation in normal forces, c.g. position, and surface inclination. Each of these factors may contribute to tripped rollover instability.

2.6 Conclusion

In this chapter, a simple model was presented that captures the effect of terrain conditions on vehicle rollover stability. This model was used to examine the effects of terrain slope, roughness, and deformability, which may be important in off-road rollovers.

3

CHAPTER 3: STABILITY MEASUREMENT

This chapter presents a new approach for measuring the instantaneous rollover stability of a vehicle. The measure is based on the distribution of wheel-terrain contact forces on the vehicle, which indicates the nearness to wheel lift-off on any terrain surface, including sloped, rough, and deformable terrain. This generality ensures that the measure will be applicable in measuring stability in road departure and other tripped rollover situations. Additionally, this stability metric can be measured in real-time with automotive sensors deemed to be practical in Chapter 1.

In Section 3.1, the physical basis of the stability measure is presented intuitively. In Section 3.2, a vehicle model is presented along with a derivation of the metric using the angular momentum principle. In Section 3.3, results from simulations are provided to validate the model and compare its performance to existing stability measurement techniques. In Section 3.4, the measure is experimentally validated by detecting wheel lift-off in high-speed vehicle tests.

3.1 Physical basis of stability metric

During severe maneuvers, accurate monitoring of a vehicle's stability is important so that active control methods can be initiated to avoid loss of control and/or rollover. As mentioned in Chapter 1, extensive research has been conducted on measuring the stability of passenger vehicles traveling on flat, smooth, road surfaces. Vehicle crash statistics

show, however, that many accidents occur after a vehicle has departed the road surface. In these situations, a vehicle may encounter sloped, rough, and deformable terrain, which can degrade vehicle stability. As such, a technique for stability measurement that is accurate on sloped, rough, and deformable surfaces would be valuable for active safety systems.

There are three different phases of a typical rollover accident: normal driving on four wheels, a transition phase to two wheels, and body impact with the ground, as shown in Figure 39. As the accident progresses, vehicle controllability is reduced. For this reason, stability control systems are most effective when activated during the first phase, while all wheels are in contact with the ground. The stability measurement technique proposed here is used during the first phase to measure nearness to wheel lift-off, or nearness to the transition to two-wheel driving.

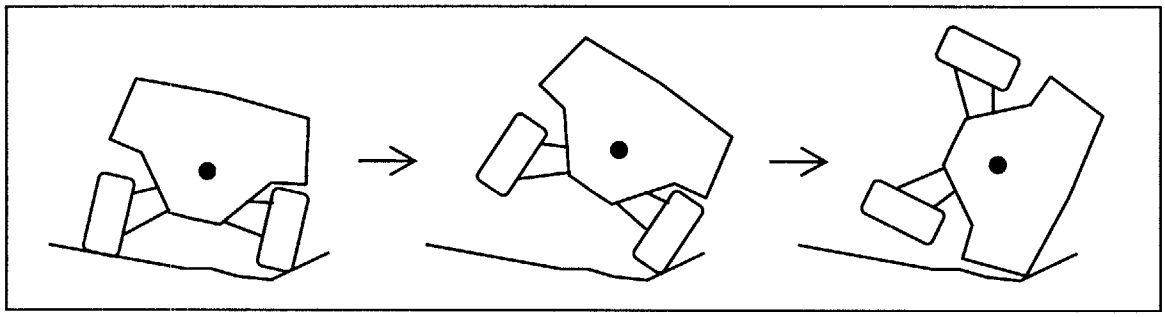

Figure 39: Typical Phases of a Rollover Accident

The distribution of terrain contact forces on the vehicle's wheels can be analyzed to determine nearness to wheel lift-off. On flat ground, an axisymmetric vehicle at rest will have contact forces distributed equally between the left and right sides. As the vehicle executes a high-speed maneuver or traverses uneven terrain, the contact force distribution will change dynamically. The transition to two wheels occurs when the contact forces for both wheels on one side of the vehicle go to zero.

As discussed in Chapter 1, a number of stability metrics based on analysis of wheel-terrain contact forces have been proposed and used in rollover stability control systems [6, 7, 36], though these approaches are only valid on flat ground. Accurate measurement of wheel-terrain contact forces on sloped and rough terrain currently requires wheel force transducers or an accurately calibrated suspension model and associated sensors, which may be impractical for production vehicles.

An alternative approach to wheel-terrain contact force measurement is to use momentum principles to define an analytical expression for contact forces that is composed of measurable sensor quantities and vehicle parameters. A simple example of this method is shown below for the planar vehicle model from Chapter 2, shown again in Figure 40. In this model, two contact forces $\mathbf{F}_L$ and $\mathbf{F}_R$ act at points L and R respectively. By applying the angular momentum principle with respect to point L or R, the moment caused by the force acting at that point is eliminated. This allows the moment caused by the other contact force to be computed.

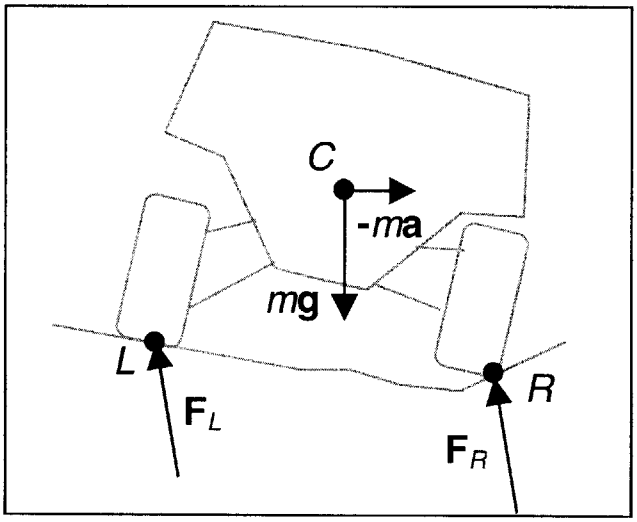

Figure 40: Simple Planar Vehicle Model

For example, if the angular momentum principle is applied with respect to point R, an expression can be derived for the contact force $\mathbf{F}_L$. The moments acting about point R, shown in (3-1), are caused by the gravitational force $m\mathbf{g}$ at point C and $\mathbf{F}_L$ at point L, where $\mathbf{C}_R$ and $\mathbf{L}_R$ are the displacement vectors to points C and L from point R. Note that the "inertial force" $-m\mathbf{a}$ or $-m\ddot{\mathbf{C}}$ is not included in (3-1), though it will appear in the angular momentum equation.

$$\mathbf{M}_R = \mathbf{C}_R \times m\mathbf{g} + \mathbf{L}_R \times \mathbf{F}_L \tag{3-1}$$

The angular momentum of the system with respect to R is shown in (3-2), where $\mathbf{I}_C$ is the inertia matrix of the body about its c.g. and $\boldsymbol{\omega}$ is the angular velocity of the body. The change in angular momentum, computed as the derivative of (3-2) is given in (3-3). Conservation of angular momentum is then expressed in (3-4).

$$\mathbf{H}_R = \mathbf{I}_C\boldsymbol{\omega} + \mathbf{C}_R \times m\dot{\mathbf{C}}_R \tag{3-2}$$

$$\dot{\mathbf{H}}_R = \mathbf{I}_C\dot{\boldsymbol{\omega}} + \mathbf{C}_R \times m\ddot{\mathbf{C}}_R \tag{3-3}$$

$$\mathbf{M}_R = \dot{\mathbf{H}}_R \tag{3-4}$$

It should be noted that (3-4) only holds for certain choices of reference point, including a fixed point in an inertial frame or the c.g. of a body [21]. These constraints are not met by any contact points of a vehicle, which are often accelerated with respect to a fixed frame and are not located at the body c.g.

These limitations of the angular momentum principle can be averted by altering the definition of angular momentum from (3-2). In (3-5), the modified angular momentum $\mathbf{H}'_R$ is formed by expressing the body velocity term $\dot{\mathbf{C}}_R$ with respect to a

fixed frame (rather than point R), as $\dot{\mathbf{C}}_0$. The modified change in angular momentum is given in (3-6), computed as the derivative of (3-5). A "pseudo-conservation" of angular momentum is given in (3-7), which will be shown to be valid with no constraints on the reference point in Section 3.2.

$$\mathbf{H}'_R = \mathbf{I}_C\boldsymbol{\omega} + \mathbf{C}_R \times m\dot{\mathbf{C}}_0 \tag{3-5}$$

$$\dot{\mathbf{H}}'_R = \mathbf{I}_C\dot{\boldsymbol{\omega}} + \mathbf{C}_R \times m\ddot{\mathbf{C}}_0 \tag{3-6}$$

$$\mathbf{M}_R = \dot{\mathbf{H}}'_R \tag{3-7}$$

By substituting (3-1) and (3-6) into (3-7) and rearranging, the moment caused by $\mathbf{F}_L$ about the right contact point can be found, as shown in (3-8).

$$\mathbf{L}_R \times \mathbf{F}_L = \mathbf{I}_C\dot{\boldsymbol{\omega}} + \mathbf{C}_R \times m\left(\ddot{\mathbf{C}}_0 - \mathbf{g}\right) \tag{3-8}$$

The moment caused by $\mathbf{F}_L$ can be estimated then given knowledge of the vehicle inertial parameters m and $\mathbf{I}_C$, the dynamic states $\dot{\boldsymbol{\omega}}$ and $\ddot{\mathbf{C}}_0 - \mathbf{g}$, and the displacement vector $\mathbf{C}_R$ from (3-8). These quantities must be practical to measure for this estimation method to be useful. The vector $\mathbf{C}_R$ can be found with an estimate of c.g. position, measurement of suspension displacement, and an estimate of the contact point location on the wheel. Noting that $\ddot{\mathbf{C}}_0 - \mathbf{g}$ is the output of an accelerometer, the sensed quantities required for (3-8) are accelerometer output, angular acceleration, and suspension displacement. Sensors for each of these quantities were deemed practical in Section 1.5. Additionally, estimators of c.g. position were presented in [19, 42] and estimates of inertial properties m and $\mathbf{I}_C$ could be obtained with similar techniques. The only

unmeasurable quantity is contact point location on the wheel, which is bounded by the size of the wheel. An uncertainty analysis of this method is provided in Chapter 4.

It should be noted that moments are not sensitive to forces acting parallel to the moment arm. For example, in Figure 41 the moment $\mathbf{M}_R$ caused by force $\mathbf{F}_L$ at L would include the effect of the component F_M but not the component F_P. When the wheels are in contact with a planar surface, the moment measures forces acting normal to the plane, while forces acting in the plane are not measured.

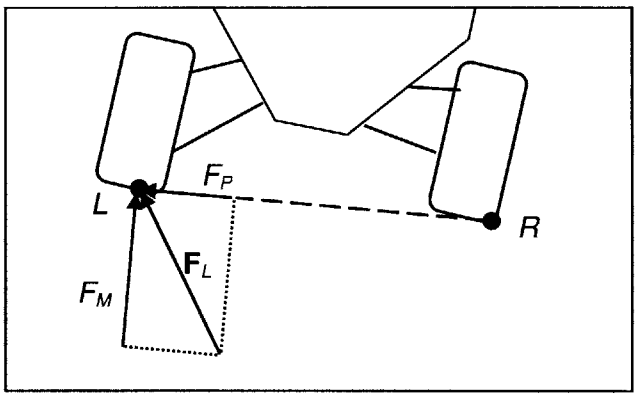

Figure 41: Measurable and Unmeasurable Force Components

3.2 Vehicle model and stability measure derivation

In this section, a vehicle model valid on sloped, rough, and deformable terrain is presented that considers the effect of wheel mass and gyroscopic forces as well as suspension displacements. Additionally, an instantaneous stability metric is derived for the model based on contact moments.

A generic l-wheeled vehicle is modeled as a multi-body system of $l+1$ rigid bodies, representing the wheels and chassis. The bodies are all able to translate and rotate relative to one another via the suspension and wheel axles. The vehicle moves with respect to a reference frame fixed at Point O, and the position of the c.g. of each

body is point c_i, which in frame O is given by $\mathbf{c}_o^i \; i \in \{1,...,l+1\}$. Additionally, $l+1$ frames are fixed to the c.g. of each body. The orientation of each body-fixed frame is given by rotation matrices $\mathbf{R}_i^o \; i \in \{1,...,l+1\}$. For each body i, $i \in \{1,...,l+1\}$, the mass is m_i, and the inertia matrix defined with respect to each body-fixed frame is $\mathbf{I}_i$, $i \in \{1,...,l+1\}$. An illustration of this model when l=4 is given in Figure 42.

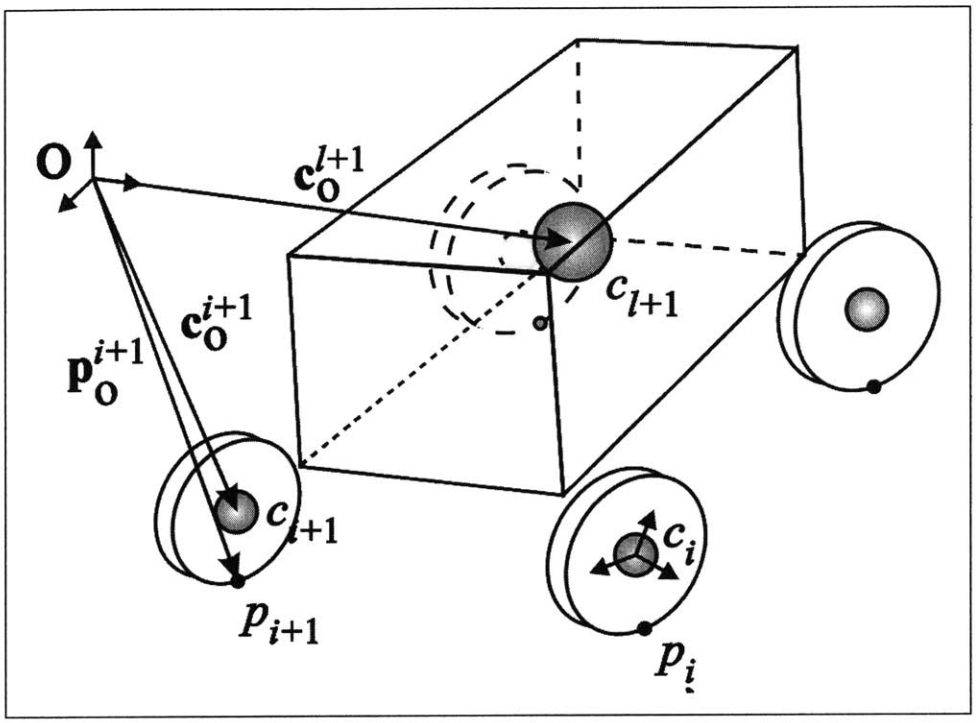

Figure 42: Vehicle model when l=4

The convention used for rotation matrices in this thesis is taken from [44], in which the matrix $\mathbf{R}_{to}^{from}$ transforms a vector from the frame *from* to the frame *to*. An example of one such vector transformation is shown in (3-9). Examples for computing the derivatives of these transformed quantities can be seen in (3-10) and (3-11), where $\boldsymbol{\omega}_o^i$ represents the angular velocity of the i^{th} frame with respect to frame O and is expressed in the coordinates of frame O. To simplify notation, the angular velocity of a frame with respect to frame O but expressed in its own coordinates will be given as

simply $\boldsymbol{\omega}_i$, defined as $\boldsymbol{\omega}_i \equiv \mathbf{R}_i^o \boldsymbol{\omega}_o^i$. Note that $\boldsymbol{\omega}_i$ is the quantity measured by a body-fixed angular velocity sensor.

$$\mathbf{x}_o = \mathbf{R}_o^i \mathbf{x}_i \tag{3-9}$$

$$\frac{d}{dt}\left(\mathbf{R}_o^i \mathbf{x}_i\right) = \dot{\mathbf{R}}_o^i \mathbf{x}_i + \mathbf{R}_o^i \dot{\mathbf{x}}_i \tag{3-10}$$

$$\dot{\mathbf{R}}_o^i \mathbf{x}_i = \boldsymbol{\omega}_o^i \times \mathbf{R}_o^i \mathbf{x}_i \tag{3-11}$$

Each of the vehicle's l wheels may be in contact with an arbitrary terrain surface (ie. flat, sloped, rough, etc.). It is assumed that the wheels make contact with the terrain at a single point. The wheel-terrain contact points p_i $i \in \{1,...,l\}$ are given by $\mathbf{p}_o^i$ in frame O and are numbered in ascending order in a clockwise manner when viewed from above, as shown in Figure 43. If any wheel i is not in contact with the terrain, p_i should be placed at a point on the wheel where contact typically occurs. Tipover axes, denoted $\mathbf{r}_o^i$, are defined as the unit vectors pointing from one contact point to the next and can be computed for $i \in \{1,...,l-1\}$ with (3-12) and for $i=l$ with (3-13).

$$\mathbf{r}_o^i = \frac{\mathbf{p}_o^{i+1} - \mathbf{p}_o^i}{\left\|\mathbf{p}_o^{i+1} - \mathbf{p}_o^i\right\|} \tag{3-12}$$

$$\mathbf{r}_o^l = \frac{\mathbf{p}_o^1 - \mathbf{p}_o^l}{\left\|\mathbf{p}_o^1 - \mathbf{p}_o^l\right\|} \tag{3-13}$$

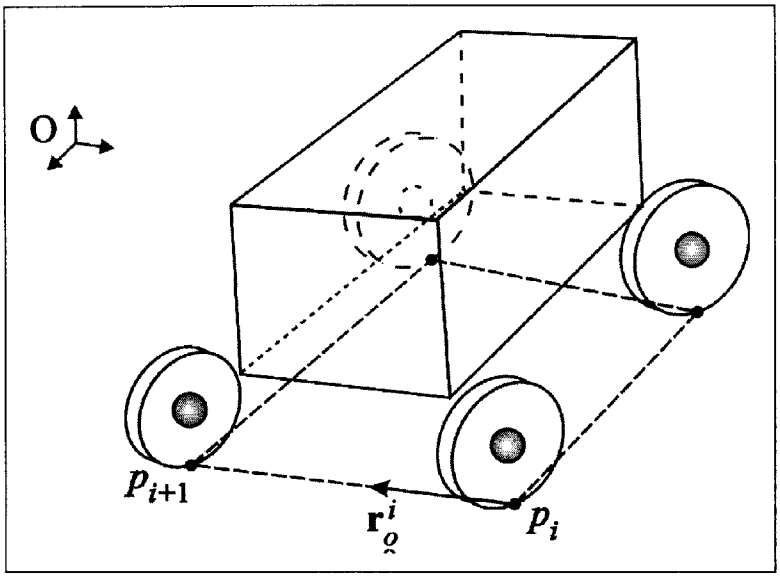

Figure 43: Tipover Axes

Previous vehicle models [36, 40, 42] have considered each body in the vehicle system separately, which requires modeling of the interaction forces between the bodies in the system. To avoid this, a single multi-body system is defined for the whole vehicle, which makes suspension forces internal to the system. Thus this model is valid for all types of suspensions and steering mechanisms. Knowledge of suspension kinematics is necessary to determine the instantaneous location of the wheel c.g. and contact points, but no knowledge of stiffness, damping, or other dynamic suspension elements is required. The lumped mass, c.g. position, and c.g. acceleration of the multi-body system can be computed with (3-14), (3-15), and (3-16) respectively.

$$m = \sum_{i=1}^{l+1} m_i \tag{3-14}$$

$$\mathbf{c}_o = \sum_{i=1}^{l+1} \frac{m_i}{m} \mathbf{c}^i_o \tag{3-15}$$

$$\ddot{\mathbf{c}}_o = \sum_{i=1}^{l+1} \frac{m_i}{m} \ddot{\mathbf{c}}_o^i \tag{3-16}$$

A free body diagram of the vehicle system is shown in Figure 44, with wheel-terrain contact forces $\mathbf{F}_o^i$ acting at p_i $i \in \{1,...,l\}$ and body forces $\mathbf{B}_o^j$ acting at q_j $j \in \{1,...,k\}$. The locations of points p_i and q_j in the fixed frame O are given by $\mathbf{p}_o^i$ and $\mathbf{q}_o^j$. Examples of body forces include gravity, aerodynamic drag, reactions from external manipulators or trailers, and collisions with other bodies.

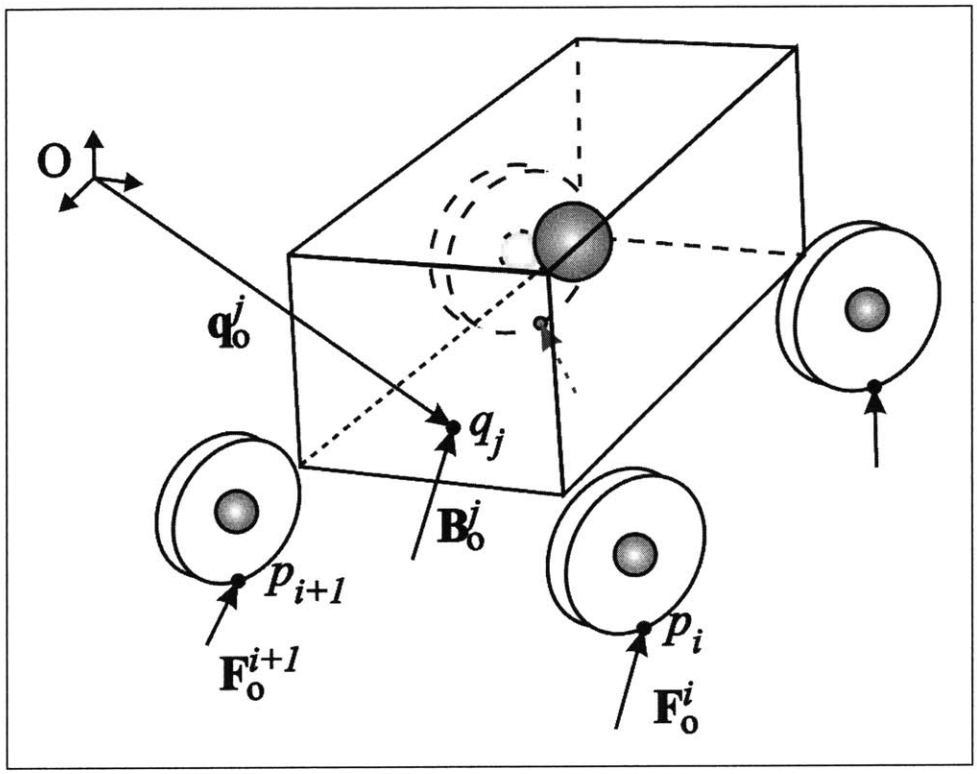

Figure 44: Free body diagram

Summing the forces acting on this system results in (3-17) and (3-18).

$$\sum \mathbf{F} = m\mathbf{a} \tag{3-17}$$

$$\sum_{j=1}^{k} \mathbf{B}_o^j + \sum_{i=1}^{l} \mathbf{F}_o^i = \sum_{i=1}^{l+1} m_i \ddot{\mathbf{c}}_o^i \tag{3-18}$$

As discussed in Section 3.1, it is desirable to apply the conservation of angular momentum principle with respect to an arbitrary reference point. To derive this relation, the principle will first be applied with respect to the fixed point O. The moments acting with respect to point O are given in (3-19). The angular momentum and its derivative are given in (3-20) and (3-21) respectively. For a fixed reference point, conservation of angular momentum holds [21]. This is expressed in (3-22).

$$\mathbf{M}_o = \sum_{j=1}^{k} \left(\mathbf{q}_o^j \times \mathbf{B}_o^j \right) + \sum_{i=1}^{l} \left(\mathbf{p}_o^i \times \mathbf{F}_o^i \right) \tag{3-19}$$

$$\mathbf{H}_o = \sum_{i=1}^{l+1} \mathbf{R}_o^i \mathbf{I}_i \boldsymbol{\omega}_i + \sum_{i=1}^{l+1} \mathbf{c}_o^i \times m_i \dot{\mathbf{c}}_o^i \tag{3-20}$$

$$\dot{\mathbf{H}}_o = \sum_{i=1}^{l+1} \left(\boldsymbol{\omega}_o^i \times \left(\mathbf{R}_o^i \mathbf{I}_i \boldsymbol{\omega}_i \right) + \mathbf{R}_o^i \mathbf{I}_i \dot{\boldsymbol{\omega}}_i \right) + \sum_{i=1}^{l+1} \mathbf{c}_o^i \times m_i \ddot{\mathbf{c}}_o^i \tag{3-21}$$

$$\mathbf{M}_o = \dot{\mathbf{H}}_o \tag{3-22}$$

The sum of moments in (3-19) and the change in angular momentum in (3-21) could be substituted into (3-22) as is, but instead (3-19) will be manipulated to introduce the arbitrary reference point *b*. The position of *b* with respect to the fixed frame is given by vector $\mathbf{b}_o$. Terms representing the sum of moments with respect to point O if all forces acted at the reference point *b* are added and subtracted from (3-19) to result in (3-23).

$$\mathbf{M}_o = \sum_{j=1}^{k}\left(\mathbf{q}_o^j \times \mathbf{B}_o^j\right) + \sum_{i=1}^{l}\left(\mathbf{p}_o^i \times \mathbf{F}_o^j\right) + \left[\sum_{j=1}^{k}\mathbf{b}_o \times \mathbf{B}_o^j + \sum_{i=1}^{l}\mathbf{b}_o \times \mathbf{F}_o^i\right] - \left[\sum_{j=1}^{k}\mathbf{b}_o \times \mathbf{B}_o^j + \sum_{i=1}^{l}\mathbf{b}_o \times \mathbf{F}_o^i\right] \tag{3-23}$$

In (3-24), components of the term $-\left[\sum_{j=1}^{k}\mathbf{b}_o \times \mathbf{B}_o^j + \sum_{i=1}^{l}\mathbf{b}_o \times \mathbf{F}_o^i\right]$ are collected into the expression $\sum_{j=1}^{k}\left(\mathbf{q}_o^j \times \mathbf{B}_o^j\right) + \sum_{i=1}^{l}\left(\mathbf{p}_o^i \times \mathbf{F}_o^j\right)$, which results in $\sum_{j=1}^{k}\left(\left(\mathbf{q}_o^j - \mathbf{b}_o\right) \times \mathbf{B}_o^j\right)$ + $\sum_{i=1}^{l}\left(\left(\mathbf{p}_o^i - \mathbf{b}_o\right) \times \mathbf{F}_o^i\right)$. This changes the moment arms from $\mathbf{q}_o^j$ and $\mathbf{p}_o^i$ to $\mathbf{q}_o^j - \mathbf{b}_o$ and $\mathbf{p}_o^i - \mathbf{b}_o$ so that the modified expression represents moments with respect to the arbitrary point *b* rather than fixed point O.

$$\mathbf{M}_o = \sum_{j=1}^{k}\left(\left(\mathbf{q}_o^j - \mathbf{b}_o\right) \times \mathbf{B}_o^j\right) + \sum_{i=1}^{l}\left(\left(\mathbf{p}_o^i - \mathbf{b}_o\right) \times \mathbf{F}_o^j\right) + \left[\sum_{j=1}^{k}\mathbf{b}_o \times \mathbf{B}_o^j + \sum_{i=1}^{l}\mathbf{b}_o \times \mathbf{F}_o^i\right] \tag{3-24}$$

By collecting terms involving $\mathbf{b}_o$, (3-24) can be expressed as (3-25).

$$\mathbf{M}_o = \sum_{j=1}^{k}\left(\left(\mathbf{q}_o^j - \mathbf{b}_o\right) \times \mathbf{B}_o^j\right) + \sum_{i=1}^{l}\left(\left(\mathbf{p}_o^i - \mathbf{b}_o\right) \times \mathbf{F}_o^j\right) + \mathbf{b}_o \times \left[\sum_{j=1}^{k}\mathbf{B}_o^j + \sum_{i=1}^{l}\mathbf{F}_o^i\right] \tag{3-25}$$

Notice that the term $\sum_{j=1}^{k}\mathbf{B}_o^j + \sum_{i=1}^{l}\mathbf{F}_o^i$ in the final cross product of (3-25) is the sum of all forces on the system. According to (3-18), this quantity is equal to $\sum_{i=1}^{l+1} m_i \ddot{\mathbf{c}}_o^i$, which is substituted to result in (3-26).

$$\mathbf{M}_o = \sum_{j=1}^{k}\left(\left(\mathbf{q}_o^j - \mathbf{b}_o\right)\times \mathbf{B}_o^j\right) + \sum_{i=1}^{l}\left(\left(\mathbf{p}_o^i - \mathbf{b}_o\right)\times \mathbf{F}_o^i\right) + \mathbf{b}_o \times \sum_{i=1}^{l+1} m_i \ddot{\mathbf{c}}_o^i \tag{3-26}$$

It is assumed that the first *l+1* of the acting body forces are caused by gravity acting at the c.g. of each system, represented by the vector **g**. This leaves *k-(l+1)* non-gravitational forces acting on the body, as in (3-27).

$$\begin{aligned}\mathbf{M}_o = &\sum_{i=1}^{l+1}\left(\left(\mathbf{c}_o^i - \mathbf{b}_o\right)\times m_i \mathbf{g}_o\right) + \sum_{j=l+2}^{k}\left(\left(\mathbf{q}_o^j - \mathbf{b}_o\right)\times \mathbf{B}_o^j\right) + \\ &\sum_{i=1}^{l}\left(\left(\mathbf{p}_o^i - \mathbf{b}_o\right)\times \mathbf{F}_o^i\right) + \mathbf{b}_o \times \sum_{i=1}^{l+1} m_i \ddot{\mathbf{c}}_o^i\end{aligned} \tag{3-27}$$

Since (3-27) is equivalent to (3-19), conservation of angular momentum is still enforced. By substituting the moments in (3-27) and the change in angular momentum in (3-21) into (3-22), (3-28) is obtained.

$$\begin{aligned}&\sum_{i=1}^{l+1}\left(\left(\mathbf{c}_o^i - \mathbf{b}_o\right)\times m_i \mathbf{g}_o\right) + \sum_{j=l+2}^{k}\left(\left(\mathbf{q}_o^j - \mathbf{b}_o\right)\times \mathbf{B}_o^j\right) + \sum_{i=1}^{l}\left(\left(\mathbf{p}_o^i - \mathbf{b}_o\right)\times \mathbf{F}_o^i\right) + \\ &\mathbf{b}_o \times \sum_{i=1}^{l+1} m_i \ddot{\mathbf{c}}_o^i = \sum_{i=1}^{l+1}\left(\boldsymbol{\omega}_o^i \times \left(\mathbf{R}_o^i \mathbf{I}_i \boldsymbol{\omega}_i\right) + \mathbf{R}_o^i \mathbf{I}_i \dot{\boldsymbol{\omega}}_i\right) + \sum_{i=1}^{l+1} \mathbf{c}_o^i \times m_i \ddot{\mathbf{c}}_o^i\end{aligned} \tag{3-28}$$

Subtracting $\sum_{i=1}^{l+1}\left(\left(\mathbf{c}_o^i - \mathbf{b}_o\right)\times m_i \mathbf{g}_o\right) + \mathbf{b}_o \times \sum_{i=1}^{l+1} m_i \ddot{\mathbf{c}}_o^i$ from both sides results in:

$$\begin{aligned}&\sum_{j=l+2}^{k}\left(\left(\mathbf{q}_o^j - \mathbf{b}_o\right)\times \mathbf{B}_o^j\right) + \sum_{i=1}^{l}\left(\left(\mathbf{p}_o^i - \mathbf{b}_o\right)\times \mathbf{F}_o^i\right) \\ &= \sum_{i=1}^{l+1}\left(\boldsymbol{\omega}_o^i \times \left(\mathbf{R}_o^i \mathbf{I}_i \boldsymbol{\omega}_i\right) + \mathbf{R}_o^i \mathbf{I}_i \dot{\boldsymbol{\omega}}_i\right) + \sum_{i=1}^{l+1}\left(\mathbf{c}_o^i - \mathbf{b}_o\right)\times m_i\left(\ddot{\mathbf{c}}_o^i - \mathbf{g}_o\right)\end{aligned} \tag{3-29}$$

In (3-29), the moment arm of each cross product is measured with respect to the arbitrary point *b*, which will later be chosen as a wheel contact point. All the vectors are still expressed in the coordinates of frame O, however. An arbitrary frame is defined for point *b*, with rotation matrix $\mathbf{R}_b^o$ following the sign convention from [44] described

above. To transform all vectors in (3-29) into the coordinates of arbitrary frame b, both sides of (3-29) are multiplied by $\mathbf{R}_b^o$, as in (3-30).

$$\begin{aligned}&\mathbf{R}_b^o \sum_{j=l+2}^{k}\left(\left(\mathbf{q}_o^j - \mathbf{b}_o\right)\times \mathbf{B}_o^j\right) + \mathbf{R}_b^o \sum_{i=1}^{l}\left(\left(\mathbf{p}_o^i - \mathbf{b}_o\right)\times \mathbf{F}_o^i\right)\\ &= \mathbf{R}_b^o \sum_{i=1}^{l+1}\left(\boldsymbol{\omega}_o^i \times \left(\mathbf{R}_o^i \mathbf{I}_i \boldsymbol{\omega}_i\right) + \mathbf{R}_o^i \mathbf{I}_i \dot{\boldsymbol{\omega}}_i\right) + \mathbf{R}_b^o \sum_{i=1}^{l+1}\left(\mathbf{c}_o^i - \mathbf{b}_o\right)\times m_i\left(\ddot{\mathbf{c}}_o^i - \mathbf{g}_o\right)\end{aligned} \tag{3-30}$$

By distributing the matrix $\mathbf{R}_b^o$ throughout each equation and using the identities $\mathbf{R}_b^o = \mathbf{R}_b^i \mathbf{R}_i^o$, $\boldsymbol{\omega}_i \equiv \mathbf{R}_i^o \boldsymbol{\omega}_o^i$, and $\mathbf{I}_3 = \mathbf{R}_i^o \mathbf{R}_o^i$ where $\mathbf{I}_3$ is the identity matrix, (3-31) is obtained.

$$\begin{aligned}&\sum_{j=l+2}^{k}\left(\mathbf{R}_b^o\left(\mathbf{q}_o^j - \mathbf{b}_o\right)\times \mathbf{R}_b^o \mathbf{B}_o^j\right) + \sum_{i=1}^{l}\left(\mathbf{R}_b^o\left(\mathbf{p}_o^i - \mathbf{b}_o\right)\times \mathbf{R}_b^o \mathbf{F}_o^i\right)\\ &= \sum_{i=1}^{l+1}\left(\mathbf{R}_b^i \boldsymbol{\omega}_i \times \left(\mathbf{R}_b^i \mathbf{I}_i \boldsymbol{\omega}_i\right) + \mathbf{R}_b^i \mathbf{I}_i \dot{\boldsymbol{\omega}}_i\right) + \sum_{i=1}^{l+1}\left(\mathbf{R}_b^o\left(\mathbf{c}_o^i - \mathbf{b}_o\right)\times m_i \mathbf{R}_b^o\left(\ddot{\mathbf{c}}_o^i - \mathbf{g}_o\right)\right)\end{aligned} \tag{3-31}$$

To simplify the notation, further definitions will be made. The output of a body-fixed accelerometer placed at the c.g. of the i^{th} body and expressed in coordinates of the i^{th} frame is $\mathbf{a}_i \equiv \mathbf{R}_i^o\left(\mathbf{g}_o - \ddot{\mathbf{c}}_o^i\right)$. Position vectors measured relative to point b and expressed in frame b are defined as $\mathbf{c}_b^i \equiv \mathbf{R}_b^o\left(\mathbf{c}_o^i - \mathbf{b}_o\right)$, $\mathbf{p}_b^i \equiv \mathbf{R}_b^o\left(\mathbf{p}_o^i - \mathbf{b}_o\right)$, and $\mathbf{q}_b^j \equiv \mathbf{R}_b^o\left(\mathbf{q}_o^j - \mathbf{b}_o\right)$. Force vectors expressed in frame b are defined as $\mathbf{B}_b^j \equiv \mathbf{R}_b^o \mathbf{B}_o^j$ and $\mathbf{F}_b^i \equiv \mathbf{R}_b^o \mathbf{F}_o^i$.

Using the above definitions (3-31) can be expressed more compactly as (3-32). In (3-33), moments caused by non-gravitational body forces are expressed in the right side of the equation.

$$\sum_{j=l+2}^{k}\left(\mathbf{q}_b^j \times \mathbf{B}_b^j\right)+\sum_{i=1}^{l}\left(\mathbf{p}_b^i \times \mathbf{F}_b^i\right)=\sum_{i=1}^{l+1}\mathbf{R}_b^i\left(\boldsymbol{\omega}_i \times\left(\mathbf{I}_i\boldsymbol{\omega}_i\right)+\mathbf{I}_i\dot{\boldsymbol{\omega}}_i\right)+\sum_{i=1}^{l+1}\left(\mathbf{c}_b^i \times m_i\mathbf{R}_b^i\mathbf{a}_i\right) \quad (3\text{-}32)$$

$$\sum_{i=1}^{l}\left(\mathbf{p}_b^i \times \mathbf{F}_b^i\right)=\sum_{i=1}^{l+1}\mathbf{R}_b^i\left(\boldsymbol{\omega}_i \times\left(\mathbf{I}_i\boldsymbol{\omega}_i\right)+\mathbf{I}_i\dot{\boldsymbol{\omega}}_i\right)+\sum_{i=1}^{l+1}\left(\mathbf{c}_b^i \times m_i\mathbf{R}_b^i\mathbf{a}_i\right)-\sum_{j=l+2}^{k}\left(\mathbf{q}_b^j \times \mathbf{B}_b^j\right) \quad (3\text{-}33)$$

Equation (3-33) states that the moments caused by contact forces at an arbitrary point are equivalent to a sum of terms that can be computed from measurements and vehicle parameter estimates that are practical to obtain. The only caveat is that unknown body forces will cause error in the estimation.

With the ability to compute the contact moments with respect to an arbitrary point b with (3-33), a rollover stability measure is defined as the portion of the contact moments acting along a particular tipover axis of the vehicle. To compute this value, the n^{th} tipover axis, $n \in \{1,...,l\}$, must be expressed in the coordinate frame of the n^{th} contact point, as in (3-34). A stability moment SM_n is then defined in (3-35) as the dot product of contact moments computed from (3-33), where b is set to the n^{th} contact point, and the n^{th} tipover axis specified in (3-34). The quantity in (3-35) represents the ground truth of the stability moment, which is not practical to measure directly as it implies direct measurement of the wheel-terrain contact forces $\mathbf{F}_n^i$. An alternative formulation of the stability moment, computed from (3-33) and (3-35), is given in (3-36). This formulation is composed of quantities that are practical to measure.

$$\mathbf{r}_n = \mathbf{R}_n^o\mathbf{r}_o^n \quad (3\text{-}34)$$

$$SM_n^{true} = \left[\sum_{i=1}^{l}\left(\mathbf{p}_n^i \times \mathbf{F}_n^i\right)\right]\cdot \mathbf{r}_n \quad (3\text{-}35)$$

$$SM_n^{meas} = \left[\sum_{i=1}^{l+1} \mathbf{R}_n^i \left(\boldsymbol{\omega}_i \times \left(\mathbf{I}_i \boldsymbol{\omega}_i \right) + \mathbf{I}_i \dot{\boldsymbol{\omega}}_i \right) - \sum_{i=1}^{l+1} \left(\mathbf{c}_n^i \times m_i \mathbf{R}_n^i \mathbf{a}_i \right) - \sum_{j=l+2}^{k} \left(\mathbf{q}_b^j \times \mathbf{B}_b^j \right) \right] \cdot \mathbf{r}_n \quad (3\text{-}36)$$

In (3-36), the term $\boldsymbol{\omega}_i \times \left(\mathbf{I}_i \boldsymbol{\omega}_i \right) + \mathbf{I}_i \dot{\boldsymbol{\omega}}_i$ corresponds to gyroscopic and angular acceleration torques for each body and can be computed with measurements of angular velocity and angular acceleration and an estimate of the inertia matrix of each body. The term $\mathbf{c}_n^i \times m_i \mathbf{R}_n^i \mathbf{a}_i$ corresponds to the moment caused gravitational and inertial force at the c.g. of each body and can be measured with an accelerometer and knowledge of c.g. and contact point positions and an estimate of the mass of each body. The term $\mathbf{q}_b^j \times \mathbf{B}_b^j$ corresponds to moments caused by any additional body forces acting on the system. If any unknown forces $\mathbf{B}_b^j$ are acting, it will cause error in this estimate.

A stability metric is defined to represent the instantaneous stability of the entire vehicle. The metric is defined as the minimum stability moment acting on the vehicle, as in (3-37).

$$\alpha = \min_n \{ SM_n \} \quad (3\text{-}37)$$

To compare the instantaneous stability of different vehicles, the stability moments and stability metric are normalized by α_0, the value of the stability metric for a vehicle at equilibrium on flat ground. The normalized stability moment about the nth axis is given in (3-38) and the normalized stability metric is given in (3-39), with an overbar indicating normalization.

$$\overline{SM_n} = \frac{SM_n}{\alpha_0} \quad (3\text{-}38)$$

$$\overline{\alpha} = \frac{\alpha}{\alpha_0} \tag{3-39}$$

The analysis in this section indicates that the stability moment for passenger vehicles can be measured with accelerometers and rotation rate sensors in conjunction with knowledge of vehicle geometry and any additional body forces acting on the system. The accuracy of these modeling assumptions will be examined in the following section with a passenger utility vehicle. The practicality of measuring stability moments with (3-36) will be addressed thoroughly in Chapter 4.

3.3 Simulation results

Simulation data from the five canonical maneuvers presented in Chapter 1 were used to evaluate the accuracy of the stability moment presented in the previous section. In Section 3.1.1, the stability moment is computed for each canonical maneuver and compared to existing stability measures. In Section 3.3.2, the measurability of the stability moment computed in (3-36) is validated with simulation results from the canonical maneuvers.

3.3.1 Comparison with existing approaches

In this section, the stability moment is compared to other stability measurement techniques mentioned in Chapter 1. First a plot of stability moments about the left and right axes is presented and interpreted in relation to the overall vehicle trajectory and other dynamic states. A stability metric $\overline{\alpha}$ is then computed as the minimum of stability moments about the left and right axes and compared to the existing approaches, which are detailed below. The performance of stability metrics is quantified by time lag and

percentage accuracy in detecting wheel lift-off. Stability about the front and rear tipover axes is not discussed in this section as none of the canonical maneuvers involve pitchover, and the existing stability measures are not sensitive to pitchover.

The existing stability measures to be compared with are load transfer [6, 7], Odenthal's measurable approximation of load transfer [36], critical lateral acceleration [2, 22], and critical roll angle [5, 23]. The form of these metrics is modified slightly so that a value of 1 indicates stability at equilibrium on flat ground, and a zero or negative value indicates instability. This modification enables comparison with the stability moment.

The load transfer metric is typically computed with (3-3), where F_L and F_R represent the sum of front and rear normal forces on the left and right side of the vehicle. This metric takes a value of 0 at equilibrium on flat ground for an axisymmetric vehicle and a value of 1 or -1 at wheel lift-off. Also, this metric is undefined if both F_L and F_R are zero, which occurs when the vehicle is completely off the ground. To enable comparison with the stability moment and mitigate the effect of an undefined value, the metric is defined as the minimum of F_L and F_R, normalized by half the static load on the vehicle as in (3-40).

$$R = \frac{F_L - F_R}{F_L + F_R} \tag{3-3}$$

$$\alpha_R = \min\left\{\frac{2F_L}{mg}, \frac{2F_R}{mg}\right\} \tag{3-40}$$

The Odenthal approximation of load transfer is typically computed with (3-40) where a_y is the measured lateral acceleration, φ is roll angle, and the remaining

parameters are summarized in Table 7. To enable comparison with the stability moment, the Odenthal metric is computed with (3-42).

$$Oden = 2\frac{m_s}{mT}\left(\left(h_r + h\cos\varphi\right)\frac{a_y}{g} + h\sin\varphi\right) \tag{3-41}$$

$$\alpha_{Oden} = \min\{1 + Oden, 1 - Oden\} \tag{3-42}$$

Stability is computed with the critical lateral acceleration and critical roll angle by comparing the measured acceleration a_y or roll angle φ with threshold values specified by a_y^* and ϕ^*. Note that an inclined accelerometer will include some components of gravity. Numerical threshold values for the ADAMS model are given in Table 7. To enable comparison with the stability moment, the critical lateral acceleration and critical roll angle are computed with (3-43) and (3-44).

$$CRa_y = \min\left\{\frac{a_y^* + a_y}{a_y^*}, \frac{a_y^* - a_y}{a_y^*}\right\} \tag{3-43}$$

$$CR\varphi = \min\left\{\frac{\phi^* + \varphi}{\phi^*}, \frac{\phi^* - \varphi}{\phi^*}\right\} \tag{3-44}$$

Parameter	Description	Value
m_s	Sprung mass	2210 kg
m	Total mass	2450 kg
h_r	Suspension roll center height	0 mm
h	Sprung mass height above roll center	770 mm
T	Vehicle width	1620 mm

a_y^*	Lateral accel. threshhold	1.05 g
ϕ^*	Body roll threshhold	4.5°

Table 7: Stability metric parameters

The stability moments for Maneuver 1 are shown in Figure 45 for the left and right tipover axes. At time t_A the vehicle is beginning its initial right turn. As it turns right, the weight shifts onto the opposite side of the vehicle, the left tipover axis. With more weight on the left side than the right side, the contact force moment measured about the left axis will be smaller, while the moment about the right axis will be larger. This can be seen in Figure 45, as SM_{left} decreased slightly from the equilibrium value at time t_A while SM_{right} increased slightly. At time t_B, the vehicle is on the brink of ending its initial right turn with a countersteer. SM_{left} reaches its approximate minimum value for the maneuver at this time, while SM_{right} reaches its approximate maximum value. Between t_B and t_C, the steering is reversed and the vehicle begins to turn left. Since the weight shifts from the left axis to the right axis with the change in path curvature, SM_{left} increases and SM_{right} decreases. For the rest of the maneuver including times t_D and t_E, the vehicle continues its left turn and SM_{left} and SM_{right} remain roughly constant.

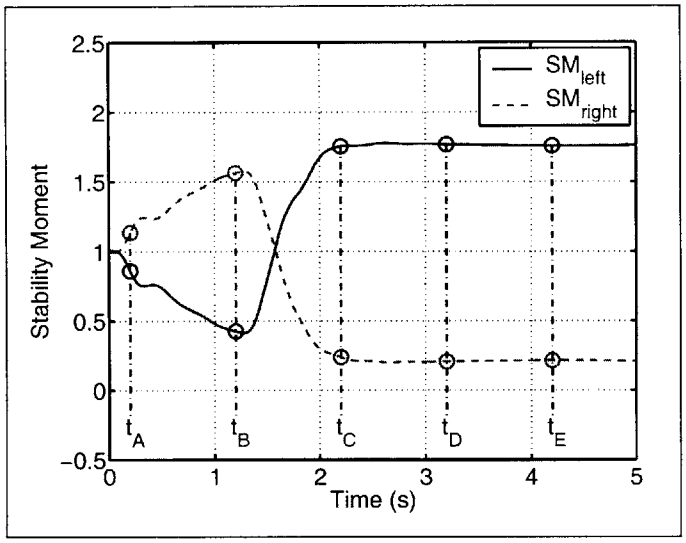

Figure 45: Maneuver 1 Stability Moments

The stability metrics are compared to the ground truth of normal forces F_Z for Maneuver 1 in the figures below. The stability moment metric in Figure 46 lies almost exactly on top of the normal forces, indicating good correspondence. The Odenthal metric in Figure 47, critical lateral acceleration in Figure 48, and critical roll angle in Figure 49 all correspond qualitatively to the normal force plot, though not to the accuracy of stability moments. For practical purposes, all metrics can be considered accurate for this maneuver.

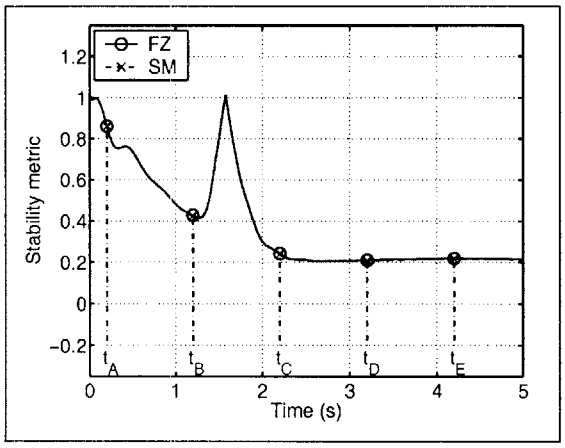

Figure 46: Maneuver 1 Stability Moment Metric

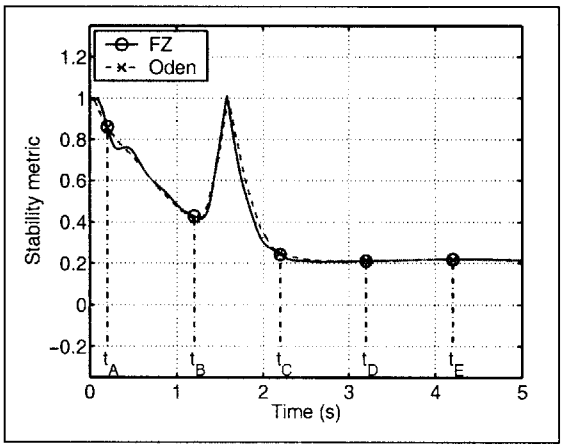

Figure 47: Maneuver 1 Odenthal Metric

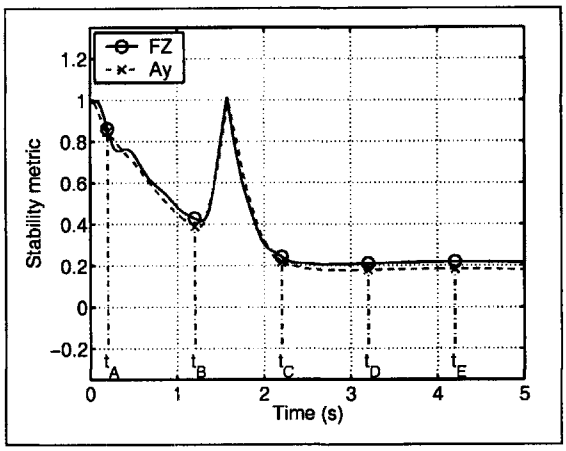

Figure 48: Maneuver 1 Critical Lateral Acceleration

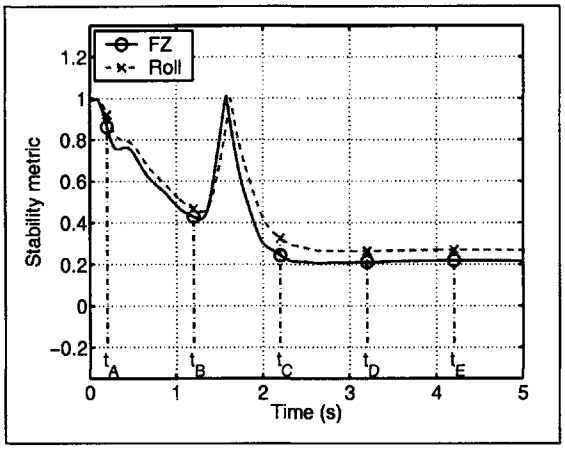

Figure 49: Maneuver 1 Critical Roll Angle

Performance of wheel lift-off detection is measured by the time lag and percent accuracy in identification over the entire maneuver. The ground truth for lift-off is chosen as the times when normal forces are less than 1% of their static value. Hysteresis is used in the lift-off detector to reduce noise sensitivity, with triggering values of 0.01 and 0.10. While the detector performance is sensitive to threshold values, these are chosen to represent reasonable values; determination of optimal threshold values is outside the scope of this thesis. The results of wheel lift-off detection for Maneuver 1 are given in Table 8. Each metric accurately indicated that lift-off did not occur in this maneuver.

Stability measure	Lift-off accuracy	Lift-off detection lag
Stability moment	100.0%	0.00 s
Critical roll	100.0%	0.00 s
Critical accel.	100.0%	0.00 s
Odenthal	100.0%	0.00 s

Table 8: Maneuver 1 Metric Performance

The stability moments for Maneuver 2 are shown in Figure 50 below. The left stability moment initially decreased from t_A to t_B as the vehicle turned right and increased after the countersteer just before t_C. This maneuver occurred at a higher speed than Maneuver 1 and resulted in wheel lift-off at approximately t=2.1 s as the right stability moment reduced to zero. The moment increased briefly just before t_F when the vehicle touched down from its tip-up.

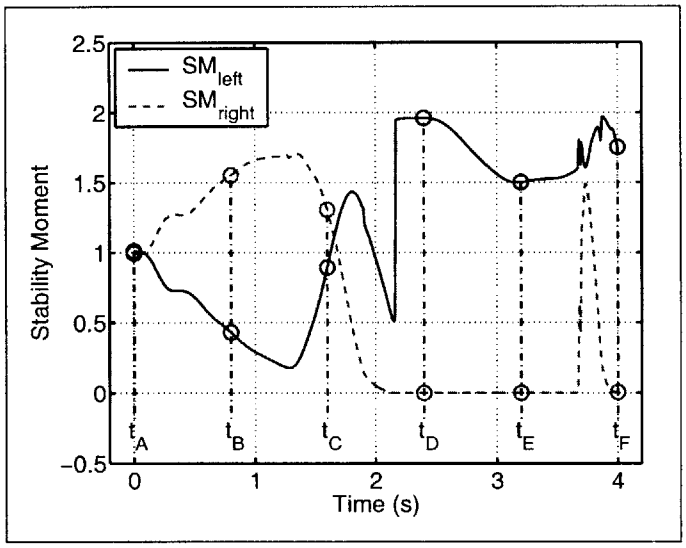

Figure 50: Maneuver 2 Stability Moments

A comparison of the stability moment with other metrics for Maneuver 2 is shown in Figure 51 through Figure 54 below. In Figure 51, the stability moment metric is compared to the normal forces computed in simulation and matches very closely, though the stability moment may indicate lift-off slightly earlier than the normal force method. In Figure 52, the Odenthal metric is seen to not accurately indicate instability for the period of time (approximately 1.5 s) that the wheel is lifted off the ground. In Figure 53, the critical lateral acceleration metric indicates instability at the instant the normal forces go to zero; however the metric increases to a positive value and remains positive for the majority of the lift-off event. In Figure 54, the critical roll angle also indicates instability

at the instant the normal forces go to zero, and it remains negative for the full duration of wheel lift-off.

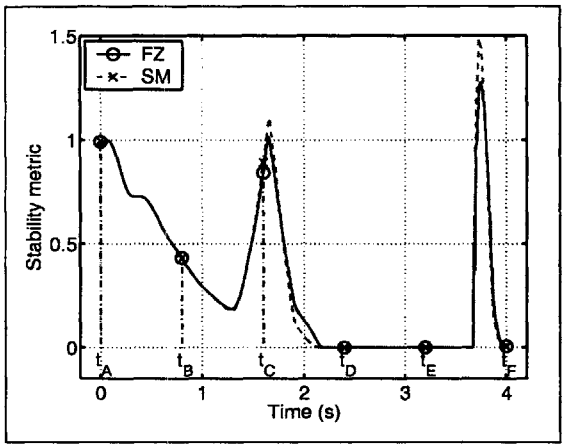

Figure 51: Maneuver 2 Stability Moment Metric

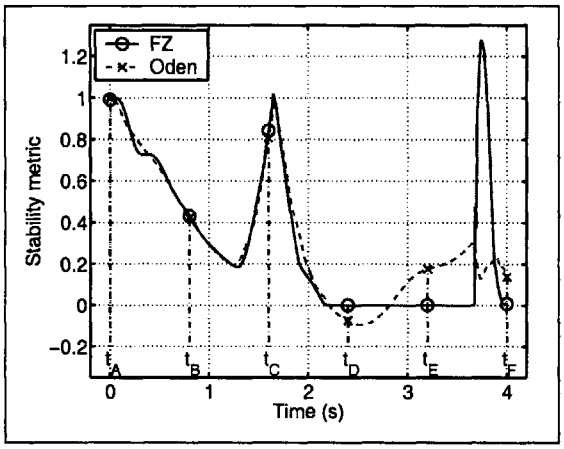

Figure 52: Maneuver 2 Odenthal Metric

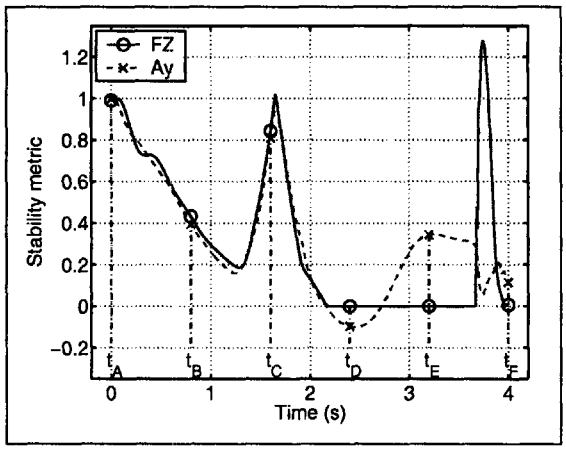

Figure 53: Maneuver 2 Critical Lateral Acceleration

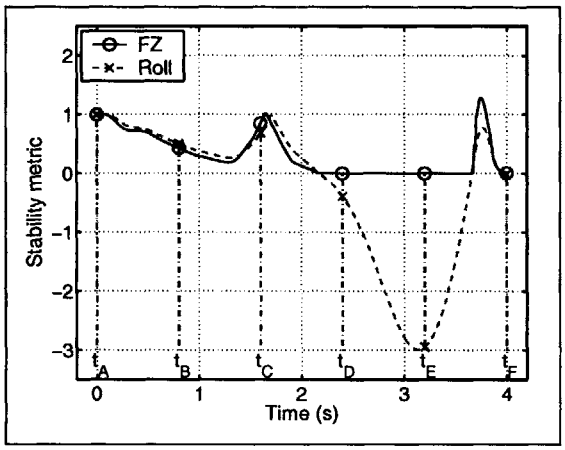

Figure 54: Maneuver 2 Critical Roll Angle

The performance of each metric in detecting wheel lift-off for Maneuver 2 is given in Table 9. In this maneuver, the stability moment and critical roll angle detect lift-off with greater than 98% accuracy. The stability moment has a slightly lower percentage because it indicates lift-off 60 ms early, while the roll angle indicates lift-off 10 ms late. The critical lateral acceleration indicates the beginning of lift-off at the same

time as the critical roll angle, though it does not last for the full duration, leading to less than 75% accuracy. The Odenthal metric does not indicate wheel lift-off at all.

Stability measure	Lift-off accuracy	Lift-off detection lag
Stability moment	98.3%	-0.06 s
Critical roll	99.0%	0.01 s
Critical accel.	77.8%	-0.01 s
Odenthal	80.8%	0.04 s

Table 9: Maneuver 2 Metric Performance

The stability moments for road departure in Maneuver 3 are shown in Figure 55 for the left and right tipover axes. At time t_A the vehicle was traveling straight ahead and the stability moment values were 1.0. At time t_B the vehicle began its right turn, decreasing the left moment and increasing the right moment. Between t_B and t_C, the vehicle fully departed the roadway and initiated a countersteer maneuver, causing the vehicle to turn left. At t_C, the left wheels are about to lift-off as SM_{right} approaches zero. The vehicle proceeds to rollover and SM_{right} remains zero for the duration of the maneuver. Just before t_E, SM_{left} goes to zero. This occurs because the vehicle has tipped up and the contact points are near the line of action of the contact forces.

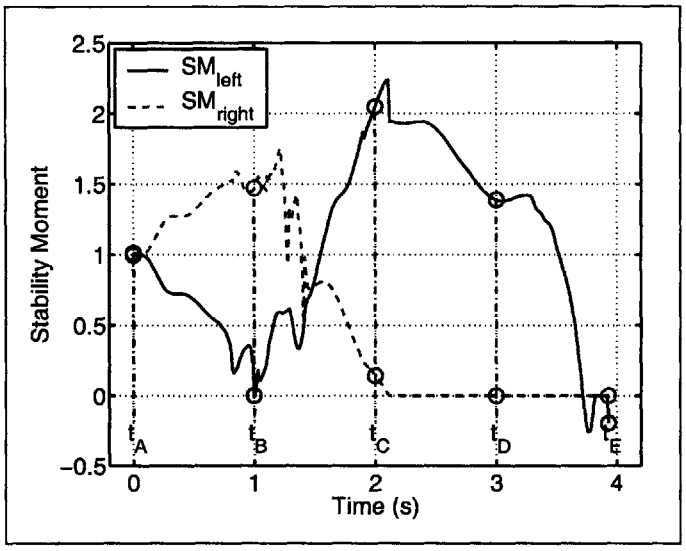

Figure 55: Maneuver 3 Stability Moments

The stability metrics are compared to the computed normal forces for Maneuver 3 in the figures below. Again the metric based on stability moments in Figure 56 corresponds very closely to the computed normal forces. The other metrics, however, show the limitations of the flat ground assumption during road departure. The Odenthal metric in Figure 57 has some correspondence to the computed normal forces for roughly the first 1.75 seconds, but suffers a false negative for the majority of the two second period of the lift-off event. The critical lateral acceleration in Figure 58 shows better correspondence than the Odenthal metric, but it also fails to indicate instability as the vehicle rolls over. The critical roll angle in Figure 59 matches the computed normal forces until the vehicle departs the roadway at t_B, when the metric generates a false positive for a full second when the vehicle is safely traversing the slope.

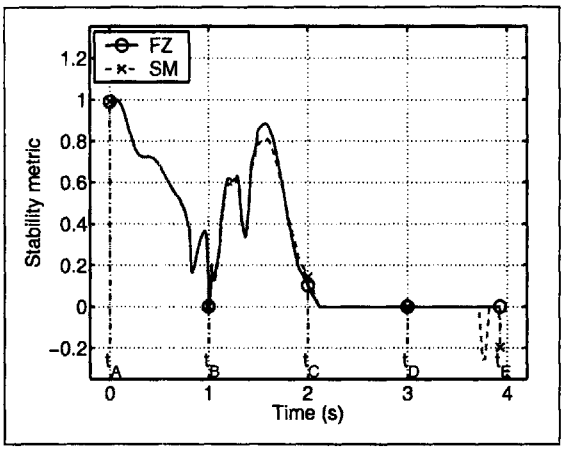

Figure 56: Maneuver 3 Stability Moment Metric

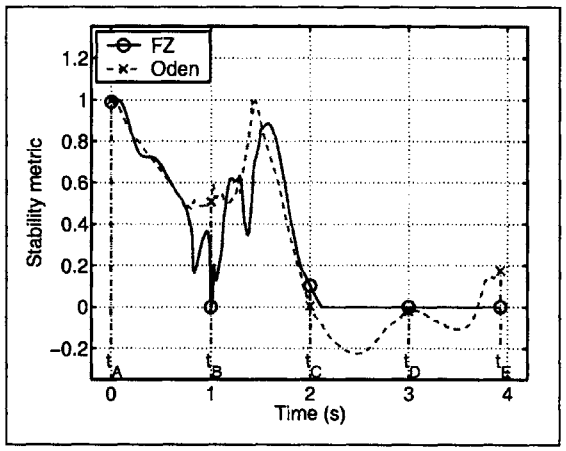

Figure 57: Maneuver 3 Odenthal Metric

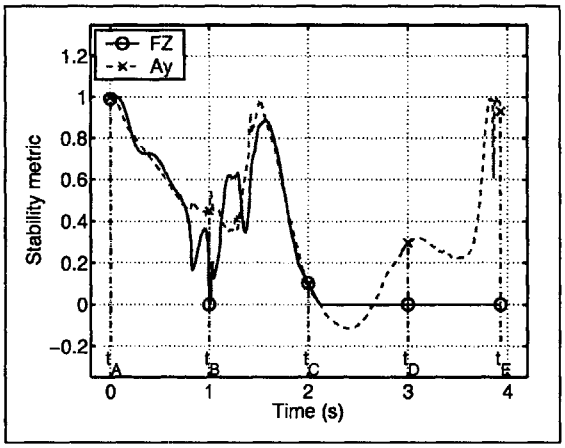

Figure 58: Maneuver 3 Critical Lateral Acceleration

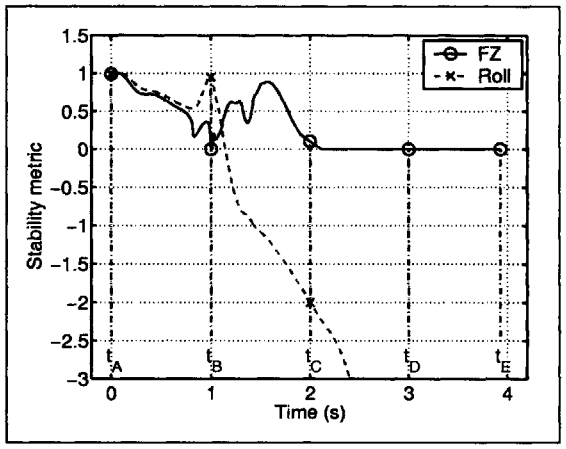

Figure 59: Maneuver 3 Critical Roll Angle

The performance of each metric in detecting wheel lift-off for Maneuver 3 is given in Table 10. In this maneuver, the stability moment detects lift-off with nearly 100% accuracy. The critical roll angle indicates lift-off just after the vehicle departs the roadway, nearly a full second before actual lift-off. The critical lateral acceleration indicates the start of lift-off accurately, but does not indicate the entire duration of lift-off, with a 69.3% accuracy. The Odenthal metric performs better in this maneuver than Maneuver 2, with 92.1% accuracy.

Stability measure	Lift-off accuracy	Lift-off detection lag
Stability moment	99.8%	0.00 s
Critical roll	75.1%	-0.96 s
Critical accel.	69.3%	0.00 s
Odenthal	92.1%	-0.11 s

Table 10: Maneuver 3 Metric Performance

The stability moments for Maneuvers 4 and 5 are shown in Figure 60 and Figure 61. These maneuvers are very similar to Maneuver 3 with the exception of the shoulder roughness included in these tests. The plots are qualitatively similar, though substantial high frequency components appear with increasing roughness. Plots of stability metrics for Maneuvers 4 and 5 is included in Appendix B, and the results are summarized in Table 11 and Table 12.

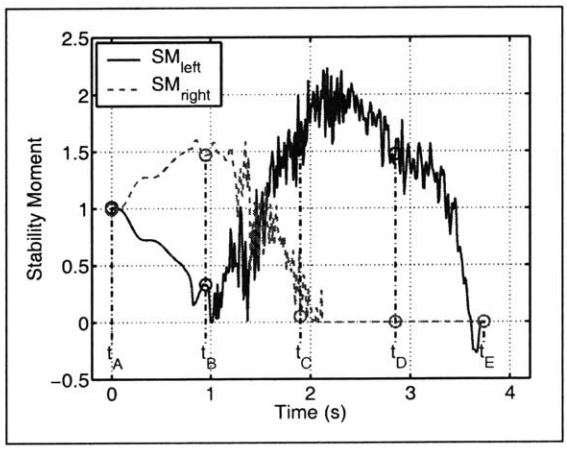

Figure 60: Maneuver 4 Stability Moments

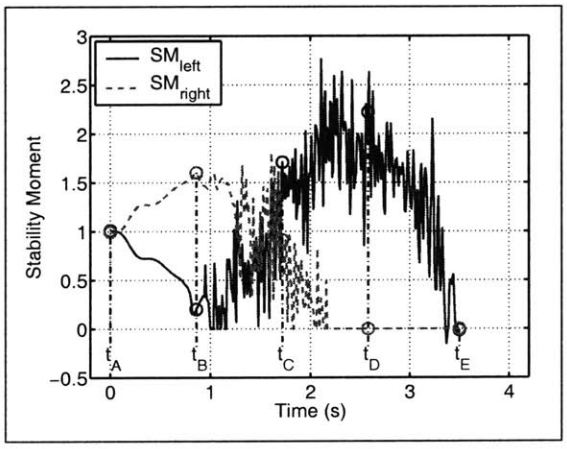

Figure 61: Maneuver 5 Stability Moments

Stability measure	Lift-off accuracy	Lift-off detection lag
Stability moment	99.2%	0.00 s
Critical roll	74.4%	-0.97 s

Critical accel.	70.7%	-0.01 s
Odenthal	94.4%	-0.11 s

Table 11: Maneuver 4 Metric Performance

Stability measure	Lift-off accuracy	Lift-off detection lag
Stability moment	99.7%	0.00 s
Critical roll	73.6%	-1.01 s
Critical accel.	70.9%	0.01 s
Odenthal	84.8%	-0.09 s

Table 12: Maneuver 5 Metric Performance

An average of the stability metric performance over the five maneuvers is given in Table 13.

Stability measure	Lift-off accuracy	Lift-off detection lag
Stability moment	99.4%	-0.01 s
Critical roll	84.4%	-0.59 s
Critical accel.	77.7%	0.00 s
Odenthal	90.4%	-0.05 s

Table 13: Average Metric Performance

The stability metric accurately indicates wheel lift-off with 99.4% accuracy, followed by the Odenthal load transfer approximation with 90.4%. The critical roll angle has reduced accuracy from early lift-off prediction on sloped terrain, and critical lateral acceleration does not indicate lift-off for the entire duration.

3.3.2 Validation of stability moment

In this section the modeling assumptions and derivation of Section 3.2 are validated by computing the stability moments with (3-36) and comparing to the ground truth computed with (3-35). As an example, the measured and true stability moments about the right tipover axis are shown in Figure 34, Figure 35, Figure 64, Figure 65, and Figure 66 for the five maneuvers.

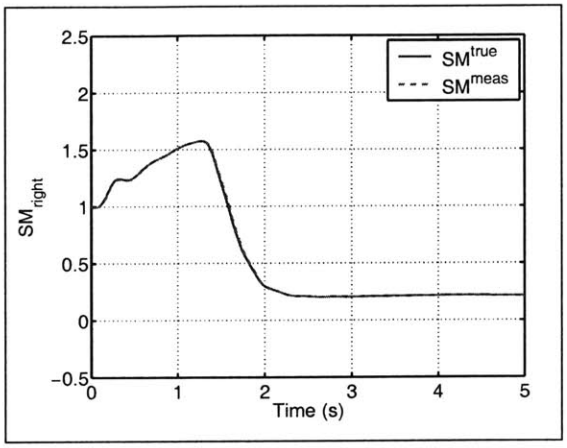

Figure 62: Maneuver 1 SM_{right}

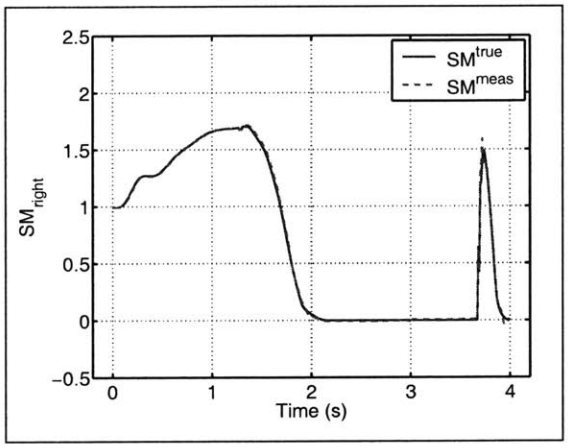

Figure 63: Maneuver 2 SM_{right}

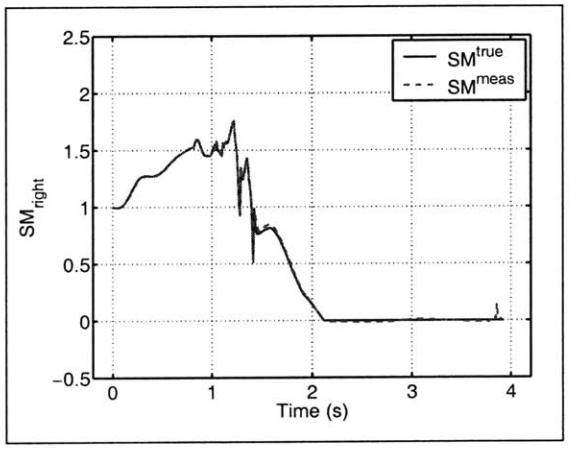

Figure 64: Maneuver 3 SM_{right}

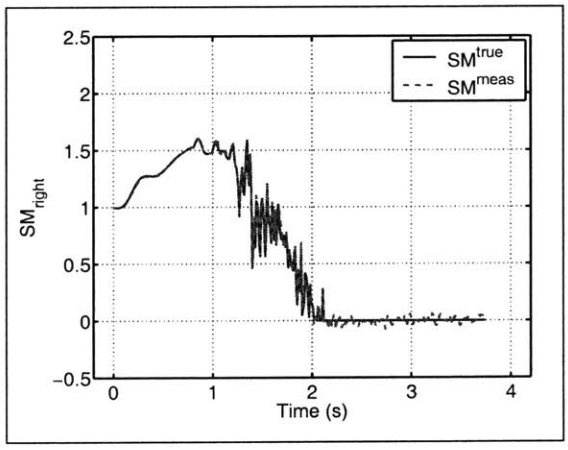

Figure 65: Maneuver 4 SM_{right}

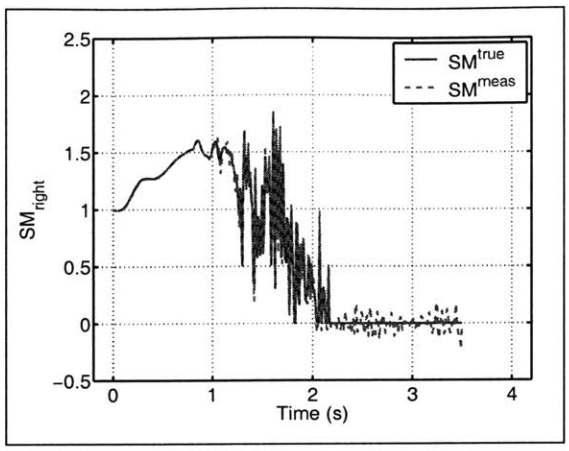

Figure 66: Maneuver 5 SM_{right}

A residual is defined in (3-45) as the difference between true and measured stability moments and computed for each axis of the vehicle for each maneuver. Residuals for the left and right tipover axes of the five maneuvers are plotted in Figure 67, Figure 68, Figure 69, Figure 70, and Figure 71.

$$res_n = \overline{SM}_n^{true} - \overline{SM}_n^{meas} \tag{3-45}$$

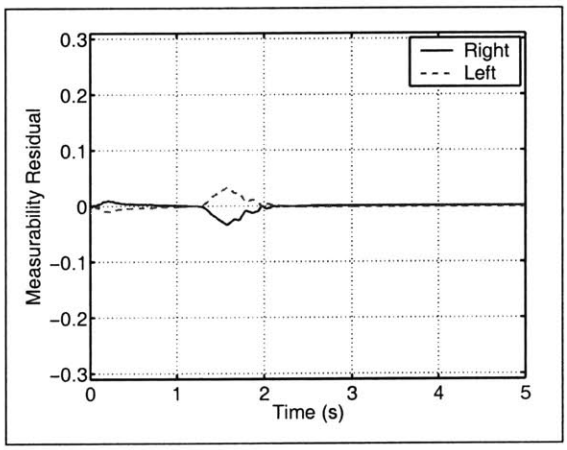

Figure 67: Maneuver 1 Residual

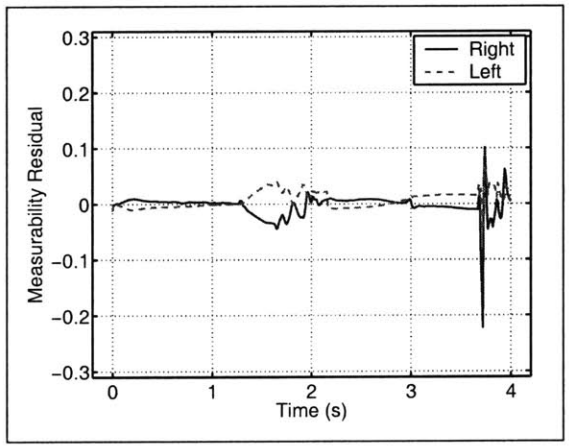

Figure 68: Maneuver 2 Residual

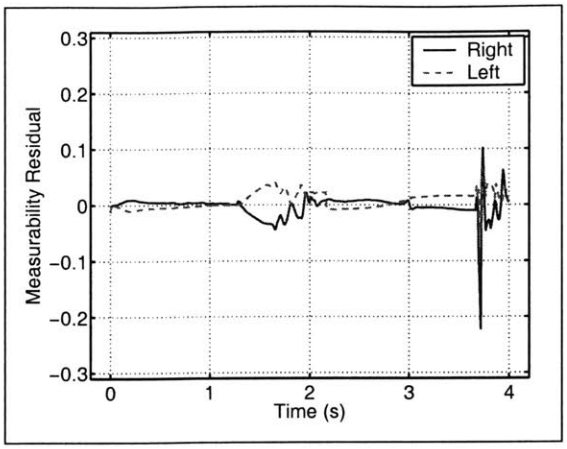

Figure 69: Maneuver 3 Residual

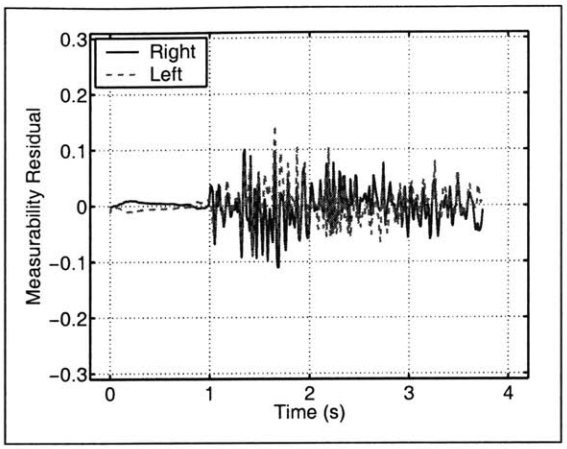

Figure 70: Maneuver 4 Residual

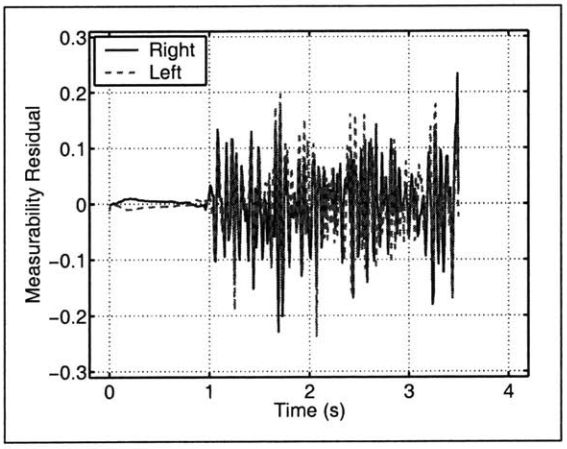

Figure 71: Maneuver 5 Residual

It can be seen that roughness increases the measurability residual in these examples. This is partially due to a software limitation in postprocessing that does not use the exact wheel-terrain contact point to compute stability moments on rough terrain surfaces.

As there are significant high frequency components in the residuals computed for rough terrain, filtering of the stability moment may be useful in these circumstances. To test this effect, the residual was filtered with 1st order lowpass Butterworth filters of several time constants. The original data was sampled every 10 ms, and the time constants ranged from 40 ms to 5 s as shown in Table 14. The maximum value of the

filtered residual for each time constant and axis is shown in Figure 72, Figure 73, Figure 74, and Figure 75 for the four maneuvers.

Filter	1	2	3	4	5	6	7	8
Time constant (s)	0.04	0.08	0.16	0.32	0.64	1.28	2.56	5.12

Table 14: Residual filter time constants

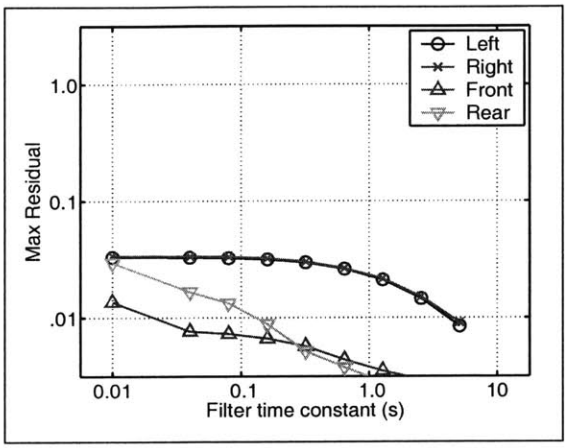

Figure 72: Maneuver 1 Max Residual

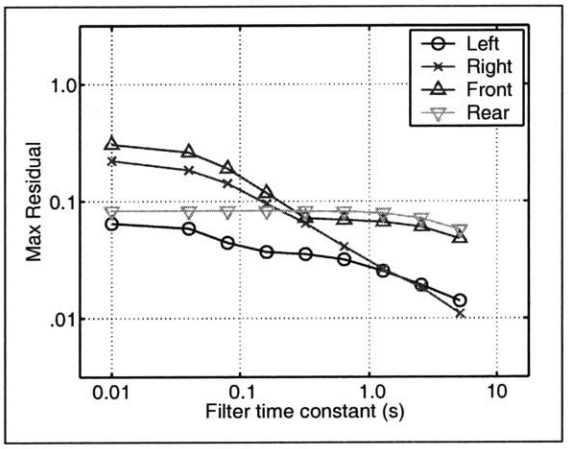

Figure 73: Maneuver 2 Max Residual

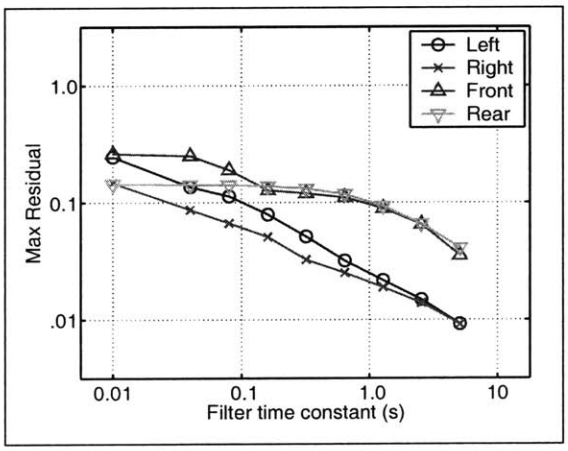

Figure 74: Maneuver 3 Max Residual

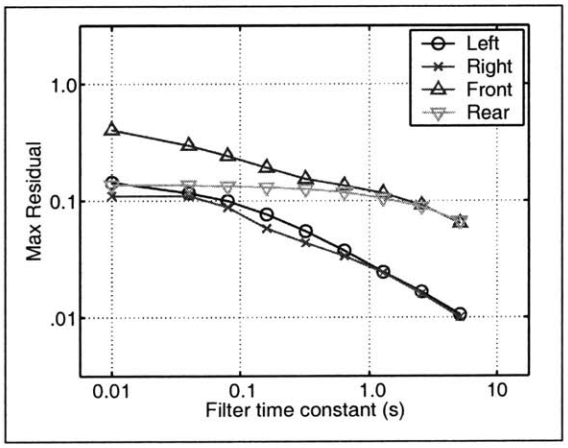

Figure 75: Maneuver 4 Max Residual

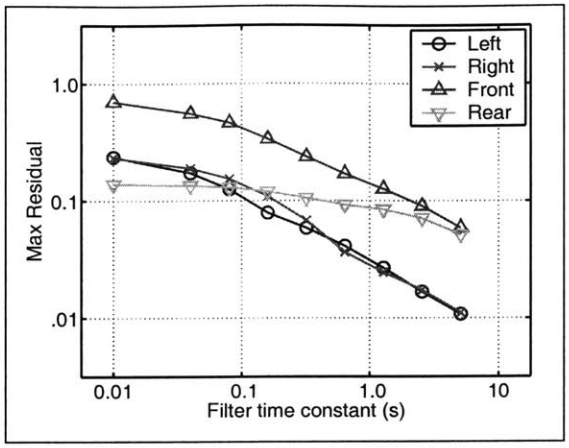

Figure 76: Maneuver 5 Max Residual

As expected, filtering reduced the magnitude of the maximum residual. While the front and rear axes had substantially larger maximum residual for Maneuvers 3-5 than Maneuver 1 and 2, the maximum residual for the left and right axes converged to the same order of magnitude when filtered above 0.64 s. This indicates that the residual errors are largely high frequency, such as the spikes in Figure 69 through Figure 71.

These results indicate that the theoretical basis of the measurable stability moment in (3-36) is sound and that terrain contact moments can be estimated in road departure scenarios involving roughness and rollover, though some filtering may be necessary on rough terrain.

3.4 Experimental results

In this section, the measurable stability moment is shown to correspond to the true stability moment during experimental trials. Two high-speed maneuvers were conducted on flat ground with a high-centered passenger vehicle, during which wheel lift-off was observed. The vehicle parameters are similar to those given in Appendix A. The vehicle was instrumented with an accelerometer and angular velocity sensor on the body and

suspension displacement sensors, and the c.g. position was carefully measured. Gyroscopic terms and wheel acceleration terms were ignored from the computation of stability moments. Since a WFT was not available for this test, the ground truth of wheel lift-off was obtained by observing when the suspension displacement sensor reached its hard stop, indicating that the spring had fully expanded and that the wheel had lifted off.

The first maneuver was a fishhook executed with an initial speed of 85 km/hr. The steering profile and vehicle trajectory are shown in Figure 77 and Figure 78, and the velocity and body roll are shown in Figure 79 and Figure 80. Points of interest are labeled A through F. The throttle was not applied after time t_B, through brakes were applied throughout the maneuver.

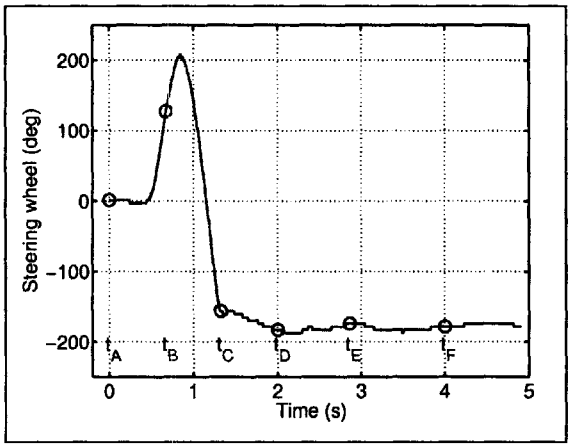

Figure 77: Fishhook Steering Input

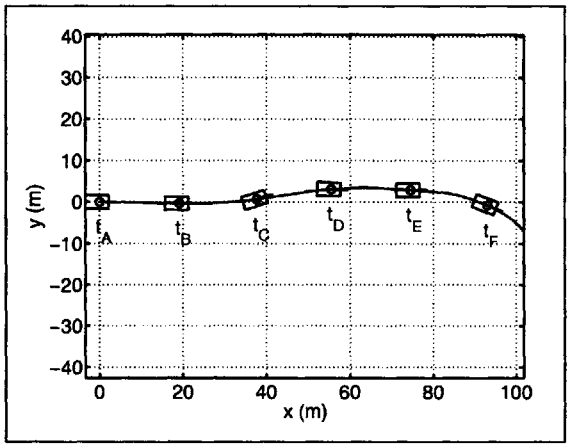

Figure 78: Fishhook Trajectory

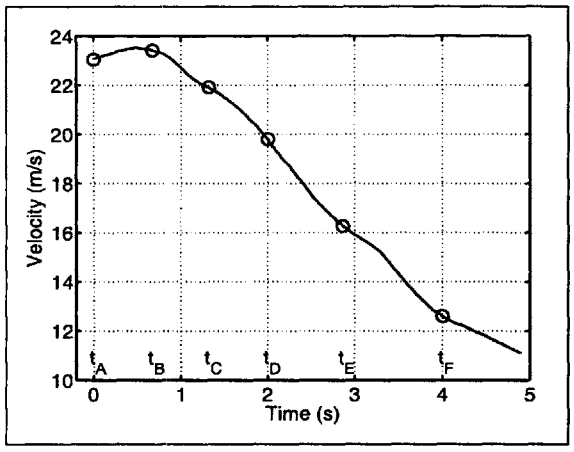

Figure 79: Fishhook Velocity

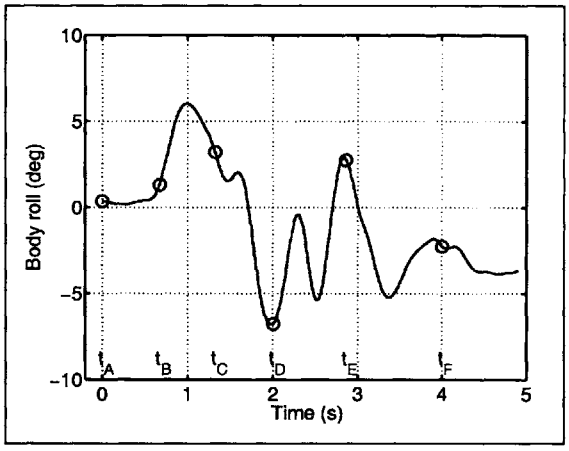

Figure 80: Fishhook Body Roll

The most unstable portion of the maneuver occurred near time t_D, when a full countersteer maneuver had been enacted and the vehicle body roll was near its largest value. The suspension displacement for the left and right wheels is shown in Figure 81, where the plotted values represent the average of front and rear wheels for each side. In this plot, the positive direction corresponds to suspension compression, while the negative direction corresponds to extension. Full extension is reached at 0 mm on this plot. For a short period near time t_D, the right wheels are fully extended, indicating that no contact force was acting on those tires. The stability moments are plotted in Figure 82, and at t_D the stability moment about the left axis is approximately zero with some sensor noise. The lift-off detection method from Section 3.3.1 is applied to this experiment, with the ground truth of lift-off defined to be within 5 mm of the suspension stop. The results are 98.9% lift-off accuracy with a 0.007 s delay.

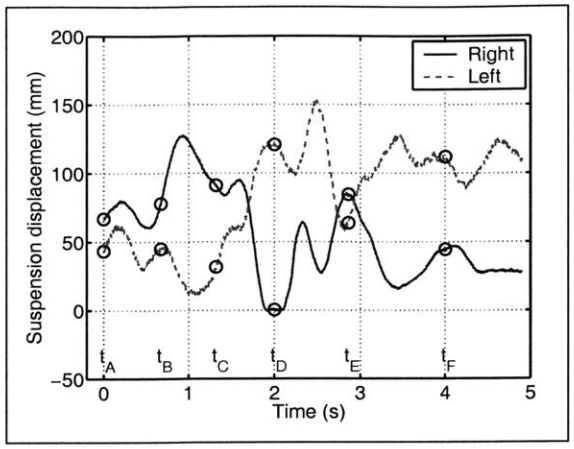

Figure 81: Fishhook Suspension Displacement

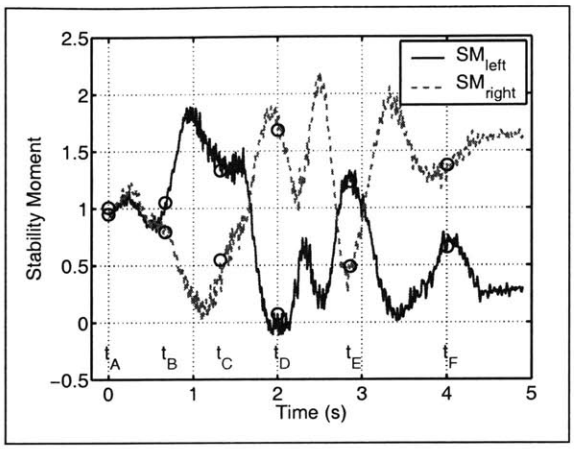

Figure 82: Fishhook Stability Moments

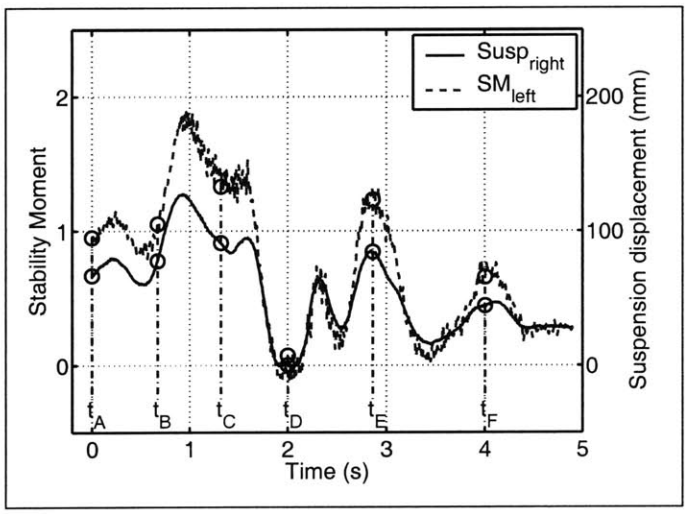

Figure 83: Fishhook Wheel Lift-Off

The second maneuver was a double lane change executed with an initial speed of 75 km/hr. The steering profile and vehicle trajectory are shown in Figure 84 and Figure 85, and the velocity and body roll are shown in Figure 86 and Figure 87. Points of interest are labeled A through G. The throttle was not applied after time t_B, and brakes were not applied at all during the maneuver.

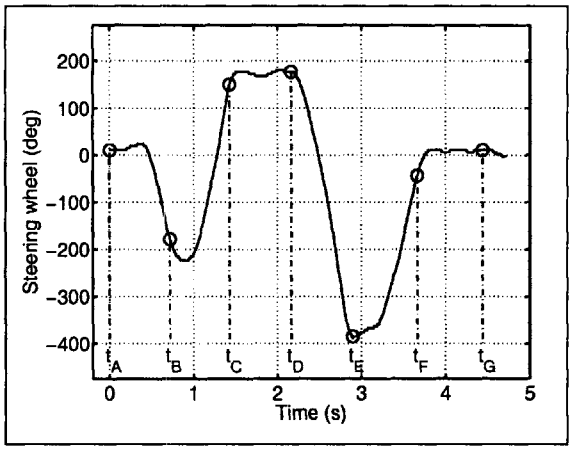

Figure 84: Lane Change Steering Input

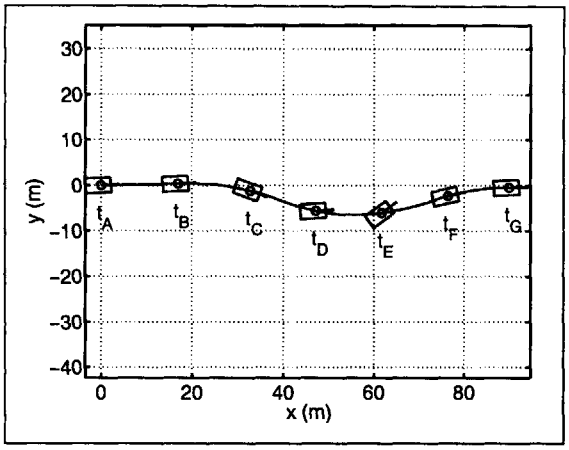

Figure 85: Lane Change Trajectory

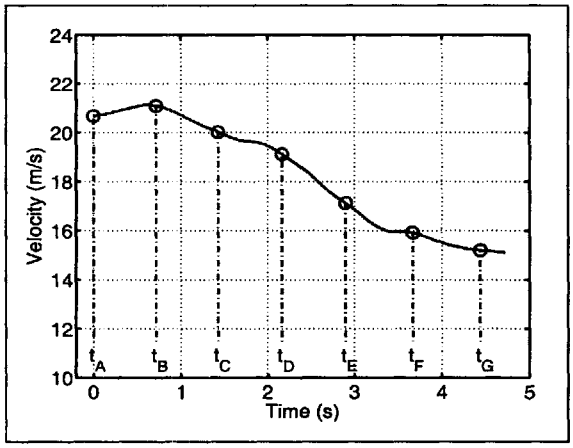

Figure 86: Lane Change Velocity

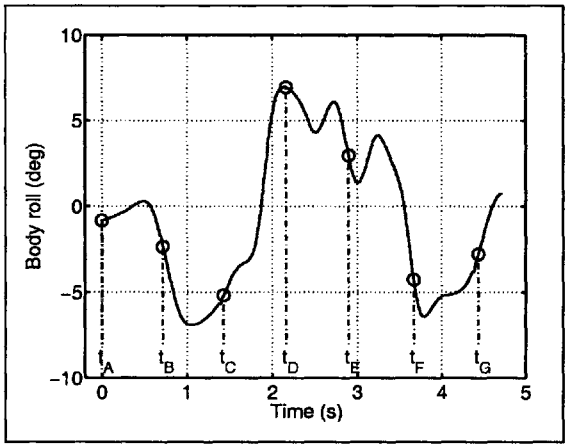

Figure 87: Lane Change Body Roll

There were several periods of instability in this maneuver, particularly between times t_B and t_C and during time t_D. These times correspond to a large steering input from the vehicle and large body roll. The suspension displacement and stability moments are plotted in Figure 88 and Figure 89. Each of these plots indicates that lift-off occurred first for the right wheels between t_B and t_C then for the left wheels at time t_D. The right suspension displacement and left stability moment are shown in Figure 90, and the left suspension displacement and right stability moment are shown in Figure 91. Again, the lift-off detection method from Section 3.3.1 is applied to this experiment, and the results are 96.4% lift-off accuracy with a 0 s delay.

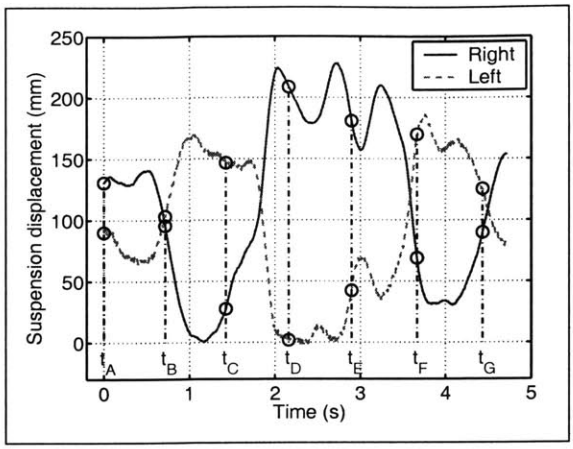

Figure 88: Lane Change Suspension Displacement

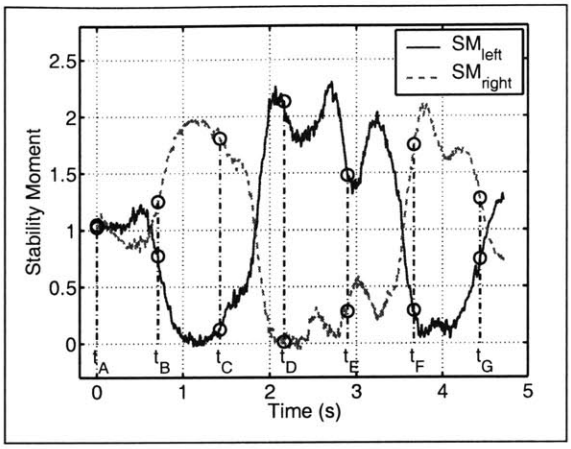

Figure 89: Lane change Stability Moments

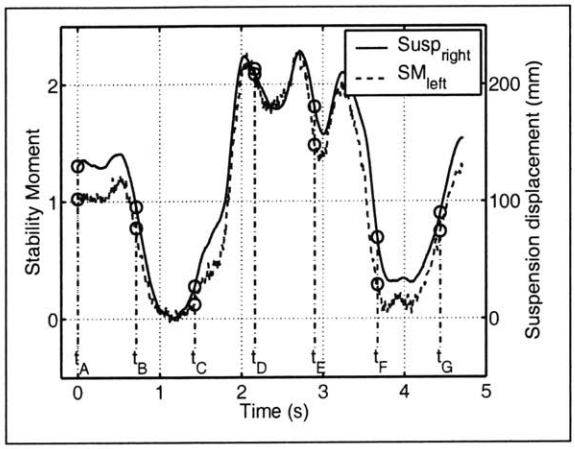

Figure 90: Lane Change Wheel Lift-Off Right

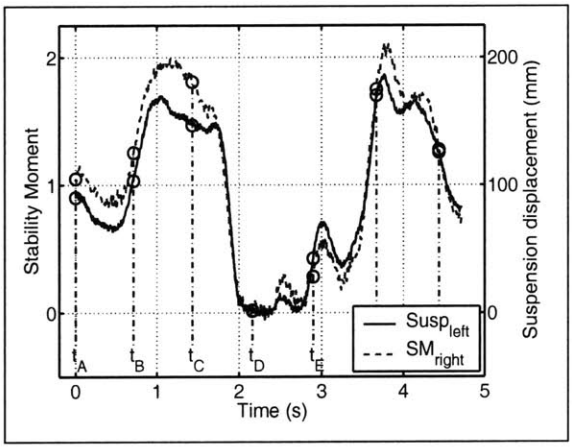

Figure 91: Lane Change Wheel Lift-Off Left

A total of five experiments were conducted in which wheel lift-off was observed. The performance of the stability moment for each test is given in Table 15.

Experiment	Lift-off accuracy	Lift-off detection lag
1	98.9%	0.01 s
2	96.4%	0 s
3	98.5%	0 s
4	98.2%	-0.04 s
5	97.9%	-0.06 s

Average	98.0%	-0.02 s

Table 15: Experimental Lift-off Detection Performance

In these experimental tests, it was observed that the stability moment was able to accurately detect wheel lift-off. This suggests that the measurable stability moment corresponds to the true stability moment defined by contact force moments.

3.5 Conclusion

In this chapter, an instantaneous rollover stability measure was presented that is valid in the presence of sloped, rough, and deformable terrain that would be encountered in a road departure scenario. The metric is based on the moments caused by wheel-terrain contact forces. A measurable form of the metric was derived using the angular momentum principle. The metric was compared to several existing stability measures, and was found to detect wheel lift-off with the highest accuracy rate. The accuracy of the metric was validated with high-fidelity simulation and experimental results.

4

CHAPTER 4: STABILITY MEASURE UNCERTAINTY ANALYSIS

In Chapter 3, an instantaneous measure of vehicle stability was presented that is valid in the presence of terrain slope, roughness, and deformability. In this chapter, the practicality of measuring this quantity for a nominal 4-wheeled high-speed vehicle is assessed by considering the effects of uncertainty in sensing and parameter estimates. In Section 4.1, the uncertainty characteristics of the stability moment about the left and right tipover axes of a 4-wheeled vehicle are studied via sensitivity analysis of a simplified planar vehicle model. In Section 4.2, high-fidelity simulation data is used to verify the results of the uncertainty analysis with a complete vehicle model.

4.1 Uncertainty analysis of simplified model

The stability moment, defined in (3-36) and duplicated in (4-1), was shown to be a useful measure of vehicle stability in Chapter 3. Although all quantities in (4-1) can be measured directly, accurately estimated, or bounded, it is desirable to know the sensitivity of the output to uncertainty in the input parameters and sensed quantities. In the extreme case, this uncertainty would correspond to complete ignorance of some components of (4-1).

$$SM_n^{meas} = \left[\sum_{i=1}^{l+1} \mathbf{R}_n^i \left(\boldsymbol{\omega}_i \times \left(\mathbf{I}_i \boldsymbol{\omega}_i\right) + \mathbf{I}_i \dot{\boldsymbol{\omega}}_i\right) - \sum_{i=1}^{l+1} \left(\mathbf{c}_n^i \times m_i \mathbf{R}_n^i \mathbf{a}_i\right) - \sum_{j=l+2}^{k} \left(\mathbf{q}_b^j \times \mathbf{B}_b^j\right)\right] \cdot \mathbf{r}_n \qquad (4\text{-}1)$$

4.1.1 Simplified planar vehicle model

Since passenger vehicles are much more likely to rollover about the left or right axes than the front or rear, only these axes are considered in the analysis. Since the left and right axes are nearly parallel to the vehicle's roll axis, a planar vehicle model is used to simplify the analysis. The model is shown in Figure 92 with a coordinate system {yz} fixed to the body at point *d*. Bodies 1 and 2 represent the wheels, and body 3 is the chassis. It is assumed that the only body forces acting on the system are caused by gravitational force at the c.g. of each body. A simplified version form of (4-1) for this model is shown in (4-2), where $n \in \{1,2\}$.

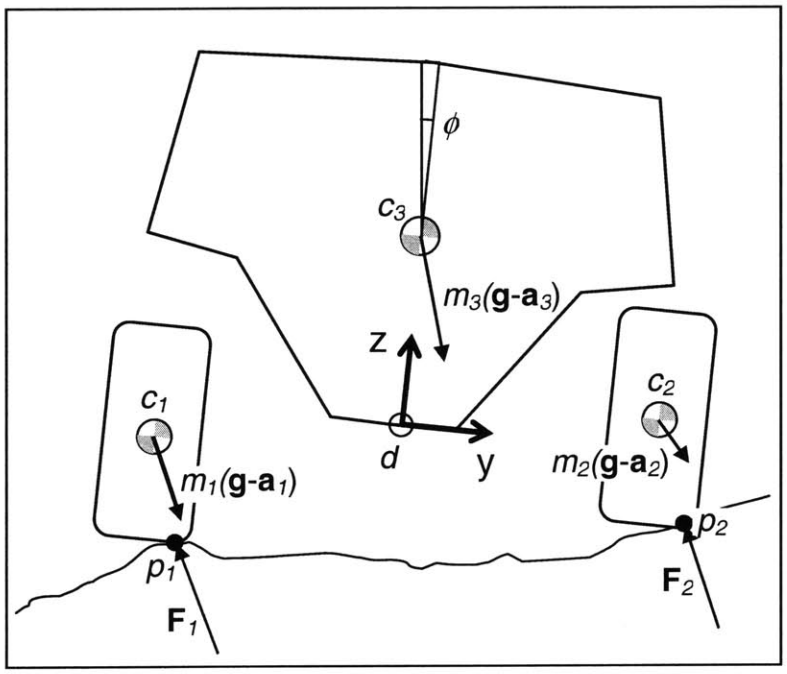

Figure 92: Planar Free Body Diagram

$$SM_n = \sum_{i=1}^{3}\begin{bmatrix}(I_{iz} - I_{iy})\omega_{iy}\omega_{iz} + I_{ix}\dot{\omega}_{ix} + \\ m_i(c_{iy} - p_{ny})(\ddot{c}_{iz} - g\cos\phi) - m_i(c_{iz} - p_{nz})(\ddot{c}_{iy} - g\sin\phi)\end{bmatrix} \quad (4\text{-}2)$$

To determine the relative position vectors used in (4-2), a reference point d is chosen on the body as shown in Figure 92 above. It is assumed that the body c.g. position with respect to d is constant and is given by $\mathbf{c}_b \equiv \mathbf{c}_3 - \mathbf{d}$ in Figure 93. The c.g. positions of the wheels relative to d can be determined with knowledge of suspension displacement and are given by $\mathbf{s}_n \equiv (\mathbf{c}_n - \mathbf{d})$ for $n \in \{1,2\}$ in Figure 93. The locations of the n^{th} wheel contact point relative to the n^{th} wheel c.g. are not easily measurable but are bounded by the size of the tire. They are given by $\mathbf{t}_n \equiv (\mathbf{p}_n - \mathbf{c}_n)$ in Figure 93. With these definitions, the c.g. position of the i^{th} body with respect to contact point n can be computed with (4-3). Note that some simplification of (4-3) occurs when i=n.

$$(\mathbf{c}_i - \mathbf{p}_n) = (\mathbf{c}_i - \mathbf{d}) - \mathbf{s}_n - \mathbf{t}_n \tag{4-3}$$

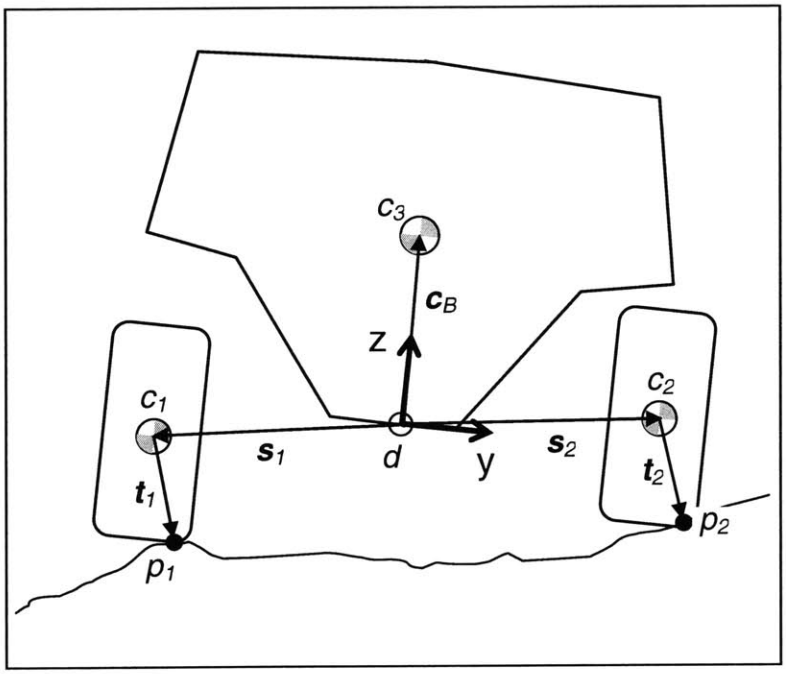

Figure 93: Planar Vehicle Geometry

The components of position vectors $\mathbf{c}_b$, $\mathbf{s}_n$, and $\mathbf{t}_n$ are defined in (4-5), (4-6), and (4-4), respectively. Note that the wheel terrain contact point location in (4-4) is defined

by the equilibrium contact point location $\mathbf{t}_{nz0}$ and the deviation from the equilibrium contact point $\mathbf{t}_{ny}$ and $\mathbf{t}_{nz}$. Additionally, output of a body-fixed accelerometer output is defined as $\mathbf{a}_i \equiv \ddot{\mathbf{c}}_i - \mathbf{g}$ with vector components given in (4-7).

$$\mathbf{c}_b = \begin{bmatrix} 0 \\ c_{by} \\ c_{bz} \end{bmatrix} \tag{4-4}$$

$$\mathbf{s}_n = \begin{bmatrix} 0 \\ s_{ny} \\ s_{nz} \end{bmatrix} \tag{4-5}$$

$$\mathbf{t}_n = \begin{bmatrix} 0 \\ 0 \\ t_{nz0} \end{bmatrix} + \begin{bmatrix} 0 \\ t_{ny} \\ t_{nz} \end{bmatrix} \tag{4-6}$$

$$\mathbf{a}_i = \begin{bmatrix} 0 \\ a_{iy} \\ a_{iz} \end{bmatrix} = \begin{bmatrix} 0 \\ \ddot{c}_{iy} - g\sin\phi \\ \ddot{c}_{iz} - g\cos\phi \end{bmatrix} \tag{4-7}$$

With these definitions, (4-2) becomes (4-8).

$$\begin{aligned} SM_n = \sum_{i=1}^{2} \Big[& \left(I_{iz} - I_{iy}\right)\omega_{iy}\omega_{iz} + I_{ix}\dot{\omega}_{ix} + \\ & m_i\left(s_{iy} - s_{ny} - t_{ny}\right)a_{iz} - m_i\left(s_{iz} - s_{nz} - t_{nz}\right)a_{iy} \Big] + \\ & \left(I_{3z} - I_{3y}\right)\omega_{3y}\omega_{3z} + I_{3x}\dot{\omega}_{3x} + \\ & m_3\left(c_{by} - s_{ny} - t_{ny}\right)a_{3z} - m_3\left(c_{bz} - s_{nz} - t_{nz}\right)a_{3y} \end{aligned} \tag{4-8}$$

As in Chapter 3, the stability moment is normalized by dividing by the static moment on flat ground SM_0 as in (4-9).

$$\overline{SM_n} = \frac{SM_n}{SM_0} \tag{4-9}$$

4.1.2 Uncertainty due to vehicle parameters and sensor uncertainty

With the normalized stability moment equation for the simplified planar vehicle defined in (4-8) and (4-9), the effect of uncertainty in parameters and sensed quantities can be defined.

Parameters in the stability moment equation represent intrinsic vehicle properties and are denoted as k_p, $p \in \{1,...,n_p\}$ and listed in Table 16. Although parameters may vary with loading conditions and fuel consumption, they are assumed to be constant in this analysis. Numerical values for the parameters are given in Appendix C for a light truck passenger vehicle.

p	Variable k_p	Sensitivity S_{kp}^n	Description
1	$I_{iz} - I_{iy}$, $i \in \{1,2\}$	$\omega_{iy}\omega_{iz}$	Wheel gyroscopic inertia
2	$I_{3z} - I_{3y}$	$\omega_{3y}\omega_{3z}$	Chassis gyroscopic inertia
3	I_{ix}, $i \in \{1,2\}$	$\dot{\omega}_{ix}$	Wheel roll inertia
4	I_{3x}	$\dot{\omega}_{3x}$	Chassis roll inertia
5	m_i, $i \in \{1,2\}$	$(s_{iy} - s_{ny} - t_{ny})a_{iz} - (s_{iz} - s_{nz} - t_{nz})a_{iy}$	Wheel mass
6	m_3	$(c_{by} - s_{ny} - t_{ny})a_{3z} - (c_{bz} - s_{nz} - t_{nz})a_{3y}$	Chassis mass
7	$s_{iy} - s_{ny}$	$m_i a_{iz}$	Vehicle width
8	t_{nz0}	$\sum_{i=1}^{3} m_i a_{iy}$	Tire radius
9	$c_{by} - s_{ny}$	$m_3 a_{3z}$	Lateral chassis c.g. position
10	c_{bz}	$-m_3 a_{3y}$	Vertical chassis c.g. position

Table 16: Stability Moment Parameters

Sensed quantities in the stability moment equation represent dynamic states of the vehicle and are denoted as x_s, $s \in \{1,...,n_s\}$ and listed in Table 17. Sensed quantities are not constant like parameters but can vary dynamically within bounds specified by $x_s \in \left[x_s^{\min}, x_s^{\max}\right]$. Numerical values for bounds on sensed quantities are specified in Appendix C for each of the canonical high-speed maneuvers described in Chapter 1.

s	Variable x_s	Sensitivity S_{xs}^n	Description
1	$\omega_{iy}\omega_{iz}$, $i \in \{1,2\}$	$I_{iz} - I_{iy}$	Wheel gyroscopic angular velocity
2	$\omega_{3y}\omega_{3z}$	$I_{3z} - I_{3y}$	Chassis gyroscopic angular velocity
3	$\dot{\omega}_{ix}$, $i \in \{1,2\}$	I_{ix}	Wheel angular acceleration
4	$\dot{\omega}_{3x}$	I_{3x}	Chassis angular acceleration
5	s_{iz}, $i = n$	$m_3 a_{3y}$	Vertical suspension displacement
6	$s_{iz} - s_{nz}$, $i \neq n$	$m_i a_{iy}$	Difference in vertical suspension displacement
7	t_{ny}, $n \in \{1,2\}$	$-\sum_{i=1}^{3} m_i a_{iz}$	Lateral tire contact
8	t_{nz}, $n \in \{1,2\}$	$\sum_{i=1}^{3} m_i a_{iy}$	Vertical tire contact
9	a_{iy}, $i \in \{1,2\}$	$-m_i\left(s_{iz} - s_{nz} - t_{nz}\right)$	Lateral wheel accelerometer
10	a_{iz}, $i \in \{1,2\}$	$m_i\left(s_{iy} - s_{ny} - t_{ny}\right)$	Vertical wheel accelerometer
11	a_{3y}	$-m_3\left(c_{bz} - s_{nz} - t_{nz}\right)$	Lateral chassis accelerometer
12	a_{3z}	$m_3\left(c_{by} - s_{ny} - t_{ny}\right)$	Vertical chassis accelerometer

Table 17: Stability Moment Sensed Quantities

The sensitivity of the stability moment represents the rate at which the stability moment changes for a unit change in a parameter or sensed quantity. In this analysis, first-order sensitivities are considered only, which are defined for each parameter with (4-

10) and for each sensed quantity with (4-11). Parameter sensitivities are listed in Table 16 and sensor sensitivities in Table 17 above. Since the sensed quantities are not constant but lie in a range of values, the sensitivities will also lie in a range of values. For this analysis, the maximum sensitivity value over the entire range will be used.

$$S_{kp}^{n} \equiv \frac{\partial \overline{SM_n}}{\partial k_p} \tag{4-10}$$

$$S_{xs}^{n} \equiv \frac{\partial \overline{SM_n}}{\partial x_s} \tag{4-11}$$

The error in the stability moment attributable to deviation of an estimated parameter value k_p^e from the true value k_p^0 can be computed with (4-12). Likewise, the error in the stability moment attributable to deviation of a sensed quantity x_s^e from the true value x_s^0 can be computed with (4-13).

$$\Delta\overline{SM}_{nkp} = S_{kp}^{n}\left(k_p^e - k_p^0\right) \tag{4-12}$$

$$\Delta\overline{SM}_{nxs} = S_{xs}^{n}\left(x_s^e - x_s^0\right) \tag{4-13}$$

Since parameter values are assumed to be constant, the effect of parameter error is expressed as the change in stability moment caused by 1% parameter error, as computed in (4-14). Sensed quantities, however, vary dynamically throughout a maneuver. For 1% sensor error, the stability moment error will lie in the range specified in (4-15).

$$\Delta\overline{SM}_{nkp}^{1\%} = S_{kp}^{n}\frac{k_p^0}{100} \tag{4-14}$$

$$\Delta\overline{SM}_{nxs}^{1\%} \in \left[\frac{S_{xs}^{n} x_s^{\min}}{100}, \frac{S_{xs}^{n} x_s^{\max}}{100}\right] \tag{4-15}$$

Numerical values for the sensitivities S_{kp}^{n} and S_{xs}^{n} are given in Appendix D along with the nominal parameter values k_p^0 and sensor bounds $\left[x_s^{\min}, x_s^{\max}\right]$ for a flat ground and road departure scenario. The effect of parameter error is shown in Figure 94 and the range of effects of sensor error $\frac{S_{xs}^{n} x_s^{\max}}{100} - \frac{S_{xs}^{n} x_s^{\min}}{100}$ is plotted in Figure 95.

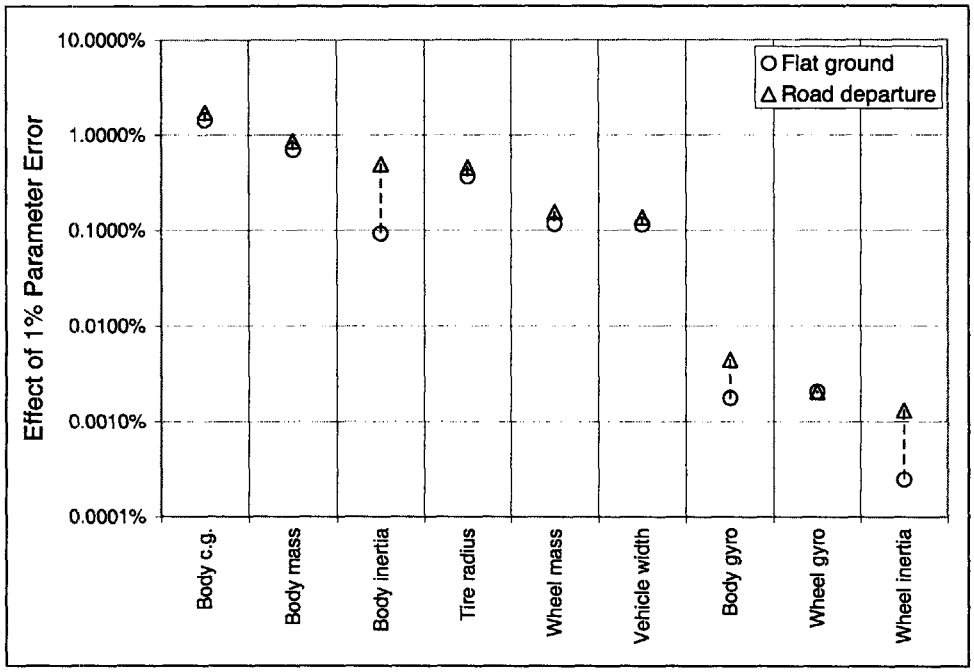

Figure 94: Effect of Parameter Uncertainty

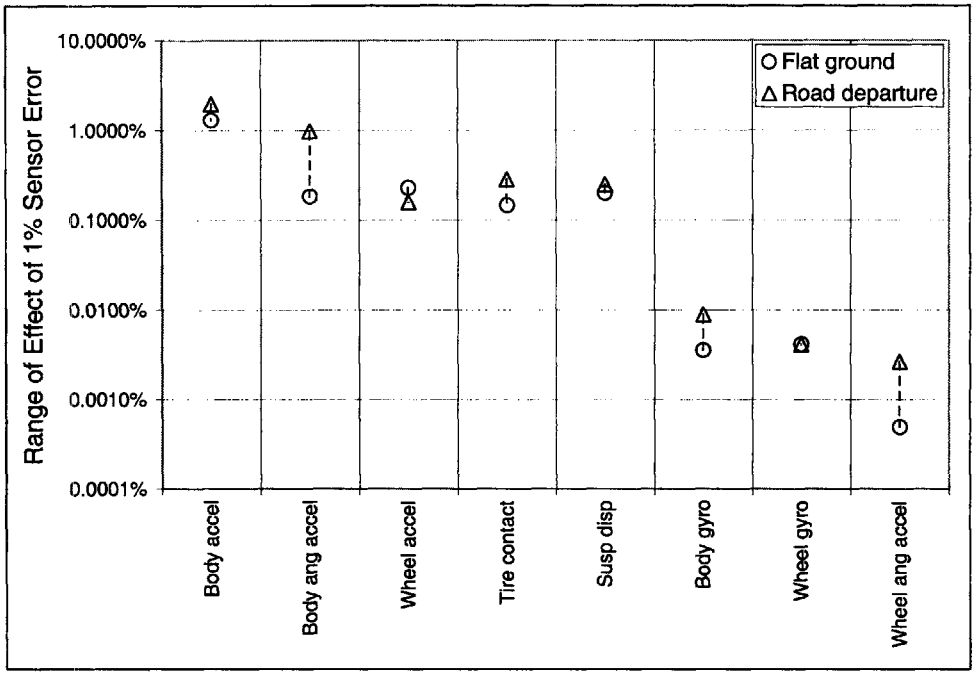

Figure 95: Effect of Sensor Uncertainty

These plots suggest that the angular acceleration of the wheels is the least important term, followed by the wheel and body gyroscopic terms. Ignoring these terms entirely, which is comparable to 100% sensor error, would cause less than 1% output error. The remaining sensed quantities include body acceleration, wheel acceleration, body angular acceleration, suspension displacement, and tire contact location. Since tire contact location sensors are not available, these signals will have 100% error as well, which can correspond to 20% error on flat ground or 25% error in road departure, which is substantial. The actual effect of variation in tire contact location will be evaluated with simulation data in Section 4.2.

The results above indicate that lack of wheel acceleration sensors will cause similar error to lack of suspension displacement or tire contact sensors. Even if a wheel acceleration sensor is not available, an estimate of wheel acceleration can be taken from the body acceleration sensor to mitigate the lack of the sensor. The effect of this

approximation and several other details of acceleration measurement are discussed in the next section.

4.1.3 Uncertainty in acceleration measurement

The analysis of the previous section suggested that ignoring wheel acceleration terms would cause substantial error in the stability moment. The error caused by lack of wheel acceleration sensor can be mitigated by using the body acceleration measurement, which is very likely to be available. Additionally, the output of acceleration sensors varies with their location on a body. The effect of this sensor placement effect will be evaluated as well.

The relationship between body acceleration and wheel acceleration is derived below. Point b in Figure 96 represents the location of the body accelerometer and point c_i the position of the wheel c.g. Vectors $\mathbf{b}_o$ and $\mathbf{c}_o$ give the location of points b and c_i with respect to fixed point O, and the vector $\mathbf{c}_b$ gives the location of c_i relative to b. The relation between $\mathbf{c}_o$, $\mathbf{b}_o$, and $\mathbf{c}_b$ is given in (4-16), where $\mathbf{R}_0^b$ is the rotation matrix for the orientation of the coordinate frame in which $\mathbf{c}_b$ is expressed.

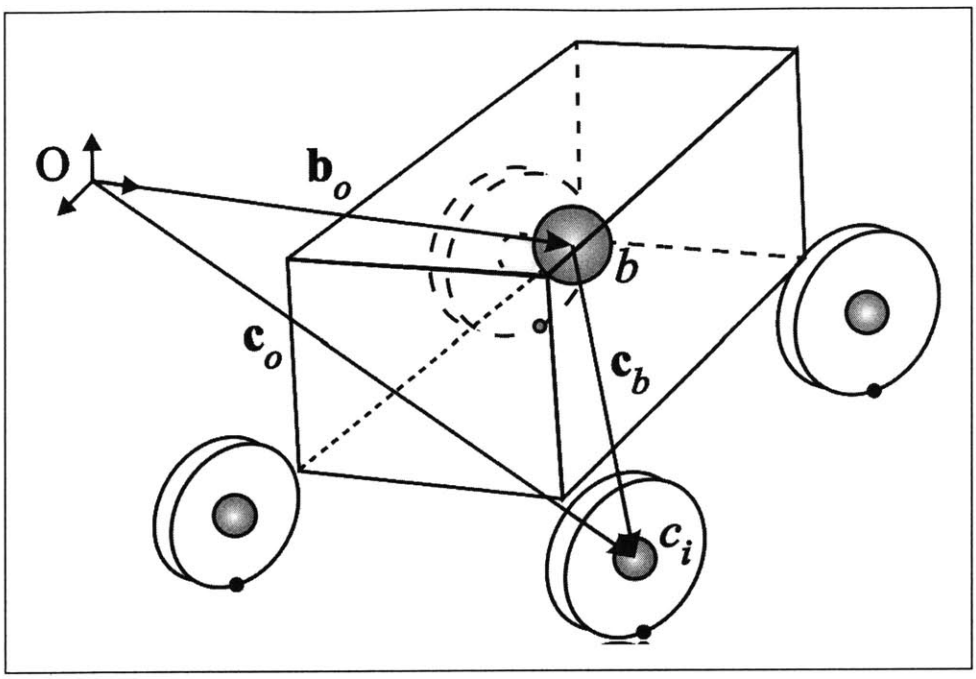

Figure 96: Wheel Position Relative to Body

$$\mathbf{c}_o = \mathbf{b}_o + \mathbf{R}_0^b \mathbf{c}_b \tag{4-16}$$

Differentiating (4-16) with respect to time yields (4-17), and (4-18) can be found by recalling the property of rotation matrices $\dot{\mathbf{R}}_o^i \mathbf{x}_i = \boldsymbol{\omega}_o^i \times \mathbf{R}_o^i \mathbf{x}_i$ given in Chapter 3.

$$\dot{\mathbf{c}}_o = \dot{\mathbf{b}}_o + \dot{\mathbf{R}}_0^b \mathbf{c}_b + \mathbf{R}_0^b \dot{\mathbf{c}}_b \tag{4-17}$$

$$\dot{\mathbf{c}}_o = \dot{\mathbf{b}}_o + \boldsymbol{\omega}_0^b \times \mathbf{R}_0^b \mathbf{c}_b + \mathbf{R}_0^b \dot{\mathbf{c}}_b \tag{4-18}$$

Differentiation of (4-18) yields (4-19), and subsequent substitution for $\dot{\mathbf{R}}_0^b$ yields (4-20).

$$\ddot{\mathbf{c}}_o = \ddot{\mathbf{b}}_o + \dot{\boldsymbol{\omega}}_0^b \times \mathbf{R}_0^b \mathbf{c}_b + \boldsymbol{\omega}_0^b \times \left(\dot{\mathbf{R}}_0^b \mathbf{c}_b + \mathbf{R}_0^b \dot{\mathbf{c}}_b\right) + \dot{\mathbf{R}}_0^b \dot{\mathbf{c}}_b + \mathbf{R}_0^b \ddot{\mathbf{c}}_b \tag{4-19}$$

$$\ddot{\mathbf{c}}_o = \ddot{\mathbf{b}}_o + \dot{\boldsymbol{\omega}}_0^b \times \mathbf{R}_0^b \mathbf{c}_b + \boldsymbol{\omega}_0^b \times \left(\boldsymbol{\omega}_0^b \times \mathbf{R}_0^b \mathbf{c}_b\right) + 2\boldsymbol{\omega}_0^b \times \mathbf{R}_0^b \dot{\mathbf{c}}_b + \mathbf{R}_0^b \ddot{\mathbf{c}}_b \tag{4-20}$$

Equation (4-20) gives an expression for the wheel acceleration in terms of the body acceleration $\ddot{\mathbf{b}}_o$ and secondary acceleration effects: sensor placement $\dot{\boldsymbol{\omega}}_0^b \times \mathbf{R}_0^b \mathbf{c}_b + \boldsymbol{\omega}_0^b \times \left(\boldsymbol{\omega}_0^b \times \mathbf{R}_0^b \mathbf{c}_b\right)$ and suspension dynamics $2\boldsymbol{\omega}_0^b \times \mathbf{R}_0^b \dot{\mathbf{c}}_b + \mathbf{R}_0^b \ddot{\mathbf{c}}_b$. With the components of the sensor placement acceleration $\mathbf{a}_{sp}$ defined in (4-21), the y and z components can be computed with (4-22) and (4-23). Likewise, components of the suspension dynamics acceleration $\mathbf{a}_{sd}$ are defined in (4-24), and the y and z components can be computed with (4-25) and (4-26).

$$\mathbf{a}_{sp} \equiv \begin{bmatrix} a_{sp}^x \\ a_{sp}^y \\ a_{sp}^z \end{bmatrix} = \dot{\boldsymbol{\omega}}_0^b \times \mathbf{R}_0^b \mathbf{c}_b + \boldsymbol{\omega}_0^b \times \left(\boldsymbol{\omega}_0^b \times \mathbf{R}_0^b \mathbf{c}_b\right) \tag{4-21}$$

$$a_{sp}^y = \dot{\omega}_0^{bz} c_b^x - \dot{\omega}_0^{bx} c_b^z - \left(\left(\omega_0^{bx}\right)^2 + \left(\omega_0^{bz}\right)^2\right) c_b^y + \omega_0^{bx} \omega_0^{by} c_b^x + \omega_0^{by} \omega_0^{bz} c_b^z \tag{4-22}$$

$$a_{sp}^z = \dot{\omega}_0^{bx} c_b^y - \dot{\omega}_0^{by} c_b^x - \left(\left(\omega_0^{bx}\right)^2 + \left(\omega_0^{by}\right)^2\right) c_b^z + \omega_0^{bx} \omega_0^{bz} c_b^x + \omega_0^{by} \omega_0^{bz} c_b^y \tag{4-23}$$

$$\mathbf{a}_{sd} \equiv \begin{bmatrix} a_{sd}^x \\ a_{sd}^y \\ a_{sd}^z \end{bmatrix} = 2\boldsymbol{\omega}_0^b \times \mathbf{R}_0^b \dot{\mathbf{c}}_b + \mathbf{R}_0^b \ddot{\mathbf{c}}_b \tag{4-24}$$

$$a_{sd}^y = 2\omega_0^{bz} \dot{c}_b^x - 2\omega_0^{bx} \dot{c}_b^z + \ddot{c}_b^y \tag{4-25}$$

$$a_{sd}^z = 2\omega_0^{bx} \dot{c}_b^y - 2\omega_0^{by} \dot{c}_b^x + \ddot{c}_b^z \tag{4-26}$$

Nominal bounds on the dynamic states that influence computation of secondary wheel accelerations are given in Table 18 for flat ground and road departure. With these bounds, the magnitude of secondary wheel accelerations can be bounded as well.

x	Description	Flat ground max	Road depart max
$\dot{\omega}_0^{bx}$	Angular acceleration roll	1.5 rad/s^2	8 rad/s^2
$\dot{\omega}_0^{by}$	Angular acceleration pitch	0.2 rad/s^2	3 rad/s^2
$\dot{\omega}_0^{bz}$	Angular acceleration yaw	2.5 rad/s^2	4 rad/s^2
ω_0^{bx}	Angular velocity roll	0.5 rad/s	1 rad/s
ω_0^{by}	Angular velocity pitch	0.2 rad/s	0.4 rad/s
ω_0^{bz}	Angular velocity yaw	0.8 rad/s	1.0 rad/s
c_b^x	Wheel position longitudinal	1.4 m	1.4 m
c_b^y	Wheel position lateral	0.81 m	0.81 m
c_b^z	Wheel position vertical	0.51 m	0.51 m
$\dot{c}_b^x$	Wheel velocity longitudinal	0 m/s	0 m/s
$\dot{c}_b^y$	Wheel velocity lateral	0 m/s	0 m/s
$\dot{c}_b^z$	Wheel velocity vertical	0.6 m/s	0.75 m/s
$\ddot{c}_b^x$	Wheel acceleration longitudinal	0 m/s^2	0 m/s^2
$\ddot{c}_b^y$	Wheel acceleration lateral	0 m/s^2	0 m/s^2
$\ddot{c}_b^z$	Wheel acceleration vertical	3 m/s^2	6 m/s^2

Table 18: Bounds on States for Secondary Wheel Acceleration

With these bounds placed on the dynamic states, the maximum sensor placement and suspension dynamics acceleration can be computed for the flat ground and road departure case. These values are given in Table 19.

x	Description	Flat ground	Road depart

a_{sp}^{y}	Sensor placement lateral	0.43 g	0.67 g
a_{sp}^{z}	Sensor placement vertical	0.24 g	0.78 g
a_{sd}^{y}	Suspension dynamics lateral	0.08 g	0.20 g
a_{sd}^{z}	Suspension dynamics vertical	0.30 g	0.60 g

Table 19: Bounds on Secondary Wheel Accelerations

Using the sensitivities computed in the previous section, the output error induced by 100% error in these acceleration quantities can be computed and is given in Table 20.

x	Description	Flat ground	Road depart
$S_x a_{sp}^{y}$	Sensor placement lateral	0.7%	1.1%
$S_x a_{sp}^{z}$	Sensor placement vertical	2.4%	8.2%
$S_x a_{sd}^{y}$	Suspension dynamics lateral	0.1%	0.3%
$S_x a_{sd}^{z}$	Suspension dynamics vertical	3.0%	6.3%
	Total	6.3%	15.9%

Table 20: Bounds on Effect of Secondary Wheel Accelerations

The expected error for complete ignorance of wheel acceleration was 13% for flat ground and 24% for road departure. Using body acceleration reduces that error to 7% on flat ground and 9% in road departure.

An additional consideration for measurement of acceleration is the location of the sensor. Accurate computation of the stability moment requires the acceleration of each body to be measured at the body c.g. The change in measured acceleration caused by sensor misplacement is given by (4-21). This effect is most pronounced for the body

acceleration, since it is often impractical or impossible to place an accelerometer exactly at the body c.g.

The effect of misplacing the body acceleration sensor can be estimated by assuming that the sensor is placed along the vector $\mathbf{c}_b$ defined in Figure 96. This allows the use of acceleration magnitudes given in Table 19. Assuming the sensor lies 10% of the length of $\mathbf{c}_b$ away from the body c.g. and using sensitivity values from Section 4.1.2 given in Appendix D the effect of misplacing the body accelerometer can be computed and is given in Table 21.

x	Description	Flat ground	Road depart
$S_x a_{sp}^y$	Sensor placement lateral	2.6%	4.0%
$S_x a_{sp}^z$	Sensor placement vertical	2.2%	7.6%
	Total	4.8%	11.6%

Table 21: Effect of 10% Misplacement of Body Accelerometer

In this section, the effects of sensing and parameter uncertainty were assessed for a planar vehicle model. Body acceleration and c.g. position were found to be the most significant sensor and parameter respectively.

4.2 Simulation results

The performance in measuring stability moments of various sensor sets is assessed here with simulation data from the canonical maneuvers described in Chapter 1 and detailed in Appendix B. The sensor sets to be evaluated are given in Table 22 with an X indicating inclusion in the set.

Sensor Set	Body accel.	Body angular accel.	Susp. disp.	Wheel Accel.	Gyroscopic and wheel inertia	Tire contact
0	X	X	X	X	X	X
1	X	X	X	X	X	
2	X	X	X	X		
3	X	X	X			
4	X	X		X		
5	X		X	X		

Table 22: Sensor Sets

Set 0 utilizes every sensor required in (4-1) and represents the best measurement possible. Set 1 utilizes all sensed quantities except tire contact location, which is the most difficult to obtain. Set 1 represents the best measurement possible with practical sensors. Set 2 is similar to Set 1 with the exception of gyroscopic and angular acceleration terms, which were predicted to have little effect on the stability moment in the previous section. Sets 3-5 take Set 2 as a baseline and wheel acceleration, suspension displacement, and body angular acceleration individually to see the relative importance of each sensor. Body acceleration is included in all sensor sets because it is the most dominant term.

When a sensor is not available in this analysis, a reasonable approximation based on the available sensors is made. In Sets 1-5, the tire contact point is assumed to lie at the nominal contact position at equilibrium on flat ground, in the middle of the tire. In Set 3, body acceleration is used in place of wheel acceleration. In Set 4, the suspension is assumed to be compressed 50 mm out of the full compression of 100 mm. As an example, the stability moments measured by each sensor set for Maneuver 3 are shown in Figure 97 through Figure 102.

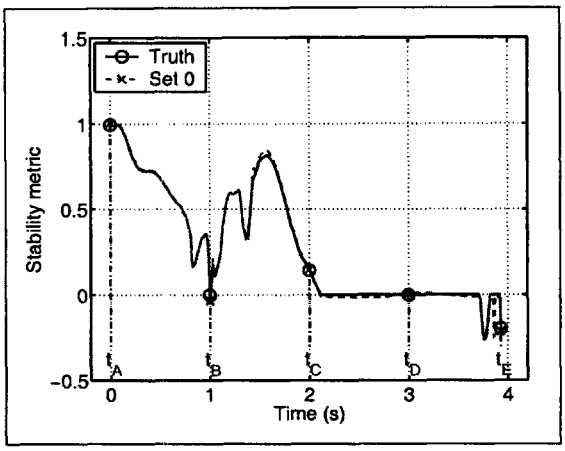

Figure 97: Maneuver 3 Set 0

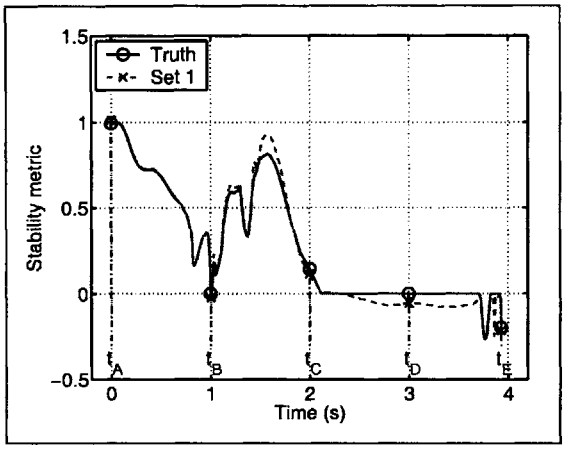

Figure 98: Maneuver 3 Set 1

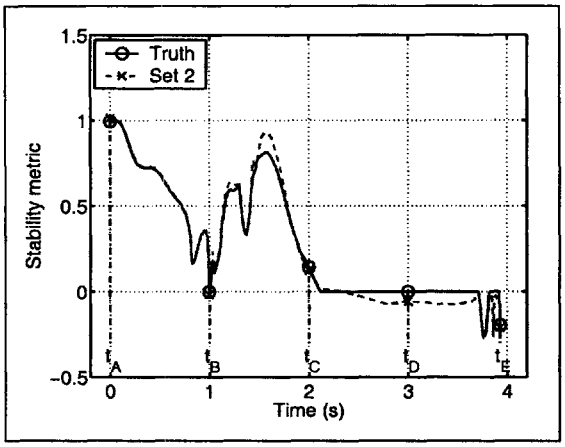

Figure 99: Maneuver 3 Set 2

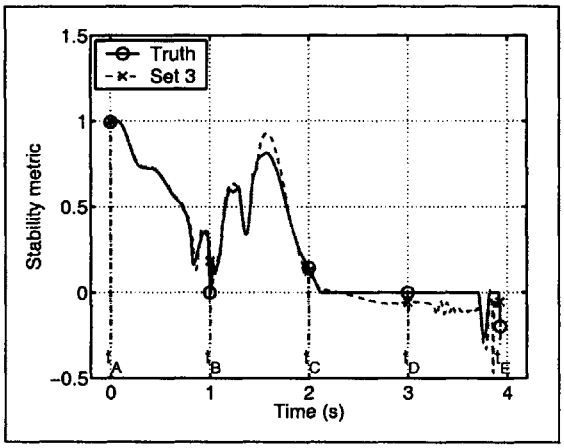

Figure 100: Maneuver 3 Set 3

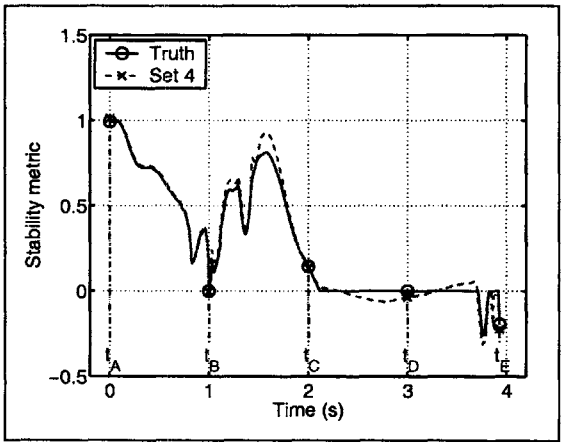

Figure 101: Maneuver 3 Set 4

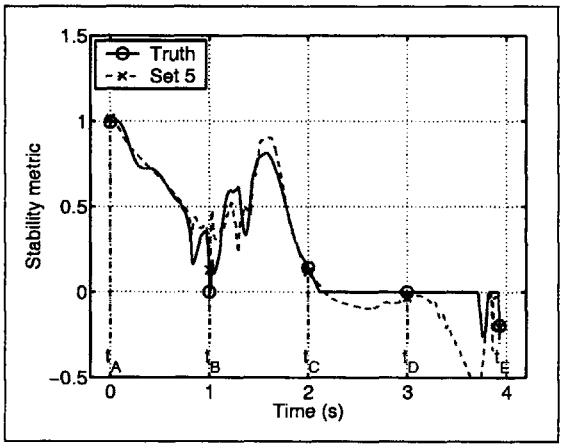

Figure 102: Maneuver 3 Set 5

Sensor set performance is quantified by root-mean-squared (RMS) error of the measured stability moment and performance in detecting wheel lift-off. Wheel lift-off detection is considered separately since it is more sensitive to error for small values of the stability moment. Performance of the wheel lift-off detector is measured by the time lag and percent accuracy in identification over the entire maneuver. The ground truth for lift-off is chosen as the times when normal forces are less than 1% of their static value. Hysteresis is used in the lift-off detector to reduce noise sensitivity, with triggering values of 0.01 and 0.10. While the detector performance is sensitive to threshold values, these are chosen to represent reasonable values; determination of optimal threshold values is outside the scope of this thesis.

Details on the performance of each sensor set during each maneuver are given in Appendix D. A summary of the results averaged over the five canonical maneuvers is given in Table 23.

Sensor Set	RMS Error	Lift-off accuracy	Lift-off detection lag
0	0.027	98.3%	-0.01 s
1	0.044	98.7%	0.01 s
2	0.045	97.0%	0.07 s
3	0.098	96.0%	0.05 s
4	0.042	97.4%	0.04 s
5	0.142	95.4%	0.13 s

Table 23: Average Performance of Sensor Sets

Sensor Set 0 has the full set of sensors, and consequently has the smallest RMS error of 0.027. Sets 1, 2, and 4 have RMS errors of approximately 0.04 and lift-off accuracies above 97%. Interestingly, Set 1 has a better accuracy percentage than Set 0

even though it has less information and a larger RMS error; Set 4 and Set 2 share this property as well. This can be attributed to the high sensitivity of the lift-off detector for values of the stability moment near the threshold. Even if the lack of sensing causes reduced average accuracy; it can have short durations of improved accuracy, which dramatically affect lift-off accuracy results. To determine the effect of sensing on wheel lift-off detection, a large number of trials should be run to fully gauge the effect of each sensor.

As mentioned above, Sets 3 and 5 are similar Set 2 with the absence of wheel acceleration in Set 3 and body angular acceleration in Set 5. These two sets have the largest RMS errors and the lowest accuracy in lift-off measurement, suggesting that they may be more important than suspension displacement or gyroscopic effects.

The effect of parameter uncertainty was also evaluated with simulation data from the canonical maneuvers. The effect of 10% uncertainty in wheel mass, body inertia, and body c.g. position for each maneuver can be seen in Appendix D. A summary of the results are given in Table 24.

Uncertain Parameter	RMS Error	Lift-off accuracy	Lift-off detection lag
None	0.027	98.3%	-0.01 s
Wheel mass	0.029	97.6%	-0.01
Body inertia	0.029	98.2%	-0.01
Body c.g.	0.052	97.1%	-0.07

Table 24: Effect of 10% Parameter Uncertainty

This uncertainty in wheel mass and body inertia have little effect on the RMS error, while the uncertainty in c.g. position nearly doubles the RMS error from 0.027 to

0.052. Uncertainty in c.g. position also causes the largest drop in lift-off detection accuracy, followed by uncertainty in wheel mass.

4.3 Conclusion

In this chapter, practical considerations were discussed for measurement of the stability moment presented in Chapter 3, including the effect of parameter and sensor uncertainty. These uncertainties were assessed analytically with a planar model and with simulation results from the canonical maneuvers. Body acceleration and body c.g. position were found to be the dominant sensor and parameter, while body angular acceleration and wheel acceleration were seen to be significant as well.

5

CHAPTER 5: CONCLUSIONS

This thesis presented an analysis of terrain factors that influence tripped rollover stability during road departure. A simple model that captures the first-order effects of slope, roughness, and deformability was presented in Chapter 2. A new instantaneous stability measure, the stability moment, that is based on the distribution of contact forces on a vehicle in arbitrary terrain was presented in Chapter 3. An uncertainty analysis of the measure was presented in Chapter 4.

Future work in tripped rollover stability management would be to integrate the stability moment into a control system and test in a variety of road departure situations. In addition, further analysis of the effective friction values of snow and organic soil matter would provide insight into the destabilizing potential of commonly encountered deformable terrains.

R

REFERENCES:

1. American Association of State Highway and Transportation Officials, *Roadside Design Guide*. Washington, D.C.: AASHTO, 1996.
2. J. Bernard, J. Shannan, M. Vanderploeg, "Vehicle rollover on smooth surfaces," *SAE Transactions*, no. 891991, 1989.
3. M. Blank, D. Margolis, "The Effect of Normal Force Variation on the Lateral Dynamics of Automobiles," *SAE Transactions*, no. 960484, 1996.
4. J. S. Cap, J. C. Wambold, "Traction Loss of a Suspended Tire on a Sinusoidal Road," *Transportation Research Record*, vol. 1000, pp 33-38, 1984.
5. C. R. Carlson, J. C. Gerdes, "Optimal Rollover Prevention with Steer by Wire and Differential Braking," *Proc. of IMECE'03*, no. IMECE2003-41825, pp. 345-354, 2003.
6. B. Chen, H. Peng, "A real-time rollover threat index for sport utility vehicles," *Proc. of American Control Conference*, pp. 1233-1237, 1999.
7. B. Chen, H. Peng, "Differential-Braking-Based Rollover Prevention for Sport Utility Vehicles with Human-in-the-loop Evaluations," *Vehicle System Dynamics*, vol. 36, no. 4-5, pp. 359-389, 2001.
8. S. R. Christoffersen, M. J. Jarzombek, J. G. Wallingford, et al., "Deceleration factors of off-road surfaces applicable for accident reconstruction," *SAE Transactions*, no. 950139, 1995.
9. N. K. Cooperrider, S. A. Hammoud, J. Colwell, "Characteristics of Soil-Tripped Rollovers," *SAE Transactions*, no. 980022, 1998.
10. DARPA Grand Challenge Web Site, www.darpa.mil/grandchallenge/
11. J. K. Davidson, G. Schweitzer, "A mechanics-based computer algorithm for displaying the margin of static stability in four-legged vehicles," *Transactions ASME Journal of Mechanical Design*, vol. 11, .pp. 487-502, 1994.

12. N. J. DeLeys, C. P. Brinkman, "Rollover Potential of Vehicles on Embankments, Sideslopes, and Other Roadside Features," *SAE Transactions*, no. 870234, 1987.
13. A. Diaz, A. Kelly, "On the dynamic stability of mobile manipulators," *Proc. of the Intl. Conf. on Field and Service Robotics,* 2003.
14. K. L. d'Entremont, "The Effects of Light-Vehicle Design Parameters in Tripped-Rollover Maneuvers – A Statistical Analysis Using an Experimentally Validated Computer Model," *SAE Transactions*, no. 950315, 1995.
15. M. A. Erdmann, "On motion planning with uncertainty," Technical Rerport 810, AI Lab, MIT, 1984.
16. G. J. Forkenbrock, W. R. Garrott, M. Heitz, B. C. O'Harra, "An experimental examination of J-Turn and Fishhook maneuvers that may induce on-road, untripped, light vehicle rollover," *SAE Transactions*, no. 2003-01-1008, 2003.
17. G. J. Forkenbrock, W. R. Garrott, M. Heitz, B. C. O'Harra, "An experimental examination of double lane change maneuvers that may induce on-road, untripped, light vehicle rollover," *SAE Transactions*, no. 2003-01-1009, 2003.
18. W. R. Garrott, G. J. Heydinger, "An investigation, via simulation, of vehicle characteristics that contribute to steering maneuver induced rollover," *SAE Transactions*, no. 920585, 1992.
19. S. Germann and R. Isermann, "Determination of the centre of gravity height of a vehicle with parameter estimation," *IFAC Symposium on System Identification*, vol. 1, pp. 563-568, 1994.
20. A. Ghasempoor, N. Sepehri, "A measure of machine stability for moving base manipulators," *Proc. of IEEE Int. Conf. on Robotics and Automation*, pp. 2249-2254, 1995.
21. Donald T. Greenwood, *Principles of Dynamics* (2nd ed.), Englewood Cliffs, NJ: Prentice Hall, 1988.
22. A. Hac, "Rollover stability index including effects of suspension design," *SAE Transactions*, no. 2002-01-0965, 2002.
23. A. Hac, T. Brown, J. Martens, "Detection of Vehicle Rollover," *SAE Transactions*, no. 2004-01-1757, 2004.

24. J. Hahn, R. Rajamani, L. Alexander, "GPS-Based Real-Time Identification of Tire-Road Friction Coefficient," *IEEE Transactions on Control Systems Technology*, vol. 10, no. 3, pp. 331-343, May 2002.

25. R. R. Hegmon, "Tire-Pavement Interaction," *SAE Transactions*, no. 870241, 1987.

26. G. J. Heydinger, R. A. Bixel, W. R. Garrott, et al., "Measured vehicle inertial parameters~NHTSA's data through November 1998," *SAE Transactions*, no. 1999-01-1336, 1999.

27. K. Iagnemma, A. Rzepniewski, S. Dubowsky, and P. Schenker, "Control of robotic vehicles with actively articulated suspensions in rough terrain," *Autonomous Robots*, vol. 14, no. 1, 2003.

28. B. Johansson, M. Gäfvert, "Untripped SUV Rollover Detection and Prevention," *Proceedings of 43rd IEEE Conference on Decision and Control*, pp. 5461-5466, Dec. 2004.

29. C. A. Klein, S. Kittivatcharapong, "Optimal Force Distribution for the Legs of a Walking Machine with Friction Cone Constraints," *IEEE Transactions on Robotics and Automation*, vol. 6, no. 1, pp. 73-85, February 1990.

30. C. Liang, R. W. Allen, T. J. Rosenthal, et al., "Tire Modeling for Off-Road Vehicle Simulation," *SAE Transactions*, no. 2004-01-2058, 2004.

31. D. A. Messuri, C. A. Klein, "Automatic body regulation for maintaining stability of a legged vehicle during rough-terrain locomotion," *IEEE J. Robotics and Automation*, vol. RA-1, .pp. 132-141, 1985.

32. R. B. McGhee, A. A. Frank, "On the stability properties of quadruped creeping gait," *Mathematical Biosciences*, vol. 3, no. 2, .pp. 331-351, 1968.

33. R. B. McGhee, G. I. Iswandhi, "Adaptive locomotion of a multilegged robot over rough terrain," *IEEE Transactions on Systems, Man, and Cybernetics*, vol. SMC-9, no. 4, .pp. 176-182 1979.

34. A. G. Nalecz, Z. Lu, K. LD'Entremont, "An investigation into dynamic measures of vehicle rollover propensity," *SAE Trans.*, no. 930831, 1993.

35. NHTSA. DOT HS 809 919. Traffic Safety Facts 2004: A Compilation of Motor Vehicle Crash Data from the Fatality Analysis Reporting System and the General Estimates System.

36. D. Odenthal, T. Bünte, J. Ackerman, "Nonlinear steering and braking control for vehicle rollover avoidance," *Proc. of European Control Conference*, 1999.

37. E. Papadopoulos, D. Rey, "The Force-Angle Measure of Tipover Stability Margin for Mobile Manipulators," *Vehicle System Dynamics*, vol. 33, no. 1, pp. 29-48, January 2000.

38. C. Parenteau, D. C. Viano, M. Shah, et al., "Field relevance of a suite of rollover tests to real-world crashes and injuries," *Accident Analysis and Prevention*, vol. 35, pp. 103-110, 2003.

39. S. C. Peters, K. Iagnemma, "An Analysis of Rollover Stability Measurement for High-Speed Mobile Robots," *Proc. of 2006 IEEE International Conference on Robotics and Automation*, pp. 3711-3716, May 2006.

40. L. R. Ray, "Nonlinear State and Tire Force Estimation for Advanced Vehicle Control," *IEEE Transactions on Control Systems Technology*, vol. 3, no. 1, pp. 117-122, March 1995.

41. RS Technologies, "Wheel Force Transducers (WFTs)", *RS Technologies Web Site*, 2006, viewed 15 June 2006, http://www.rstechltd.com/wfts.htm/.

42. J. Ryu, E. J. Rossetter, J. C. Gerdes, "Vehicle sideslip and roll parameter estimation using GPS," *Int. Symp. on Advanced Vehicle Control*, 2002.

43. M. Spenko, *Hazard Avoidance for High-Speed Rough-Terrain Unmanned Ground Vehicles*, Ph.D. Thesis, Massachusetts Institute of Technology, Cambridge MA, 2005.

44. Mark Spong, *Robot Dynamics and Control*, New York: Wiley, 1989.

45. S. V. Sreenivasan, B. H. Wilcox, "Stability and traction control of an actively actuated micro-rover," *Journal of Robotic Systems*, vol. 11, pp. 487-502, 1994.

46. D. C. Viano, C. Parenteau, "Case Study of Vehicle Maneuvers Leading to Rollovers: Need for a Vehicle Test Simulating Off-Road Excursions, Recovery and Handling," *SAE Transactions*, no. 2003-01-0169, 2003.

47. J. Viner, "Harmful Events in Crashes," *Accident Analysis and Prevention*, vol 25, no. 2, pp 139-145, 1993.

48. J. Viner, "Risk of Rollover in Ran-Off-Road Crashes," *Transportation Research Record*, vol 1500, pp 112-118, 1995.

49. J. Viner, "Rollovers on Sideslopes and Ditches," *Accident Analysis and Prevention*, vol 27, pp 483-491, 1995.

50. D. Wettergreen, C. Thrope, "Gait Generation for Legged Robots," *Proceedings IEEE/RSF International Conference on Intelligent Robots and Systems*, pp. 1413-1420, 1992.

51. R. Whitehead, W. Travis, D. M. Bevly, G. Flowers, "A Study of the Effect of Various Vehicle Properties on Rollover Propensity," *SAE Transactions*, no. 2004-01-2094, 2004.

52. J. Y. Wong, *Theory of Ground Vehicles* (3rd ed.), New York: Wiley, 2001.

A

APPENDIX A: VEHICLE MODEL PARAMETERS

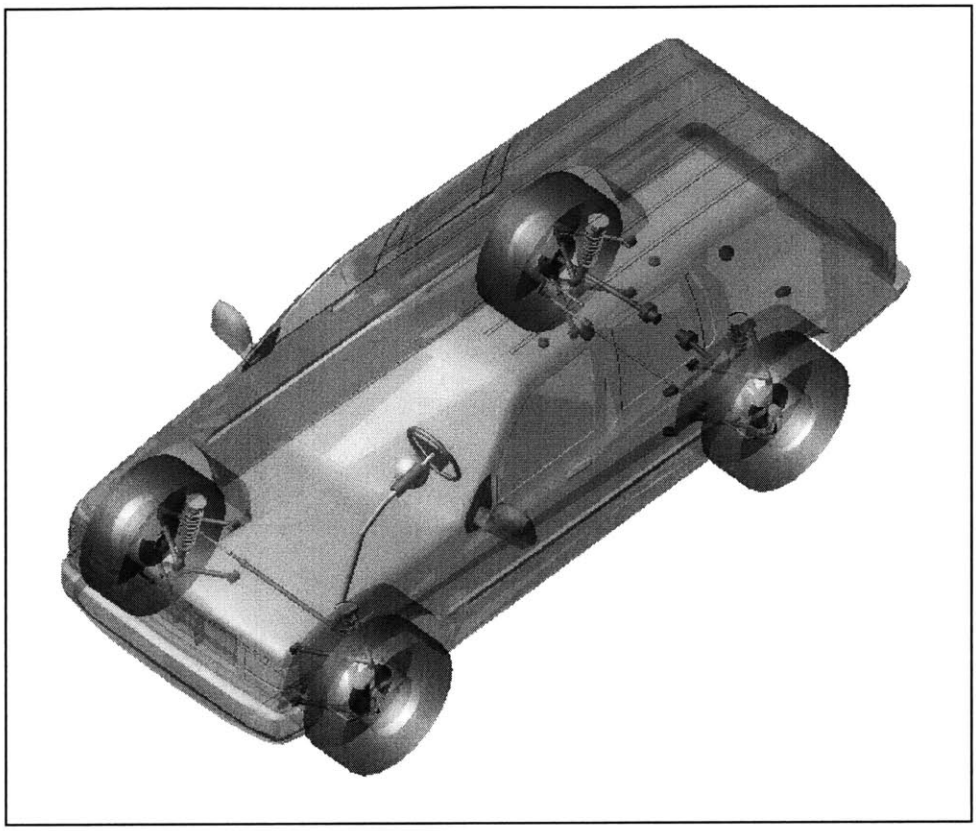

Parameters	Value
Wheelbase	2850 mm
Half Track Width	1620 mm
C.G. Distance from Front Wheels	1070 mm
C.G. Height	760 mm
SSF	1.07

Suspension Travel Full Range	200 mm
Static Tire Radius	365 mm
Tire Full Width	240 mm
Body mass	2210 kg
Unsprung mass	240 kg
Wheel mass	60 kg
Total mass	2450 kg
Body roll inertia	1240 kg m^2
Body gyroscopic inertia	0 kg m^2
Wheel gyroscopic inertia	0.2 kg m^2
Suspension spring stiffness	40 N/mm
Suspension roll stiffness	3700 N m/deg
Suspension damping	5.3 N/(mm/s)
Tire vertical stiffness	250 N/mm
Steering wheel ratio	35 deg/deg
Tire cornering stiffness	1200 N/deg (Fz = 6000 N)

B

APPENDIX B: CANONICAL MANEUVERS

Simulations of five canonical maneuvers are used throughout this thesis. A summary of each maneuver is given in Table 25. Plots of dynamic vehicle states during the maneuver are given, as well as plots of stability measures.

Maneuver	Terrain	Roughness Standard Dev.	Initial speed	Result
1	Flat	0 mm	80 km/hr	Safe
2	Flat	0 mm	100 km/hr	Tip-up
3	Road departure	0 mm	100 km/hr	Rollover
4	Road departure	6.25 mm	100 km/hr	Rollover
5	Road departure	15 mm	100 km/hr	Rollover

Table 25: Canonical Maneuver Summary

B.1 Maneuver 1

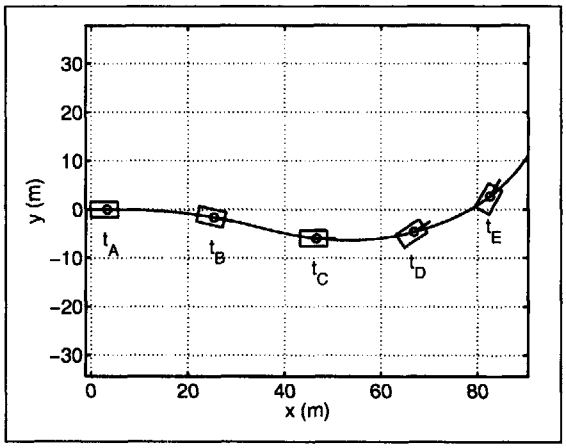

Figure 103: Maneuver 1 Trajectory

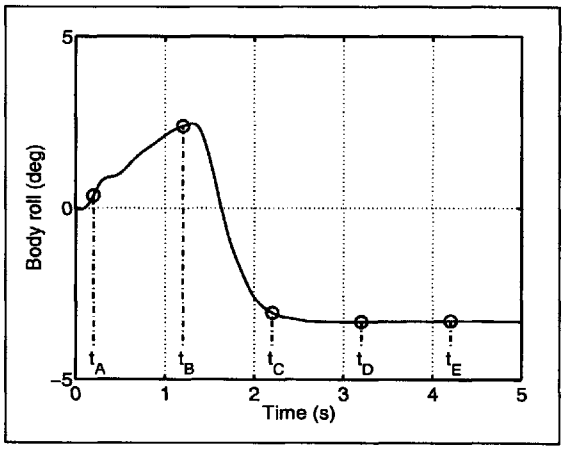

Figure 104: Maneuver 1 Body Roll

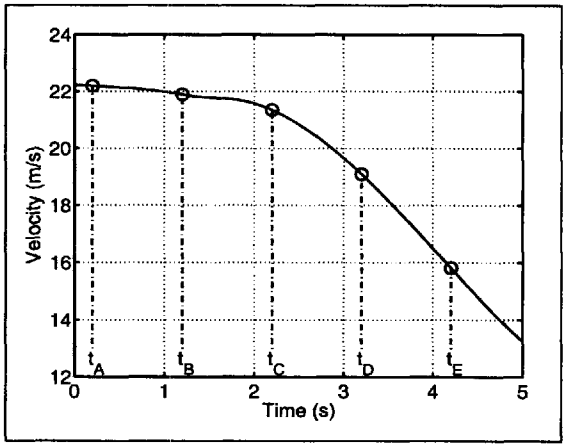

Figure 105: Maneuver 1 Velocity

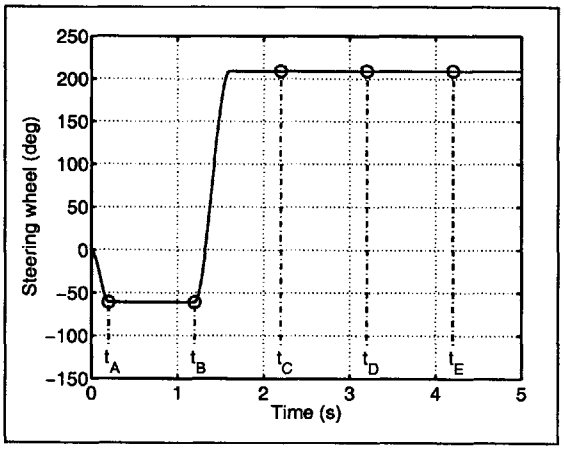

Figure 106: Maneuver 1 Steer Input

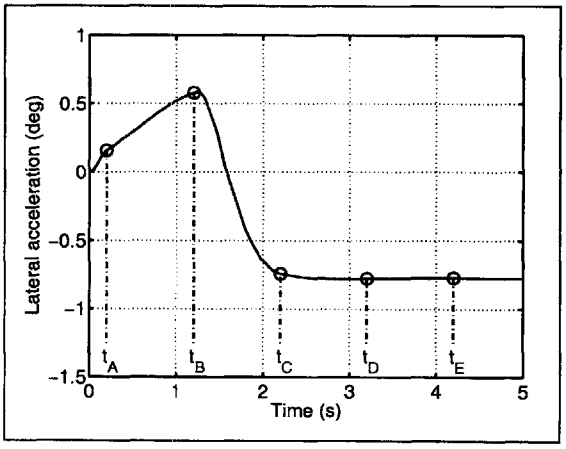

Figure 107: Maneuver 1 Lateral Acceleration

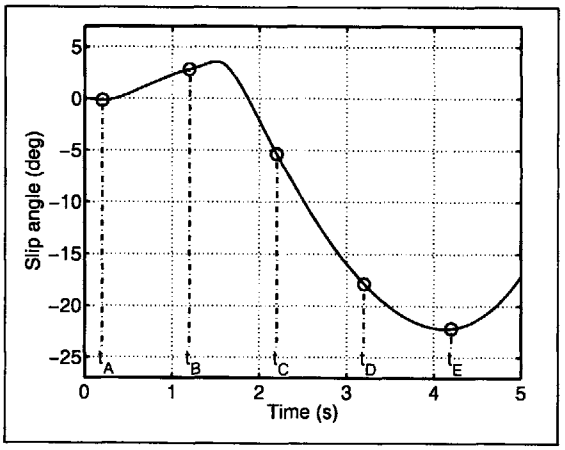

Figure 108: Maneuver 1 Slip Angle

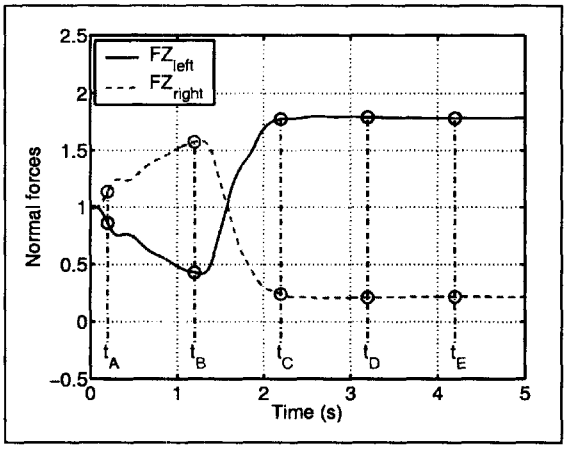

Figure 109: Maneuver 1 Left and Right Normal Forces

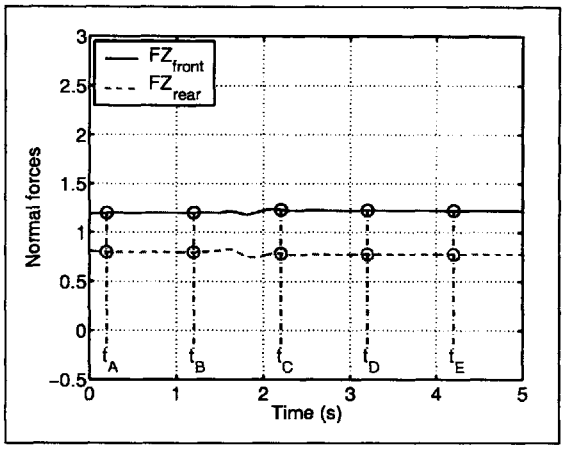

Figure 110: Maneuver 1 Front and Rear Normal Forces

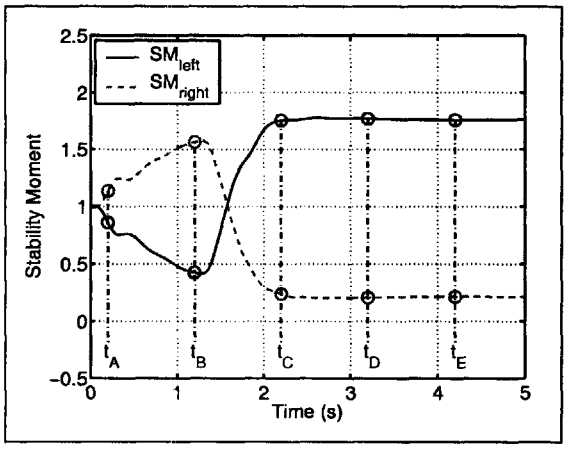

Figure 111: Maneuver 1 Left and Right Stability Moments

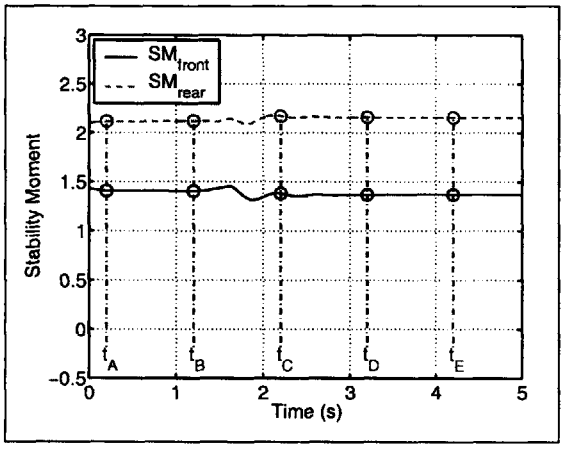

Figure 112: Maneuver 1 Front and Rear Stability Moments

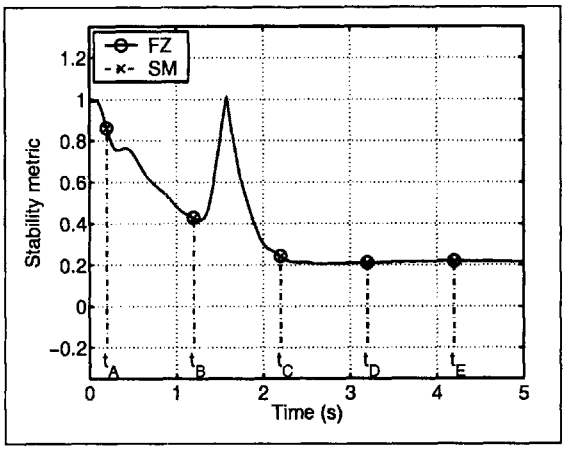

Figure 113: Maneuver 1 Stability Moment Accuracy

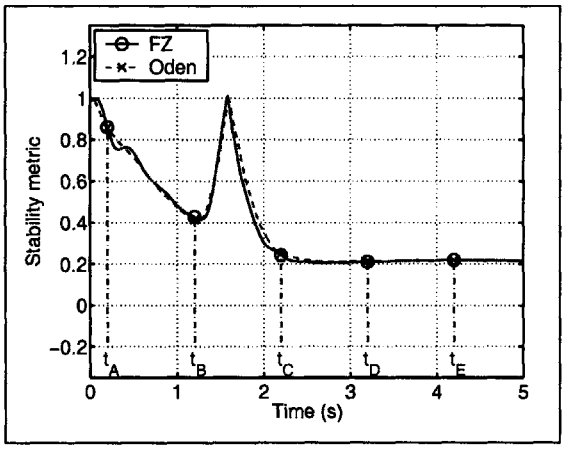

Figure 114: Maneuver 1 Odenthal Metric Accuracy

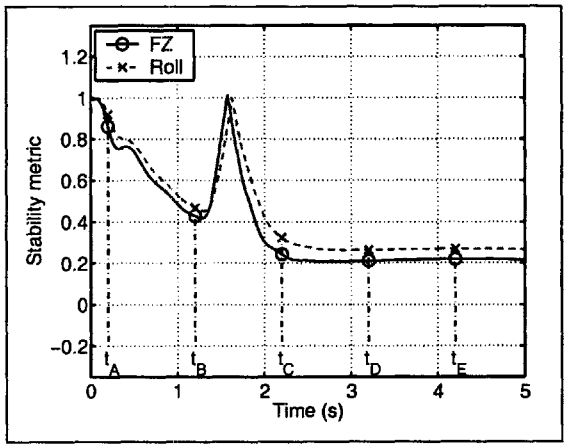

Figure 115: Maneuver 1 Critical Roll Angle Accuracy

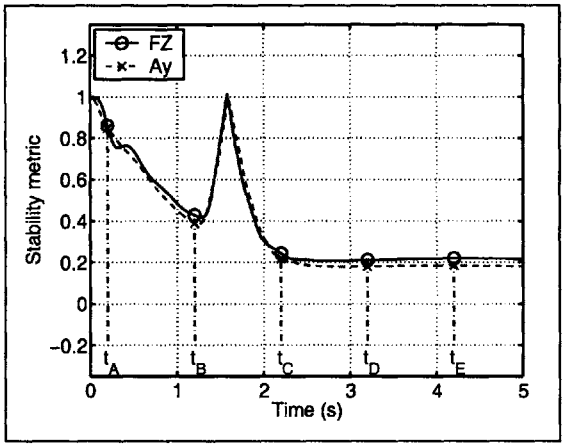

Figure 116: Maneuver 1 Critical Acceleration Accuracy

B.2 Maneuver 2

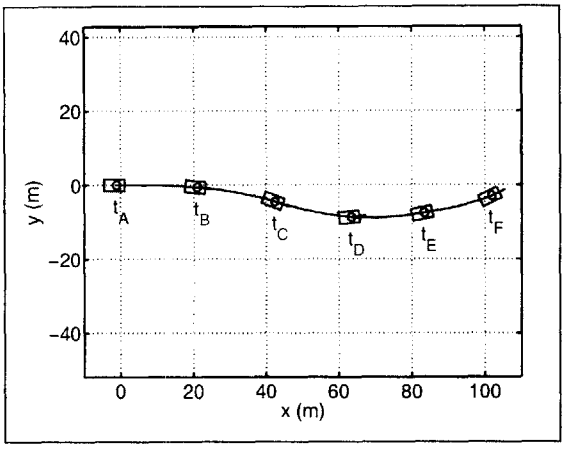

Figure 117: Maneuver 2 Trajectory

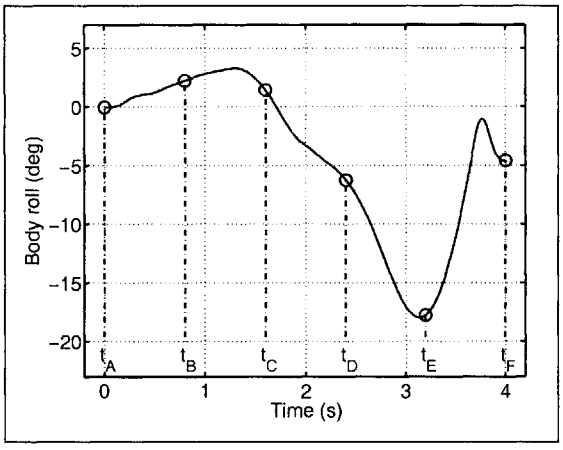

Figure 118: Maneuver 2 Body Roll

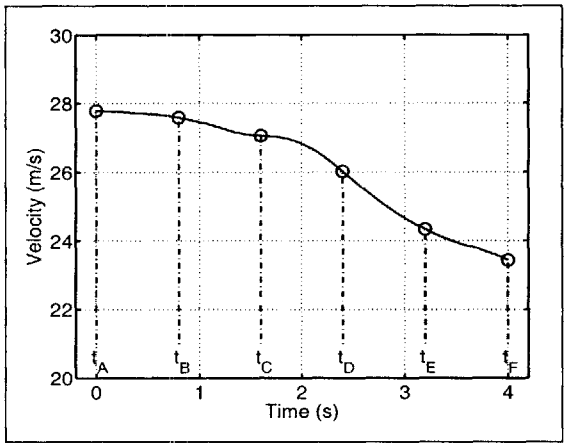

Figure 119: Maneuver 2 Velocity

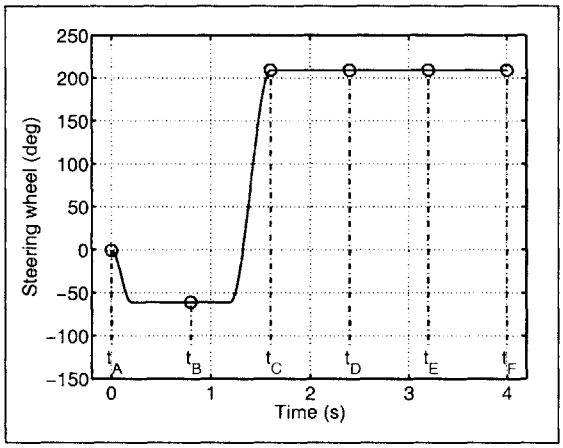

Figure 120: Maneuver 2 Steer Input

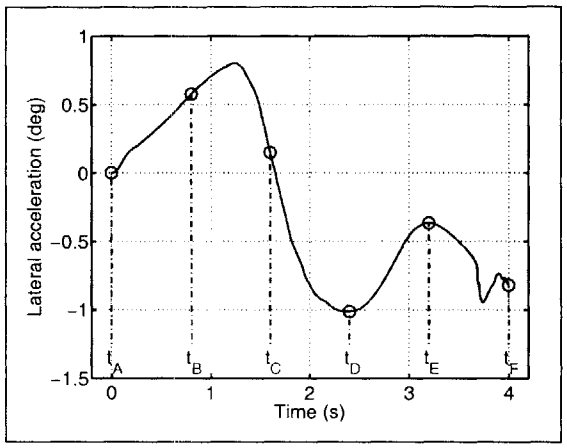

Figure 121: Maneuver 2 Lateral Acceleration

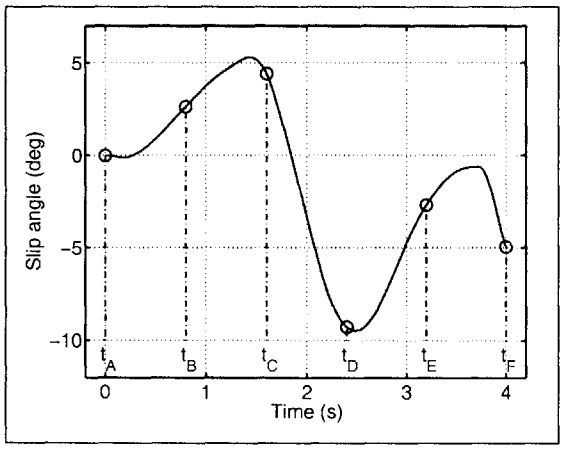

Figure 122: Maneuver 2 Slip Angle

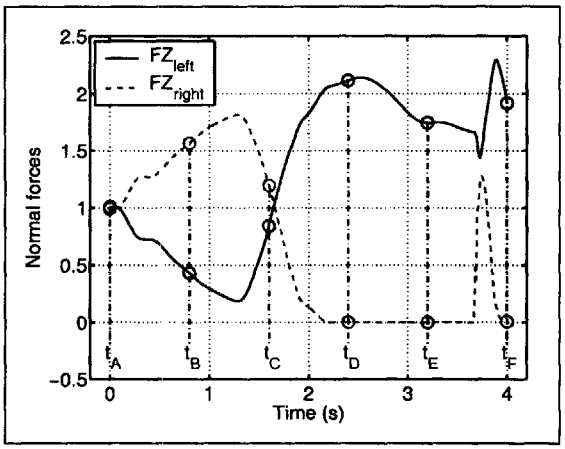

Figure 123: Maneuver 2 Left and Right Normal Forces

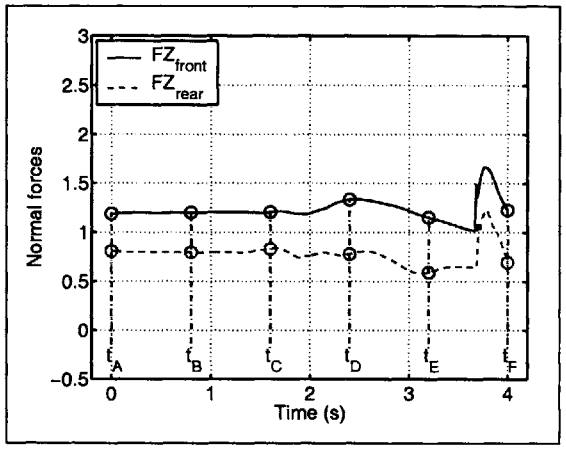

Figure 124: Maneuver 2 Front and Rear Normal Forces

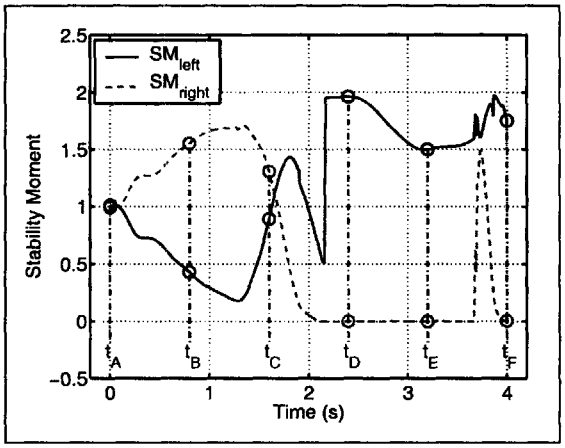

Figure 125: Maneuver 2 Left and Right Stability Moments

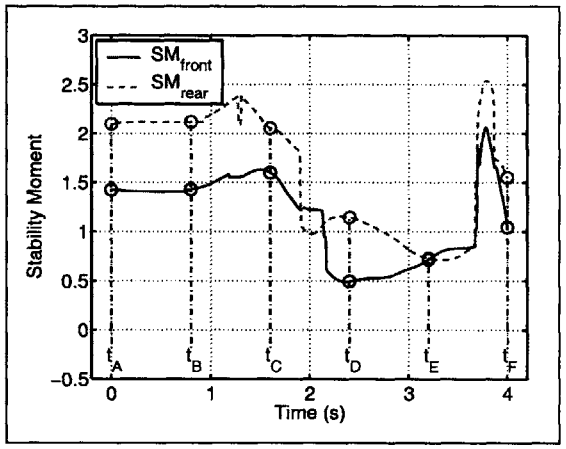

Figure 126: Maneuver 2 Front and Rear Stability Moments

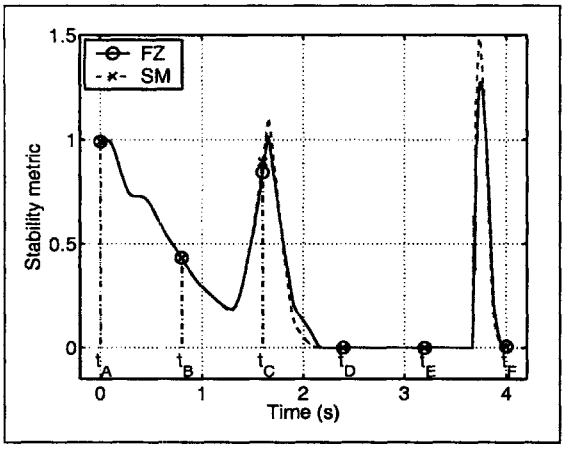

Figure 127: Maneuver 2 Stability Moment Accuracy

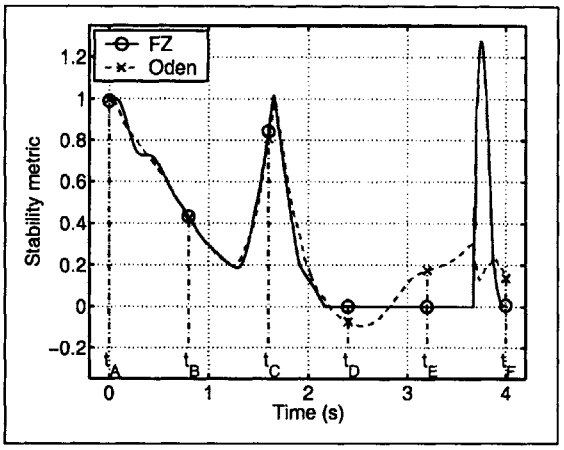

Figure 128: Maneuver 2 Odenthal Metric Accuracy

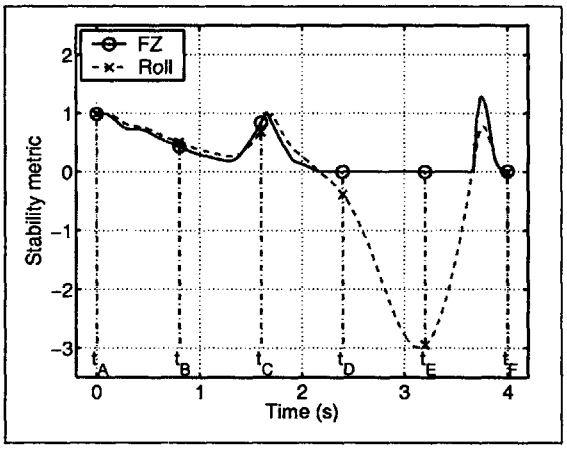

Figure 129: Maneuver 2 Critical Roll Angle Accuracy

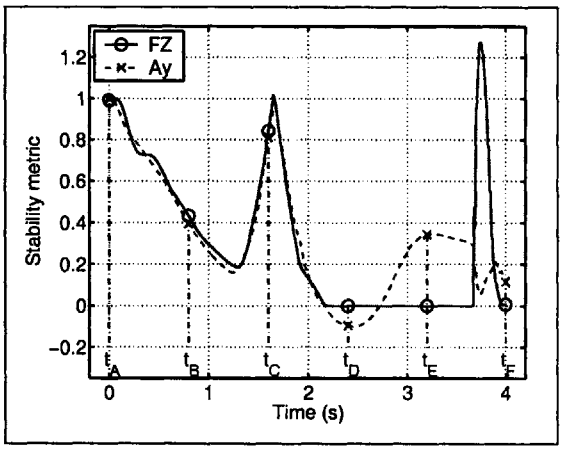

Figure 130: Maneuver 2 Critical Acceleration Accuracy

B.3 Maneuver 3

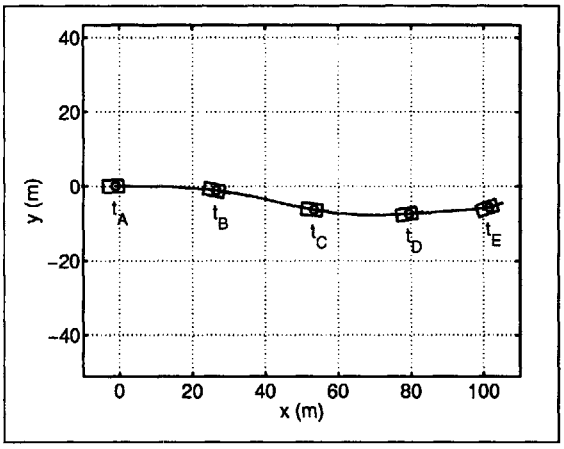

Figure 131: Maneuver 3 Trajectory

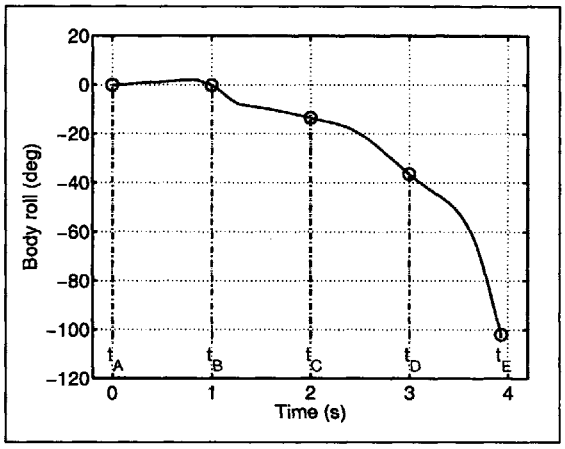

Figure 132: Maneuver 3 Body Roll

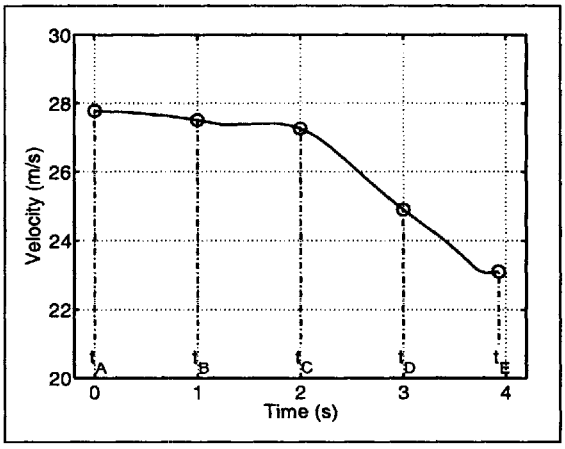

Figure 133: Maneuver 3 Velocity

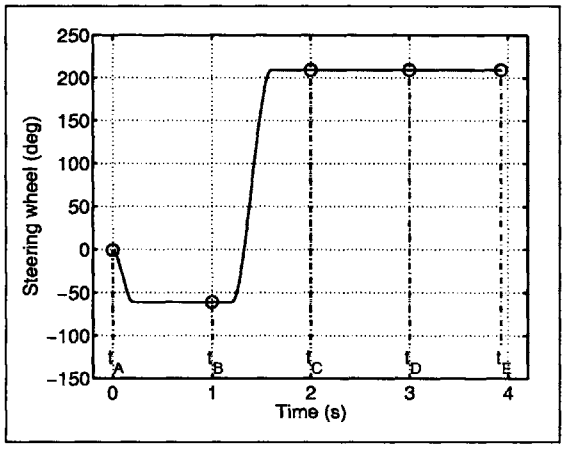

Figure 134: Maneuver 3 Steer Input

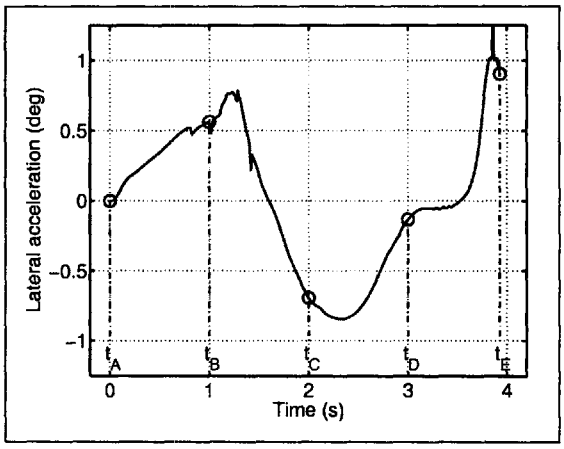

Figure 135: Maneuver 3 Lateral Acceleration

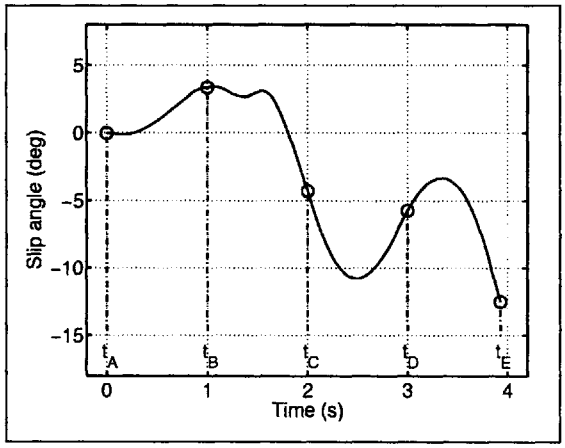

Figure 136: Maneuver 3 Slip Angle

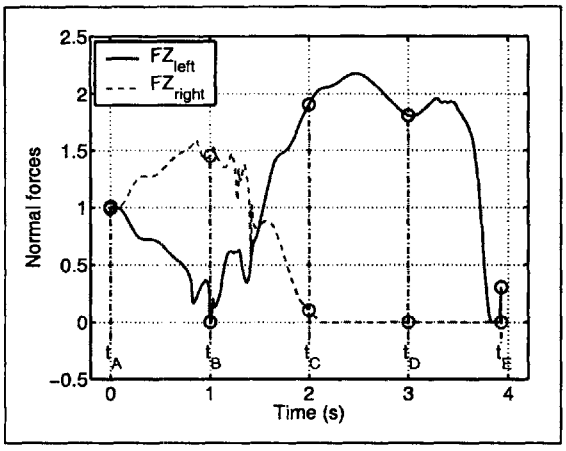

Figure 137: Maneuver 3 Left and Right Normal Forces

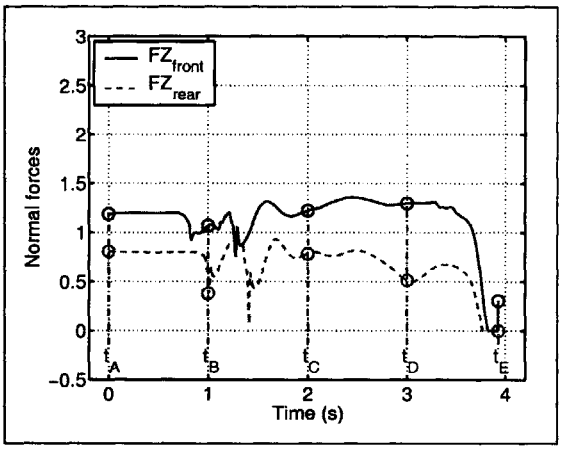

Figure 138: Maneuver 3 Front and Rear Normal Forces

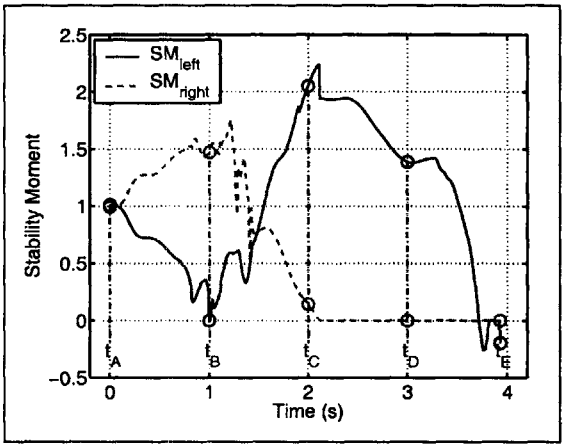

Figure 139: Maneuver 3 Left and Right Stability Moments

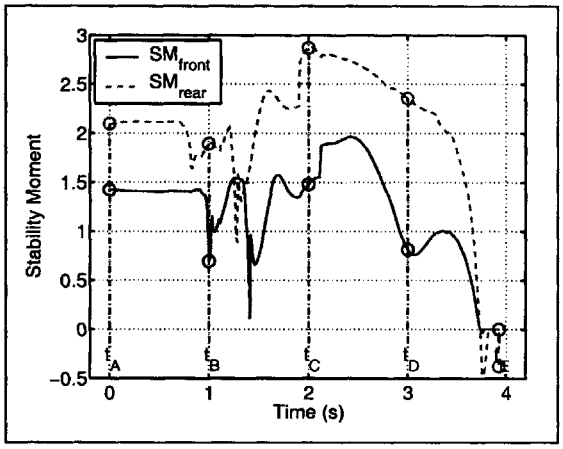

Figure 140: Maneuver 3 Front and Rear Stability Moments

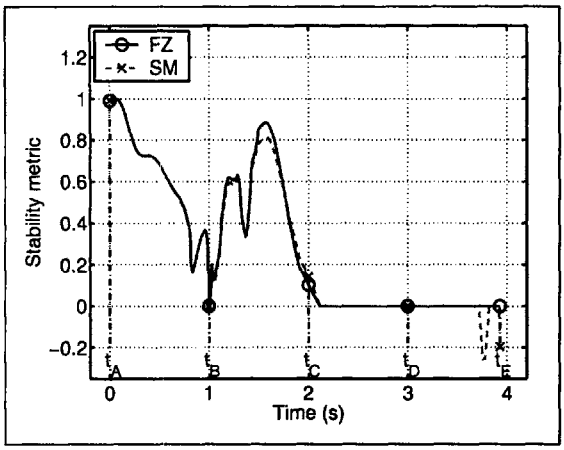

Figure 141: Maneuver 3 Stability Moment Accuracy

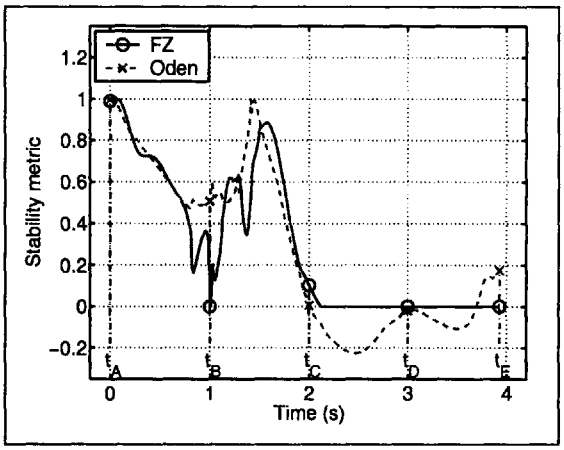

Figure 142: Maneuver 3 Odenthal Metric Accuracy

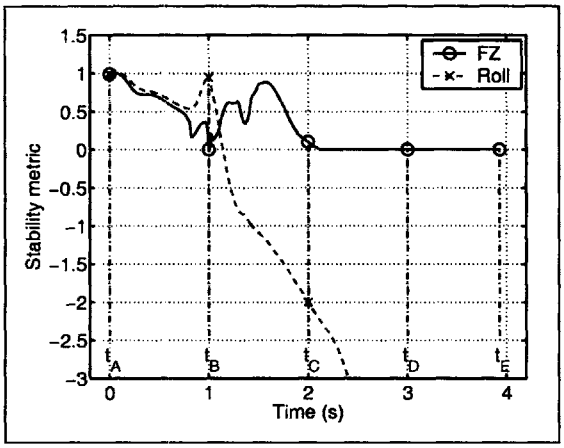

Figure 143: Maneuver 3 Critical Roll Angle Accuracy

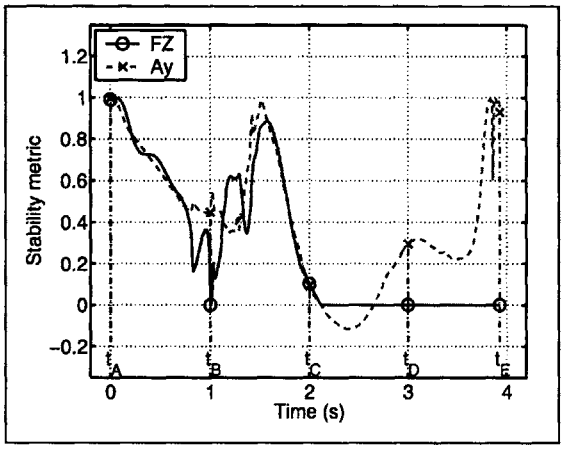

Figure 144: Maneuver 3 Critical Acceleration Accuracy

B.4 Maneuver 4

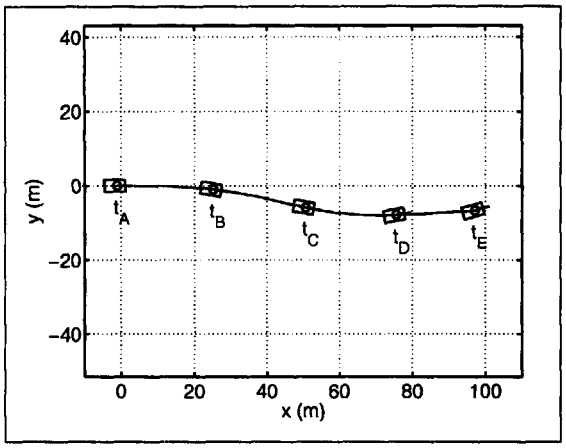

Figure 145: Maneuver 4 Trajectory

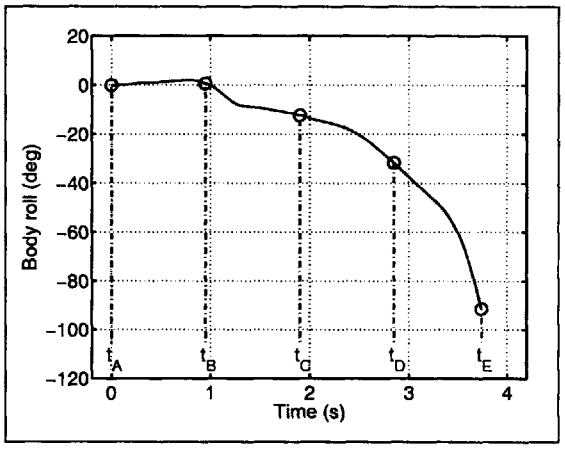

Figure 146: Maneuver 4 Body Roll

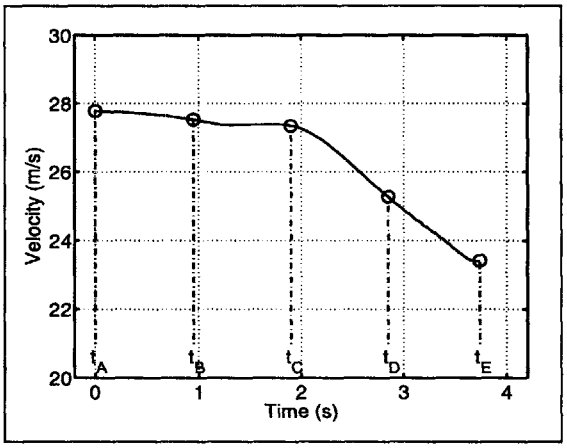

Figure 147: Maneuver 4 Velocity

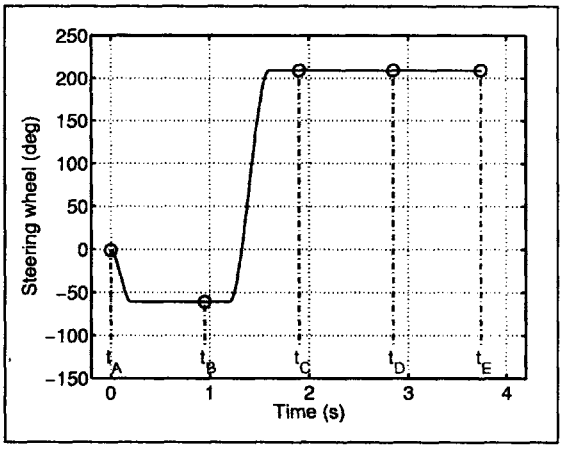

Figure 148: Maneuver 4 Steer Input

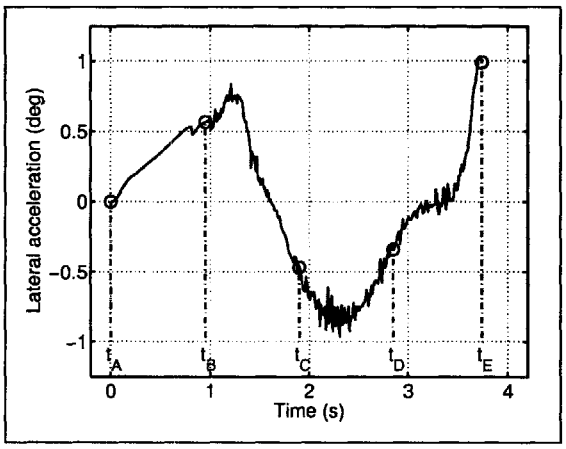

Figure 149: Maneuver 4 Lateral Acceleration

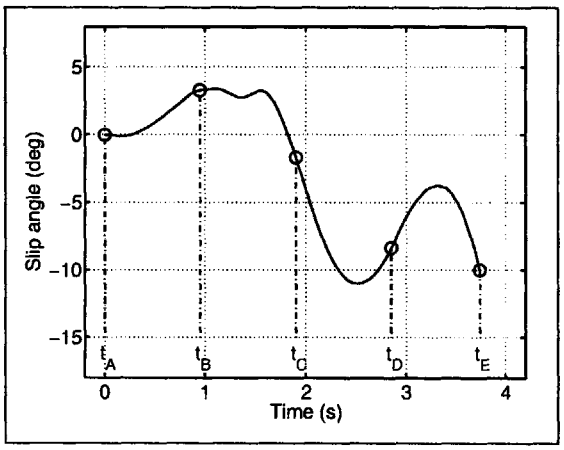

Figure 150: Maneuver 4 Slip Angle

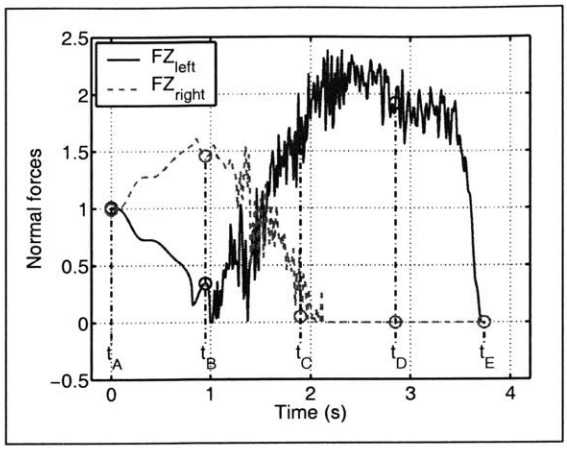

Figure 151: Maneuver 4 Left and Right Normal Forces

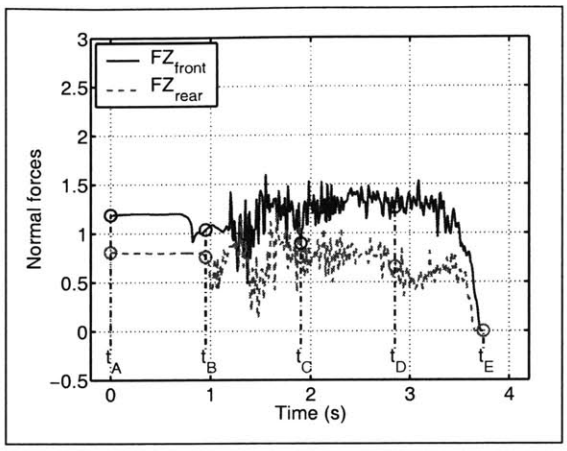

Figure 152: Maneuver 4 Front and Rear Normal Forces

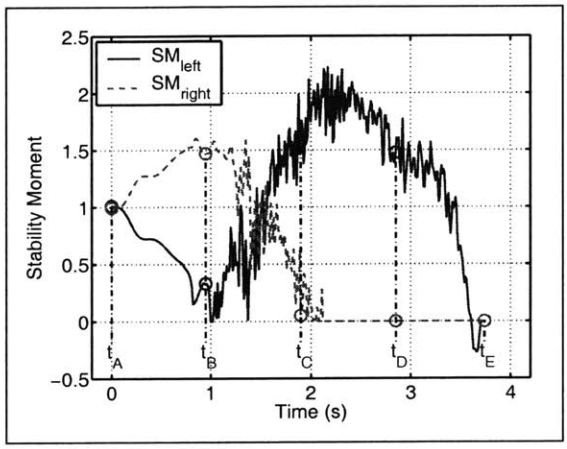

Figure 153: Maneuver 4 Left and Right Stability Moments

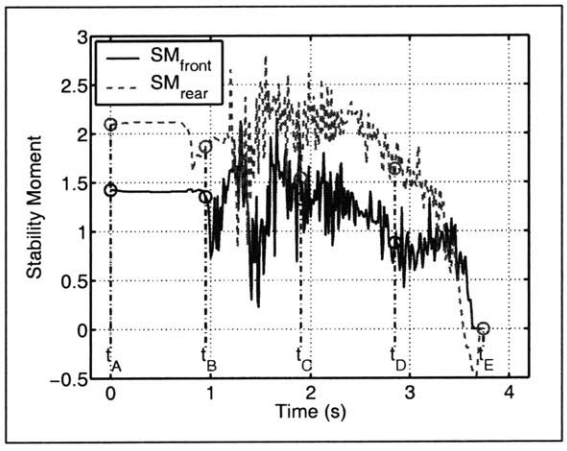

Figure 154: Maneuver 4 Front and Rear Stability Moments

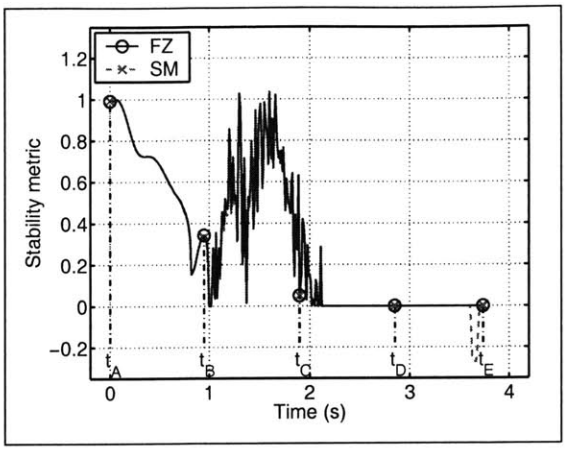

Figure 155: Maneuver 4 Stability Moment Accuracy

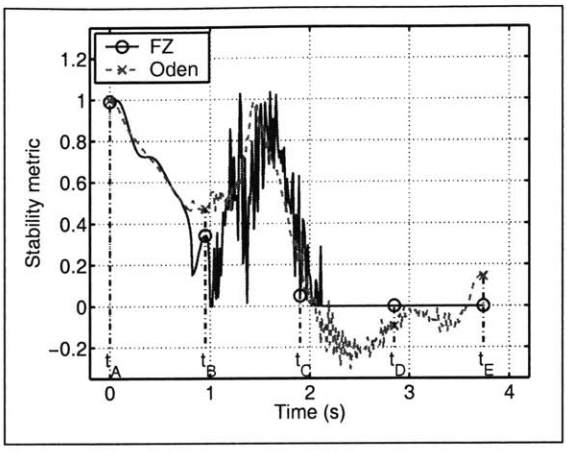

Figure 156: Maneuver 4 Odenthal Metric Accuracy

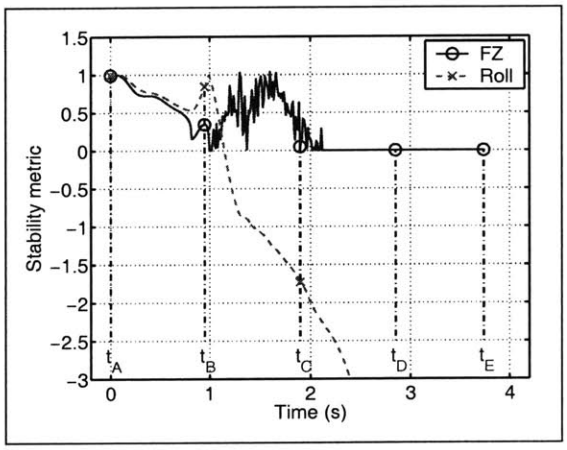

Figure 157: Maneuver 4 Critical Roll Angle Accuracy

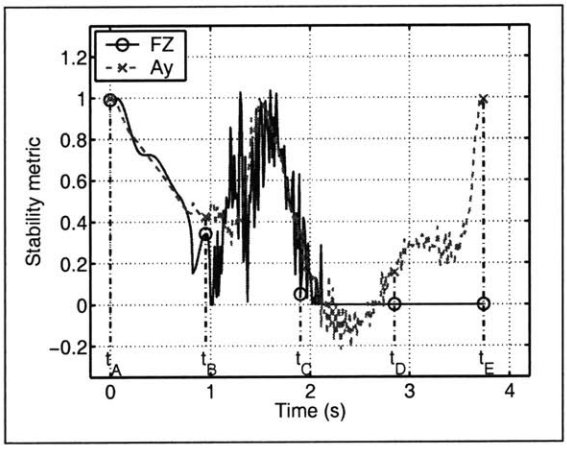

Figure 158: Maneuver 4 Critical Acceleration Accuracy

B.5 Maneuver 5

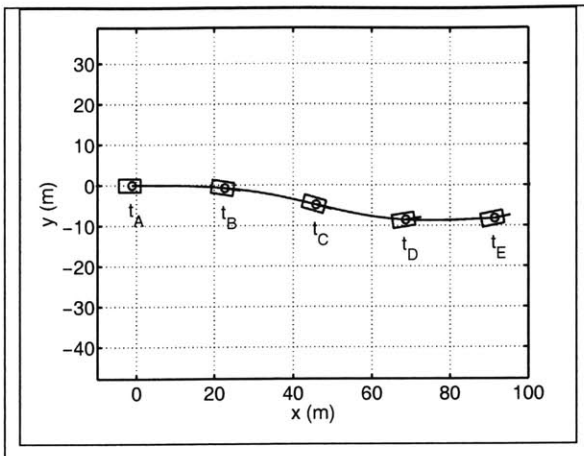

Figure 159: Maneuver 5 Trajectory

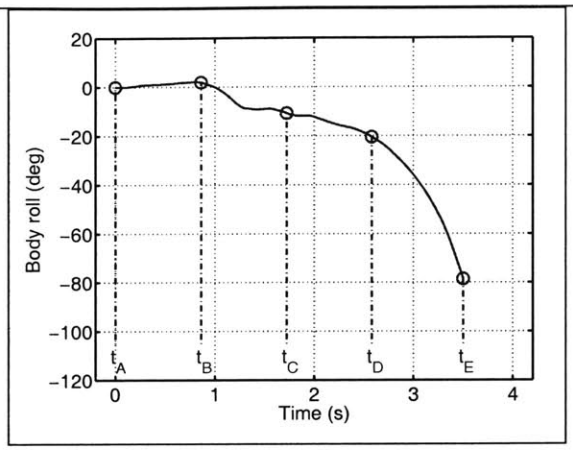

Figure 160: Maneuver 5 Body Roll

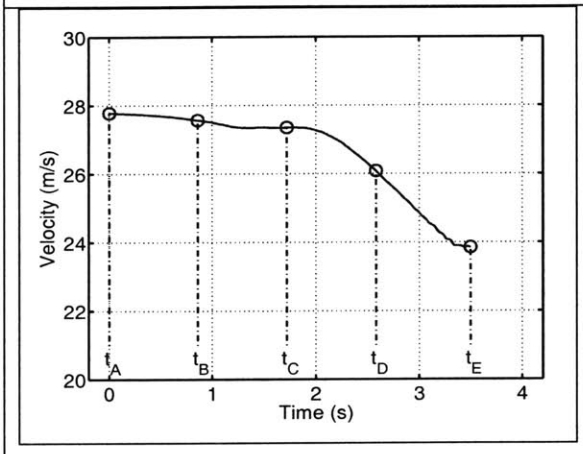

Figure 161: Maneuver 5 Velocity

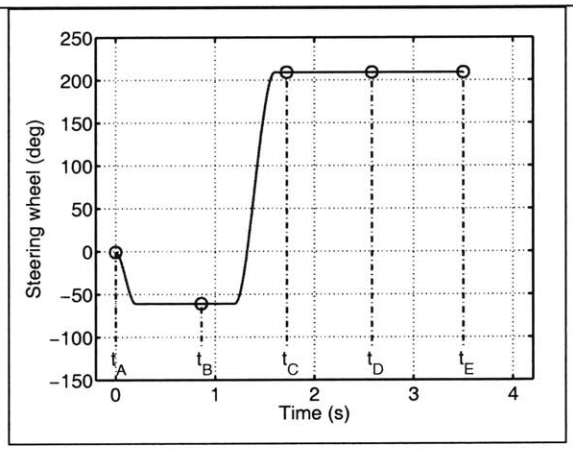

Figure 162: Maneuver 5 Steer Input

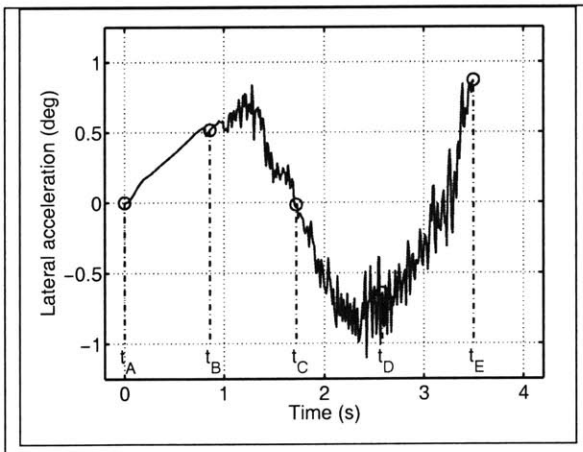

Figure 163: Maneuver 5 Lateral Acceleration

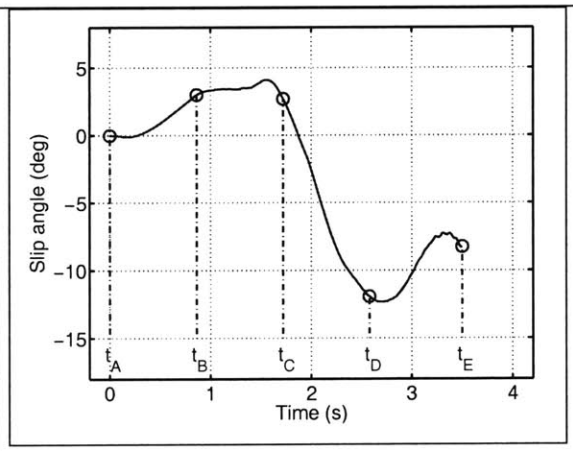

Figure 164: Maneuver 5 Slip Angle

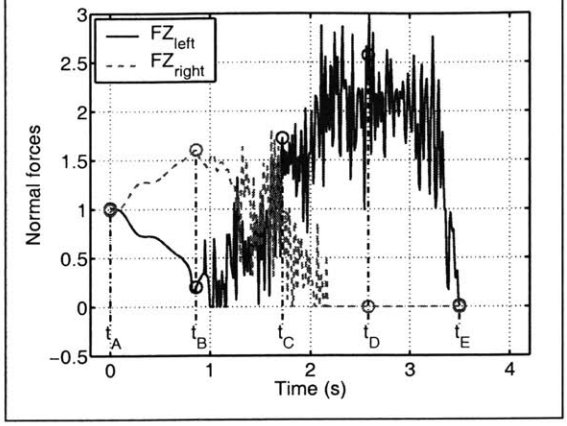

Figure 165: Maneuver 5 Left and Right Normal Forces

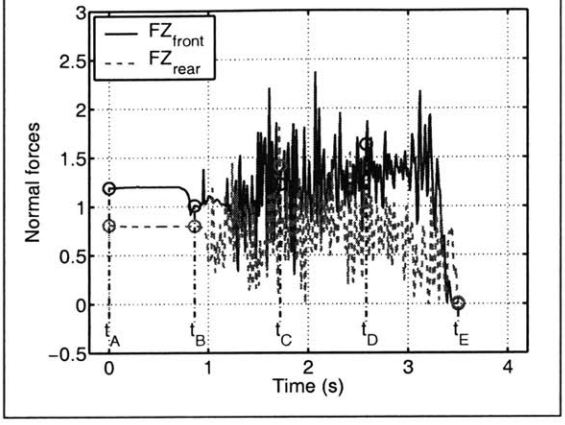

Figure 166: Maneuver 5 Front and Rear Normal Forces

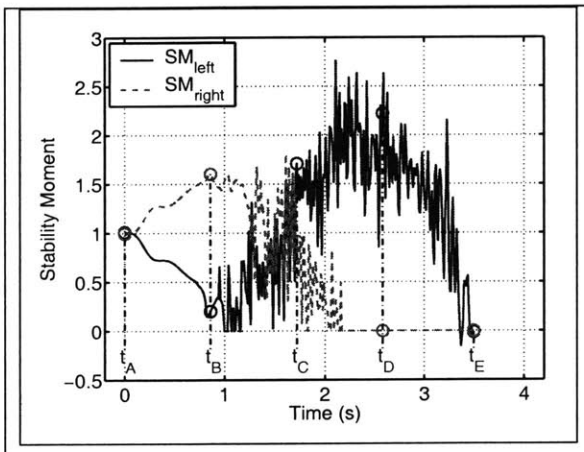

Figure 167: Maneuver 5 Left and Right Stability Moments

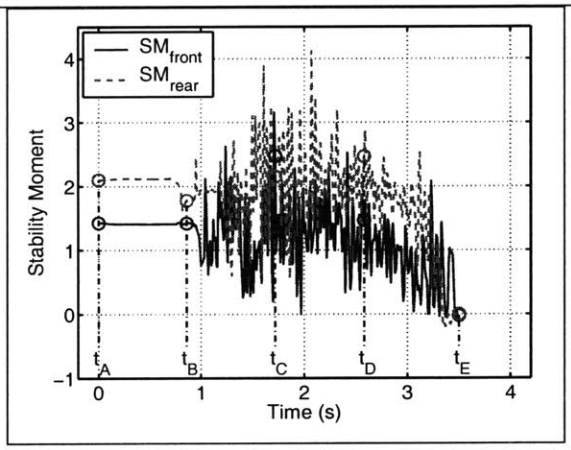

Figure 168: Maneuver 5 Front and Rear Stability Moments

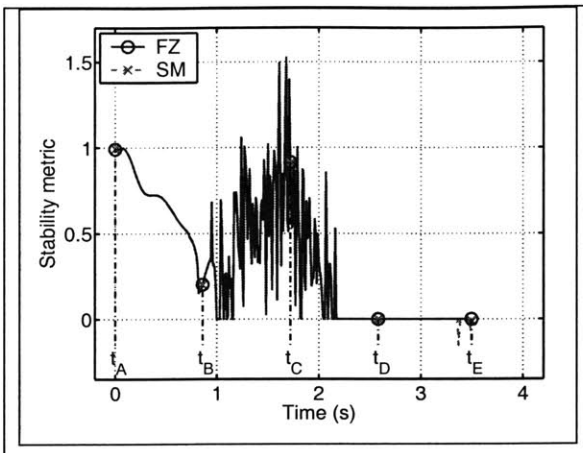

Figure 169: Maneuver 5 Stability Moment Accuracy

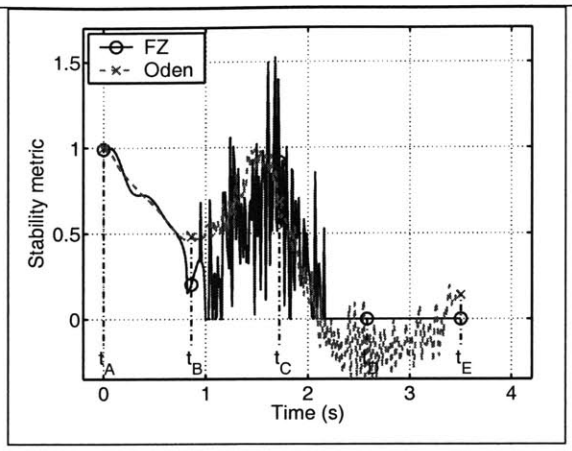

Figure 170: Maneuver 5 Odenthal Metric Accuracy

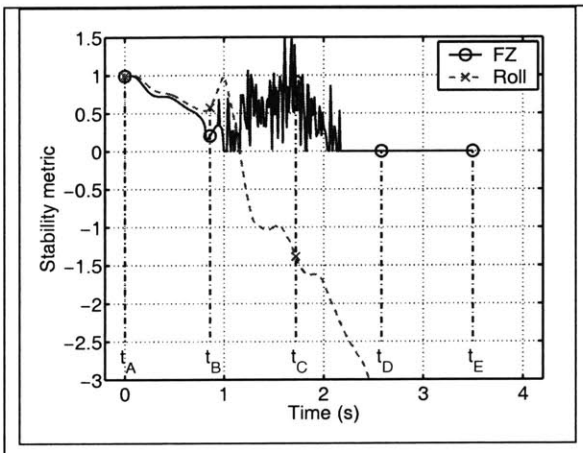

Figure 171: Maneuver 5 Critical Roll Angle Accuracy

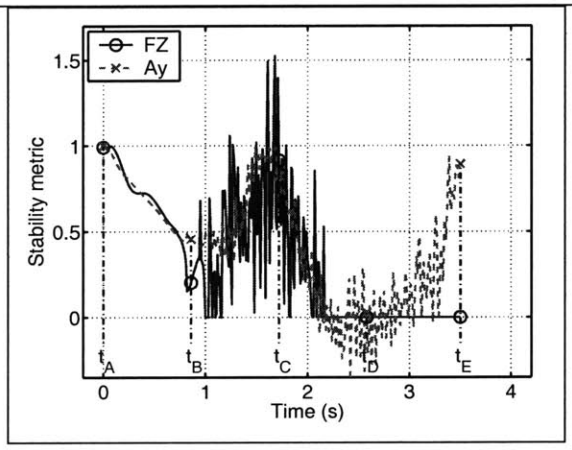

Figure 172: Maneuver 5 Critical Acceleration Accuracy

C

APPENDIX C: SENSOR BOUNDS IN SENSITIVITY ANALYSIS

p	Variable k_p	Sensitivity S_{kp}^{n}	Description
1	$I_{iz} - I_{iy}$, $i \in \{1,2\}$	$\omega_{iy}\omega_{iz}$	Wheel gyroscopic inertia
2	$I_{3z} - I_{3y}$	$\omega_{3y}\omega_{3z}$	Chassis gyroscopic inertia
3	I_{ix}, $i \in \{1,2\}$	$\dot{\omega}_{ix}$	Wheel roll inertia
4	I_{3x}	$\dot{\omega}_{3x}$	Chassis roll inertia
5	m_i, $i \in \{1,2\}$	$(s_{iy} - s_{ny} - t_{ny})a_{iz} -$ $(s_{iz} - s_{nz} - t_{nz})a_{iy}$	Wheel mass
6	m_3	$(c_{by} - s_{ny} - t_{ny})a_{3z} -$ $(c_{bz} - s_{nz} - t_{nz})a_{3y}$	Chassis mass
7	$s_{iy} - s_{ny}$	$m_i a_{iz}$	Vehicle width
8	t_{nz0}	$\sum_{i=1}^{3} m_i a_{iy}$	Tire radius
9	$c_{by} - s_{ny}$	$m_3 a_{3z}$	Lateral chassis c.g. position
10	c_{bz}	$-m_3 a_{3y}$	Vertical chassis c.g. position

Table 26: Stability Moment Parameters

s	Variable x_s	Sensitivity S_{xs}^{n}	Description
1	$\omega_{iy}\omega_{iz}$, $i \in \{1,2\}$	$I_{iz} - I_{iy}$	Wheel gyroscopic angular velocity
2	$\omega_{3y}\omega_{3z}$	$I_{3z} - I_{3y}$	Chassis gyroscopic angular velocity
3	$\dot{\omega}_{ix}$, $i \in \{1,2\}$	I_{ix}	Wheel angular acceleration
4	$\dot{\omega}_{3x}$	I_{3x}	Chassis angular acceleration
5	s_{iz}, $i = n$	$m_3 a_{3y}$	Vertical suspension displacement
6	$s_{iz} - s_{nz}$, $i \neq n$	$m_i a_{iy}$	Difference in vertical suspension displacement
7	t_{ny}, $n \in \{1,2\}$	$-\sum_{i=1}^{3} m_i a_{iz}$	Lateral tire contact
8	t_{nz}, $n \in \{1,2\}$	$\sum_{i=1}^{3} m_i a_{iy}$	Vertical tire contact
9	a_{iy}, $i \in \{1,2\}$	$-m_i(s_{iz} - s_{nz} - t_{nz})$	Lateral wheel accelerometer
10	a_{iz}, $i \in \{1,2\}$	$m_i(s_{iy} - s_{ny} - t_{ny})$	Vertical wheel accelerometer
11	a_{3y}	$-m_3(c_{bz} - s_{nz} - t_{nz})$	Lateral chassis accelerometer
12	a_{3z}	$m_3(c_{by} - s_{ny} - t_{ny})$	Vertical chassis accelerometer

Table 27: Stability Moment Sensors

p	Variable k_p	Parameter Value	First-order Sensitivity	Effect of 1% Error
1	$I_{iz} - I_{iy}$, $i \in \{1,2\}$	0.8 kg m^2	50.0	0.0021%
2	$I_{3z} - I_{3y}$	215 kg m^2	0.2	0.0018%
3	I_{ix}, $i \in \{1,2\}$	3.2 kg m^2	1.5	0.0002%
4	I_{3x}	1200 kg m^2	1.5	0.09%
5	m_i, $i \in \{1,2\}$	240 kg	11.5	0.14%
6	m_3	2210 kg	8.9	1.01%
7	$s_{iy} - s_{ny}$	1.62 m	1765.8	0.15%
8	t_{nz0}	0.365 m	19515.0	0.37%
9	$c_{by} - s_{ny}$	0.81 m	32520.2	1.72%
10	c_{bz}	0.41 m	17560.9	0.37%

Table 28: Parameter Sensitivity Flat Ground

p	Variable k_p	Parameter Value	First-order Sensitivity	Effect of 1% Error
1	$I_{iz} - I_{iy}$, $i \in \{1,2\}$	0.8 kg m^2	50	0.0021%
2	$I_{3z} - I_{3y}$	215 kg m^2	0.4	0.0044%
3	I_{ix}, $i \in \{1,2\}$	3.2 kg m^2	8	0.0013%
4	I_{3x}	1200 kg m^2	8	0.49%
5	m_i, $i \in \{1,2\}$	240 kg	16.02954	0.20%
6	m_3	2210 kg	10.57616	1.20%
7	$s_{iy} - s_{ny}$	1.62 m	2060.1	0.17%
8	t_{nz0}	0.365 m	24392.57	0.46%
9	$c_{by} - s_{ny}$	0.81 m	37940.18	2.04%
10	c_{bz}	0.41 m	21896.9	0.46%

Table 29: Parameters Sensitivity Road Departure

s	Variable x_s	Min x_s	Max x_s	Sensitivity S^n_{xs}	Effect of 1% Error
1	$\omega_{iy}\omega_{iz}$, $i \in \{1,2\}$	-50 rad^2/s^2	50 rad^2/s^2	0.8	0.0041%
2	$\omega_{3y}\omega_{3z}$	-0.16 rad^2/s^2	0.16 rad^2/s^2	215	0.0035%
3	$\dot{\omega}_{ix}$, $i \in \{1,2\}$	-1.5 rad/s^2	1.5 rad/s^2	3.2	0.0005%
4	$\dot{\omega}_{3x}$	-1.5 rad/s^2	1.5 rad/s^2	1200	0.18%
5	s_{iz}, $i = n$	-0.1 m	0.1 m	17560.88	0.18%
6	$s_{iz} - s_{nz}$, $i \neq n$	-0.2 m	0.2 m	977.076	0.02%
7	t_{ny}, $n \in \{1,2\}$	-0.03 m	0.03 m	-36051.8	0.11%
8	t_{nz}, $n \in \{1,2\}$	-0.03 m	0.03 m	19515.03	0.06%
9	a_{iy}, $i \in \{1,2\}$	-8.1423 m/s^2	8.1423 m/s^2	-31.2	0.03%
10	a_{iz}, $i \in \{1,2\}$	4.905 m/s^2	14.715 m/s^2	201.6	0.10%
11	a_{3y}	-7.9461 m/s^2	7.9461 m/s^2	-1193.4	0.97%
12	a_{3z}	4.905 m/s^2	14.715 m/s^2	1856.4	0.94%

Table 30: Sensor Sensitivity Flat Ground

s	Variable x_s	Min x_s	Max x_s	Sensitivity S_{xs}^{n}	Effect of 1% Error
1	$\omega_{iy}\omega_{iz}$, $i \in \{1,2\}$	-50 rad^2/s^2	50 rad^2/s^2	0.8	0.004%
2	$\omega_{3y}\omega_{3z}$	-0.4 rad^2/s^2	0.4 rad^2/s^2	215	0.009%
3	$\dot{\omega}_{ix}$, $i \in \{1,2\}$	-8 rad/s^2	8 rad/s^2	3.2	0.003%
4	$\dot{\omega}_{3x}$	-8 rad/s^2	8 rad/s^2	1200	0.99%
5	s_{iz}, $i = n$	-0.1 m	0.1 m	21896.9	0.22%
6	$s_{iz} - s_{nz}$, $i \neq n$	-0.2 m	0.2 m	1247.832	0.03%
7	t_{ny}, $n \in \{1,2\}$	-0.06 m	0.06 m	-42649	0.26%
8	t_{nz}, $n \in \{1,2\}$	-0.03 m	0.03 m	24392.57	0.08%
9	a_{iy}, $i \in \{1,2\}$	-10.3986 m/s^2	10.3986 m/s^2	-31.2	0.03%
10	a_{iz}, $i \in \{1,2\}$	0 m/s^2	19.62 m/s^2	208.8	0.21%
11	a_{3y}	-9.9081 m/s^2	9.9081 m/s^2	-1193.4	1.21%
12	a_{3z}	2.4525 m/s^2	17.1675 m/s^2	1922.7	1.45%

Table 31: Sensor Sensitivity Road Departure

D

APPENDIX D: UNCERTAINTY ANALYSIS RESULTS

Sensor Set	Body accel.	Body angular accel.	Susp. disp.	Wheel Accel.	Gyroscopic and wheel inertia	Tire contact
0	X	X	X	X	X	X
1	X	X	X	X	X	
2	X	X	X	X		
3	X	X	X			
4	X	X		X		
5	X		X	X		

Table 32: Sensor Set Definitions

Maneuver	Lift-off detection lag	Lift-off accuracy	RMS Error
1	0.00 s	100.0%	0.008
2	-0.06 s	97.5%	0.020
3	0.00 s	100.0%	0.018
4	0.00 s	99.2%	0.029
5	0.01 s	94.9%	0.059
Average	-0.01 s	98.3%	0.027

Table 33: Sensor Set 0 Performance

Maneuver	Lift-off detection lag	Lift-off accuracy	RMS Error
1	0.00 s	100.0%	0.016
2	0.02 s	98.8%	0.046
3	0.01 s	99.8%	0.047
4	0.00 s	98.9%	0.046
5	0.01 s	96.0%	0.065
Average	0.01 s	98.7%	0.044

Table 34: Sensor Set 1 Performance

Maneuver	Lift-off detection lag	Lift-off accuracy	RMS Error
1	0.00 s	100.0%	0.020
2	0.18 s	95.0%	0.048
3	0.15 s	96.2%	0.047
4	0.03 s	98.1%	0.046
5	0.01 s	95.7%	0.066
Average	0.07 s	97.0%	0.045

Table 35: Sensor Set 2 Performance

Maneuver	Lift-off detection lag	Lift-off accuracy	RMS Error
1	0.00 s	100.0%	0.019
2	0.13 s	95.8%	0.058
3	0.03 s	98.7%	0.061
4	0.03 s	97.3%	0.125
5	0.04 s	88.0%	0.228
Average	0.05 s	96.0%	0.098

Table 36: Sensor Set 3 Performance

Maneuver	Lift-off detection lag	Lift-off accuracy	RMS Error
1	0.00 s	100.0%	0.016
2	0.04 s	98.3%	0.048
3	0.13 s	96.7%	0.042
4	0.03 s	98.1%	0.043
5	0.01 s	94.1%	0.063
Average	0.04 s	97.4%	0.042

Table 37: Sensor Set 4 Performance

Maneuver	Lift-off detection lag	Lift-off accuracy	RMS Error
1	0.00 s	100.0%	0.028
2	0.07 s	97.3%	0.155
3	0.05 s	98.2%	0.147
4	0.05 s	94.1%	0.169
5	0.50 s	87.5%	0.211
Average	0.13 s	95.4%	0.142

Table 38: Sensor Set 5 Performance

Maneuver	Lift-off detection lag	Lift-off accuracy	RMS Error
1	0.00 s	100.0%	0.008
2	-0.06 s	97.5%	0.021
3	0.00 s	100.0%	0.018
4	0.00 s	98.9%	0.030
5	0.01 s	91.7%	0.066
Average	-0.01 s	97.6%	0.029

Table 39: 10% Wheel Mass Error

Maneuver	Lift-off detection lag	Lift-off accuracy	RMS Error
1	0.00 s	100.0%	0.008
2	-0.06 s	97.5%	0.025
3	-0.01 s	99.5%	0.022
4	0.00 s	98.9%	0.031
5	0.01 s	94.9%	0.058
Average	-0.01 s	98.2%	0.029

Table 40: 10% Body Inertia Error

Maneuver	Lift-off detection lag	Lift-off accuracy	RMS Error
1	0.00 s	100.0%	0.053
2	-0.20 s	93.8%	0.056
3	-0.04 s	98.7%	0.037
4	-0.10 s	97.6%	0.045
5	0.00 s	95.2%	0.068
Average	-0.07 s	97.1%	0.052

Table 41: 10% Body C.G. Position Error

E

APPENDIX E: MEASUREMENT OF CONTACT FORCE VARIATION

Roughness is a characteristic of off-road surfaces that was shown to have a destabilizing effect on vehicles in Chapter 2. One particular effect is to cause a variation in the wheel-terrain contact forces acting on a vehicle. Variation in contact forces has characteristics similar to a steering input on vehicle response [3], indicating that it has a significant effect on handling dynamics. Altering the handling characteristics of a vehicle can cause a driver to lose control of a vehicle, which has been observed as a significant factor in a large number of rollover accidents [49]. It is desirable to measure contact force variation, in order to inform the driver or a control system of the presence of this destabilizing effect. This Appendix presents an analysis of the performance of sensors that may be used to measure contact force variation.

Traversal of rough terrain causes variation in wheel-terrain contact forces and excites suspension dynamics. This effect is dependent on the exciting frequency of road inputs and the characteristic frequencies of the vehicle suspension. The suspension response is defined relative to temporal frequencies, while terrain is defined by spatial frequencies. The vehicle speed during traversal is the "sampling rate" that determines the temporal excitation frequency of terrain with a given spatial frequency. The relation between spatial frequency and temporal frequency for several vehicle speeds is given in Table 42.

Vehicle Speed		1 Hz	10 Hz	100 Hz	1000 Hz
1 mph	0.5 m/s	0.5 m	50 mm	5 mm	0.5 mm
10 mph	5 m/s	5 m	0.5 m	50 mm	5 mm
100 mph	50 m/s	50 m	5 m	0.5 m	50 mm

Table 42: Spatial frequencies sampled at different speeds

A linear model is used to determine the frequency response of contact force variation for a range of rough terrain excitation frequencies. The quarter car model, shown in Figure 173, has been used extensively in automotive research [3]. The model captures the vertical response of a vehicle traversing uneven terrain. The lower mass m_{us} represents a wheel, and the upper mass m_s represents 1/4 of the body. The wheel mass is commonly referred to as "unsprung mass" and the body mass as "sprung mass." The spring and damper between the two masses represent the suspension, and the spring between the wheel and the road represents tire compliance.

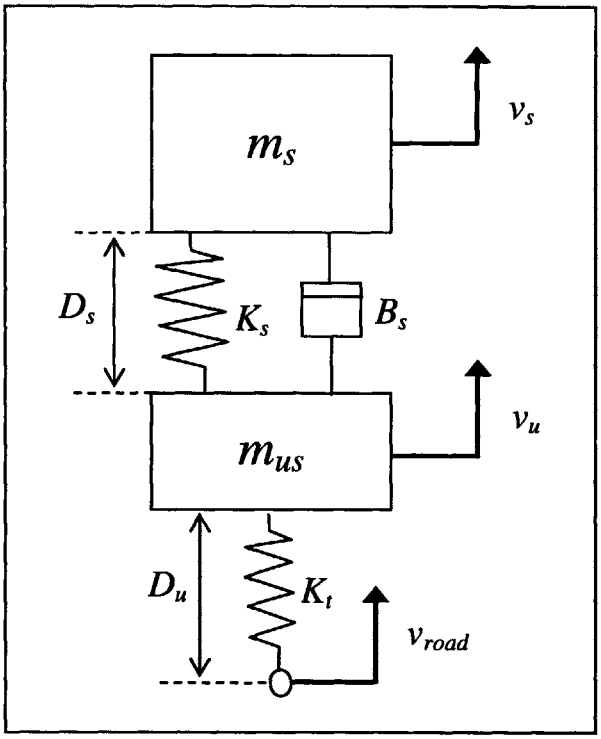

Figure 173: Quarter Car Model

The dynamics of this model are expressed with a set of linear state space equations. The general state space form is shown in (E-1), and the quarter car state space equations are shown in (E-2). The states include vertical velocity of the body v_s, vertical velocity of the wheel v_u, displacement of the suspension spring D_s, and displacement of the tire spring D_u. The road input is specified as a vertical velocity v_{road}.

$$\dot{\mathbf{x}} = \mathbf{A}\mathbf{x} + \mathbf{B}\mathbf{u} \tag{E-1}$$

$$\begin{bmatrix} \dot{v}_s \\ \dot{v}_u \\ \dot{D}_s \\ \dot{D}_u \end{bmatrix} = \begin{bmatrix} -\frac{B_s}{m_s} & \frac{B_s}{m_s} & \frac{K_s}{m_s} & 0 \\ \frac{B_s}{m_{us}} & -\frac{B_s}{m_{us}} & -\frac{K_s}{m_{us}} & \frac{K_t}{m_{us}} \\ -1 & 1 & 0 & 0 \\ 0 & -1 & 0 & 0 \end{bmatrix} \begin{bmatrix} v_s \\ v_u \\ D_s \\ D_u \end{bmatrix} + \begin{bmatrix} 0 \\ 0 \\ 0 \\ 1 \end{bmatrix} v_{road} \tag{E-2}$$

Transfer functions can be used to determine the frequency response of an output variable to an input excitation. An output variables y is specified as a linear combination

of states and inputs as in (E-3). A transfer function is defined in (E-4) for $Y(s)$, the Laplace transform of y. The frequency response of an output variable is found by substituting $s = j\omega$ into its transfer function.

$$y = \mathbf{C}\mathbf{x} + \mathbf{D}\mathbf{u} \tag{E-3}$$

$$\frac{Y(s)}{U(s)} = \mathbf{C}(s\mathbf{I} - \mathbf{A})^{-1}\mathbf{B} + \mathbf{D} \tag{E-4}$$

For this analysis, the output variable of interest is the normal contact force, which can be computed from tire deflection with (E-5). The matrices **C** and **D** for (E-5) are given as $\mathbf{C}_0$ and $\mathbf{D}_0$ in (E-6) and (E-7). A transfer function is computed in (E-8) by substituting (E-6) and (E-7) into (E-4).

$$F_z = K_t D_u \tag{E-5}$$

$$\mathbf{C}_0 = \begin{bmatrix} 0 & 0 & 0 & K_t \end{bmatrix} \tag{E-6}$$

$$\mathbf{D}_0 = [0] \tag{E-7}$$

$$\frac{F_z(s)}{V_{road}(s)} = \frac{K_t s\left(s^2 + \frac{B_s}{m_s}\frac{m_s + m_{us}}{m_{us}}s + \frac{K_s}{m_s}\frac{m_s + m_{us}}{m_{us}}\right)}{s^4 + \frac{B_s}{m_s}\frac{m_s + m_{us}}{m_{us}}s^3 + \left(\frac{K_s}{m_s}\frac{m_s + m_{us}}{m_{us}} + \frac{K_t}{m_{us}}\right)s^2 + \frac{B_s K_t}{m_s m_{us}}s + \frac{K_s K_t}{m_s m_{us}}} \tag{E-8}$$

An alternative form of the transfer function can be found by changing the road input from a velocity to a position, by (E-9). The transfer function $\mathbf{G}_0$ is then defined in (E-10) and given fully in (E-11). The magnitude frequency response $|G_0(j\omega)|$ is plotted in Figure 174 for a vehicle traversing a sinusoidal road with 10 mm amplitude, 20 mm peak-to-peak, and using parameters of the test vehicle described in Table 43. The

horizontal axis of Figure 174 indicates the temporal frequency of the road forcing input, and the vertical axis indicates the contact force variation, expressed as a percentage of the static wheel load $F_0 = (m_s + m_{us})g$.

$$Z_{road}(s) = \frac{1}{s} V_{road}(s) \tag{E-9}$$

$$G_0(s) = \frac{F_z(s)}{Z_{road}(s)} \tag{E-10}$$

$$G_0(s) = \frac{K_t s^2 \left(s^2 + \frac{B_s}{m_s} \frac{m_s + m_{us}}{m_{us}} s + \frac{K_s}{m_s} \frac{m_s + m_{us}}{m_{us}} \right)}{s^4 + \frac{B_s}{m_s} \frac{m_s + m_{us}}{m_{us}} s^3 + \left(\frac{K_s}{m_s} \frac{m_s + m_{us}}{m_{us}} + \frac{K_t}{m_{us}} \right) s^2 + \frac{B_s K_t}{m_s m_{us}} s + \frac{K_s K_t}{m_s m_{us}}} \tag{E-11}$$

Ks	22.3 N/mm
Kt	243 N/mm
Ms	413 kg
Mus	27 kg
Bs	303 N s/m

Table 43: Quarter car vehicle parameters

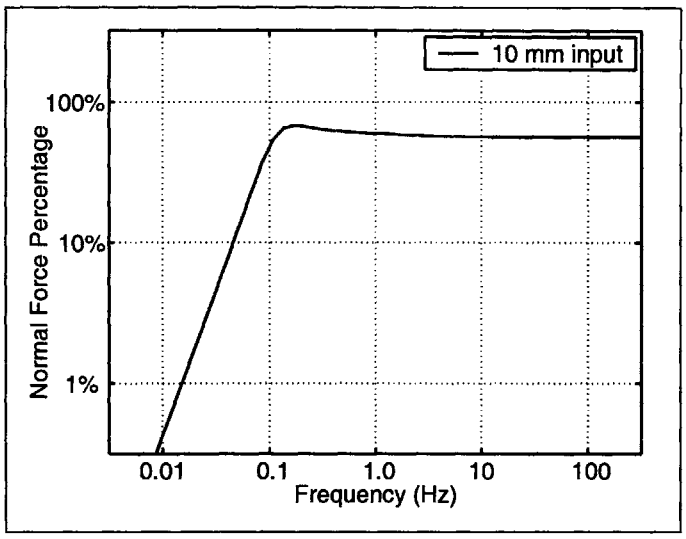

Figure 174: Bode plot of $G_0(s)$

In addition to (E-5), two expressions can be written for the normal contact force. The first, given in (E-12), is computed with the sum of forces acting on the unsprung mass. The second, given in (E-13), is computed from the sum of sprung and unsprung mass accelerations, since the contact force is the only external force acting on that system. It should be noted that (E-13) is also used in the contact force stability measure of Chapter 3.

$$F_z = K_s D_s + B_s(v_u - v_s) - m_{us}\dot{v}_u \tag{E-12}$$

$$F_z = m_s\dot{v}_s + m_{us}\dot{v}_u \tag{E-13}$$

Equation (E-12) requires measurement of suspension spring displacement, suspension damper velocity, and wheel acceleration. As discussed in Chapter 1, sensors for suspension displacement and acceleration are readily available. Suspension damper velocity may be computed from the numerical derivative of suspension displacement, though this increases sensitivity to high-frequency sensor noise. Additionally, automotive shock absorbers generate forces as a nonlinear function of suspension

velocity, increasing the calibration requirements. As such, normal contact force is partially measurable with (E-12).

Equation (E-13) requires measurement of wheel acceleration and body acceleration, which were deemed practical to measure in Chapter 1. In a multi-wheeled vehicle, however, the body acceleration includes components of the normal force variation from all wheels, which this quarter car model is unable to resolve. As such, normal contact force is unmeasurable with (E-13).

Of the three expressions for normal force, (E-5) and (E-13) are unmeasurable, while (E-12) is partially measurable with suspension displacement and wheel acceleration sensors. The component of normal force variation measured by suspension displacement is defined as F_1 in (E-14). The component measured by wheel acceleration is defined as F_2 in (E-15). Transfer functions that indicate the normal force measured by the components F_1 and F_2 are defined as G_1 and G_2 in (E-16) and (E-17). The full form of (E-16) and (E-17) is given in (E-18) and (E-19).

$$F_1 = K_s D_s \tag{E-14}$$

$$F_2 = -m_u \dot{v}_u \tag{E-15}$$

$$G_1(s) = \frac{F_1(s)}{Z_{road}(s)} \tag{E-16}$$

$$G_2(s) = \frac{F_2(s)}{Z_{road}(s)} \tag{E-17}$$

$$G_1(s) = \frac{K_t \cdot \frac{K_s}{m_{us}} s^2}{s^4 + \frac{B_s}{m_s}\frac{m_s + m_{us}}{m_{us}} s^3 + \left(\frac{K_s}{m_s}\frac{m_s + m_{us}}{m_{us}} + \frac{K_t}{m_{us}}\right) s^2 + \frac{B_s K_t}{m_s m_{us}} s + \frac{K_s K_t}{m_s m_{us}}} \quad \text{(E-18)}$$

$$G_2(s) = \frac{K_t \cdot s^2 \left(s^2 + \frac{B_s}{m_s} s + \frac{K_s}{m_s}\right)}{s^4 + \frac{B_s}{m_s}\frac{m_s + m_{us}}{m_{us}} s^3 + \left(\frac{K_s}{m_s}\frac{m_s + m_{us}}{m_{us}} + \frac{K_t}{m_{us}}\right) s^2 + \frac{B_s K_t}{m_s m_{us}} s + \frac{K_s K_t}{m_s m_{us}}} \quad \text{(E-19)}$$

Performance transfer functions H_1 and H_2 are defined in (E-20) and (E-21) as the ratio of sensor transfer functions G_1 and G_2 to the total normal force transfer function G_0. H_1 and H_2 are expressed fully in (E-22) and (E-23). The amplitudes of H_1 and H_2 at a given frequency, $|H_1(j\omega)|$ and $|H_2(j\omega)|$, are plotted in Figure 175. These magnitudes represent the fraction of the true normal force measured by each sensor at a given frequency. The parameters used in this plot are based the test vehicle shown below and are given above in Table 43. It should be noted, however, that no vehicle data was available for the suspension damper, so a damping ratio of 0.75 was assumed.

$$H_1(s) = \frac{G_1(s)}{G_0(s)} \quad \text{(E-20)}$$

$$H_2(s) = \frac{G_2(s)}{G_0(s)} \quad \text{(E-21)}$$

$$H_1(s) = \frac{\frac{K_s}{m_{us}}}{s^2 + \frac{B_s}{m_s}\frac{m_s + m_{us}}{m_{us}} s + \frac{K_s}{m_s}\frac{m_s + m_{us}}{m_{us}}} \quad \text{(E-22)}$$

$$H_2(s) = \frac{s^2 + \frac{B_s}{m_s}s + \frac{K_s}{m_s}}{s^2 + \frac{B_s}{m_s}\frac{m_s + m_{us}}{m_{us}}s + \frac{K_s}{m_s}\frac{m_s + m_{us}}{m_{us}}} \qquad \text{(E-23)}$$

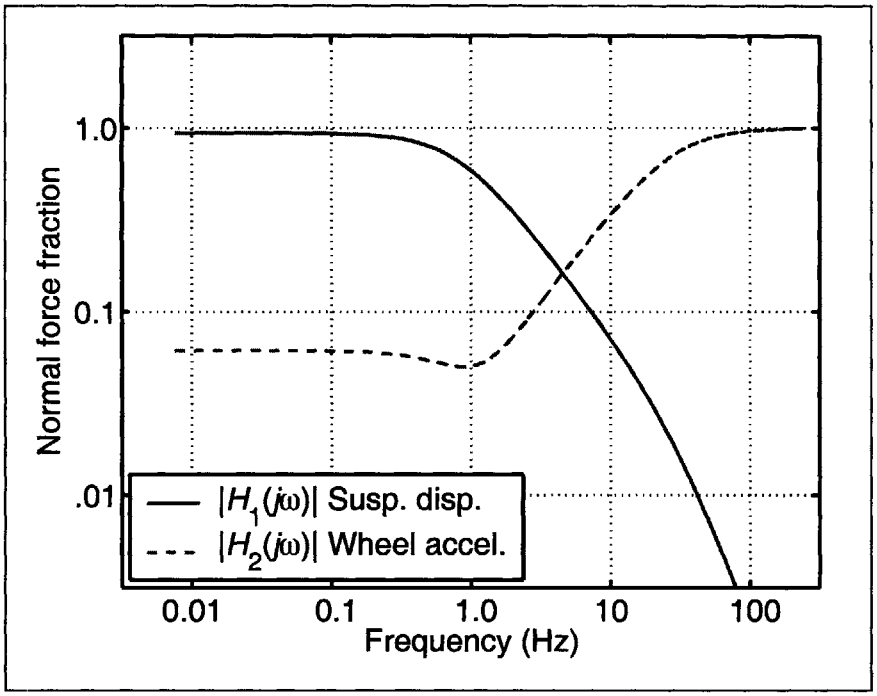

Figure 175: Sensor Performance Predicted by Quarter Car Model

This plot indicate that suspension displacement may be used to estimate normal force at low frequencies and that wheel acceleration may be used to measure normal force variation at high frequencies.

To verify this conclusion, experiments were conducted with a test vehicle traveling over surfaces of varying roughness. Vehicle sensors included suspension displacement, wheel acceleration, and a high-fidelity Wheel Force Transducer (WFT) to measure normal forces. A view of the accelerometer mounted on the suspension knuckle and a typical WFT [41] are shown in Figure 176.

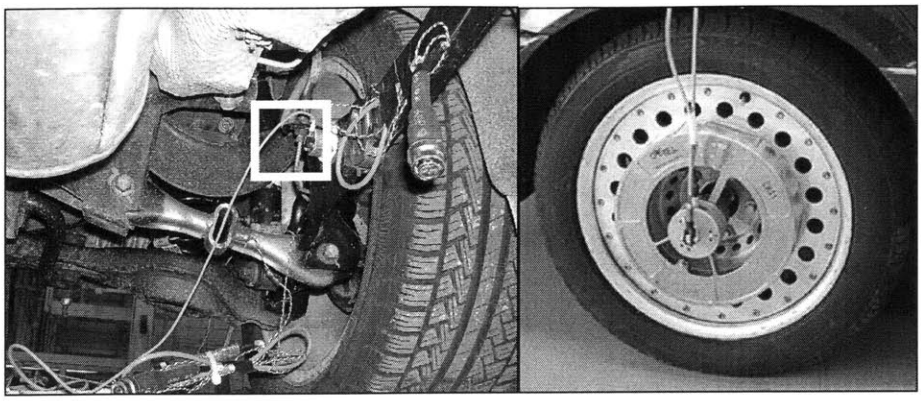

Figure 176: Rear left accelerometer and typical WFT [41]

The following plots show the experimental measurement of the performance transfer function amplitudes during traversal of a gravel road course. The spectral amplitudes were computed from the square root of Welch power spectral density in Matlab using the default window parameters of 8 window sections with 50% overlap. The sensors were sampled at 500 Hz, and the length of the dataset was just under 8 minutes. Suspension displacement performance $|H_1(j\omega)|$ is given in Figure 177 and wheel acceleration performance $|H_2(j\omega)|$ in Figure 178.

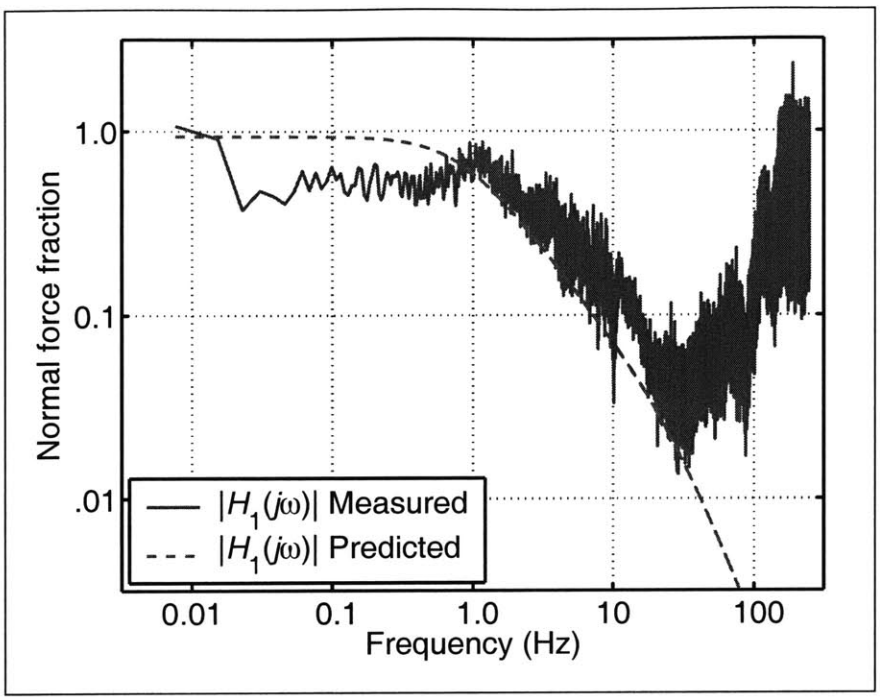

Figure 177: Performance of Suspension Displacement Sensor on Gravel

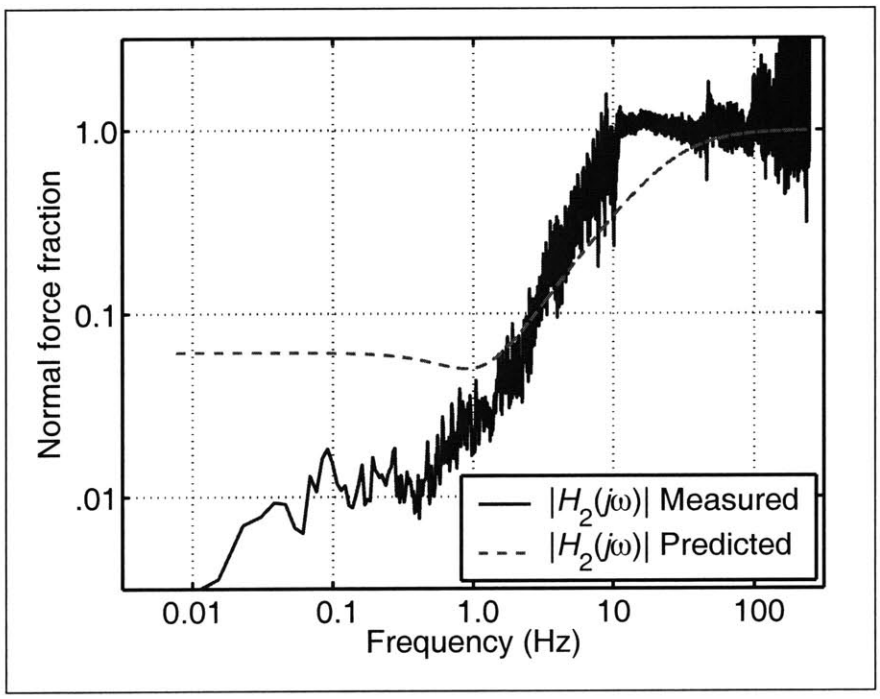

Figure 178: Performance of Wheel Acceleration Sensor on Gravel

In Figure 177 and Figure 178, the experimental measurement of sensor performance agrees qualitatively with the quarter car model predictions that suspension

displacement measures a large fraction of normal force variation for low frequencies and wheel acceleration at high frequencies. There are differences in the cutoff frequencies of each plot and the low-frequency magnitude of suspension displacement. A possible source of these differences is the neglect of roll stabilizer bars in the quarter car model, which are effectively an unmodeled stiffness. A half-car model would be necessary to model this effect. Another possible source of error are nonlinear characteristics of automotive shock absorbers, which are tuned to have different characteristics in compression and extension.

Experimental data is also available for a city driving surface and a harsh testing surface known as an impact road. Sensor performance for these surfaces is given in Figure 179, Figure 180, Figure 181, and Figure 182.

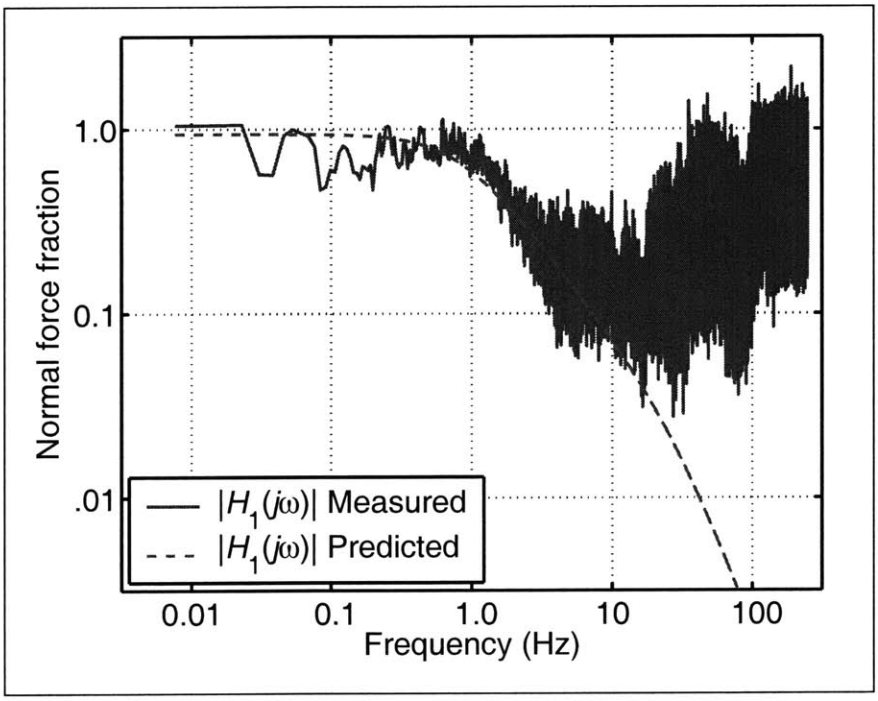

Figure 179: Performance of Suspension Displacement Sensor on City Road

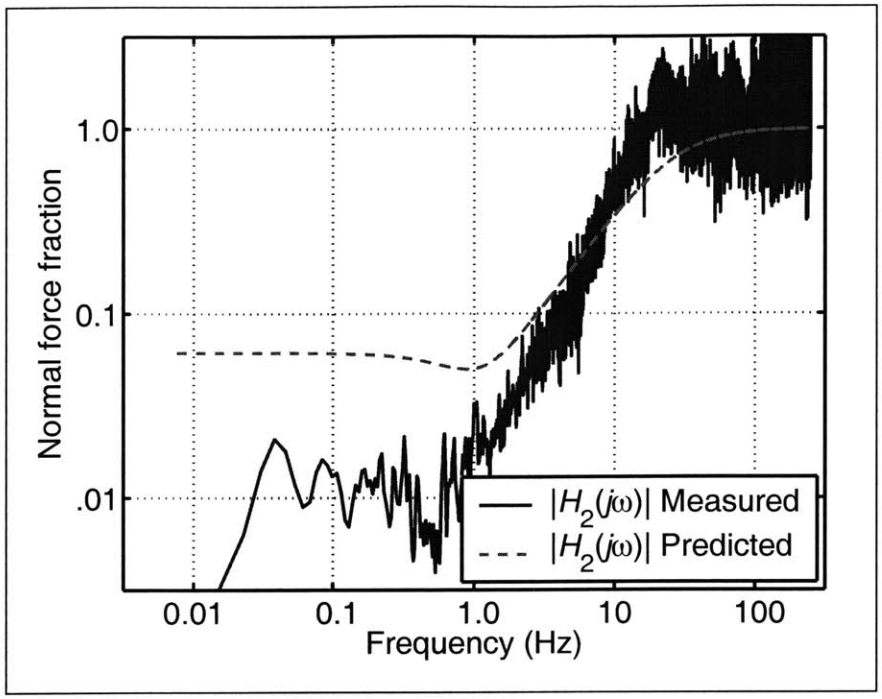

Figure 180: Performance of Wheel Acceleration Sensor on City Road

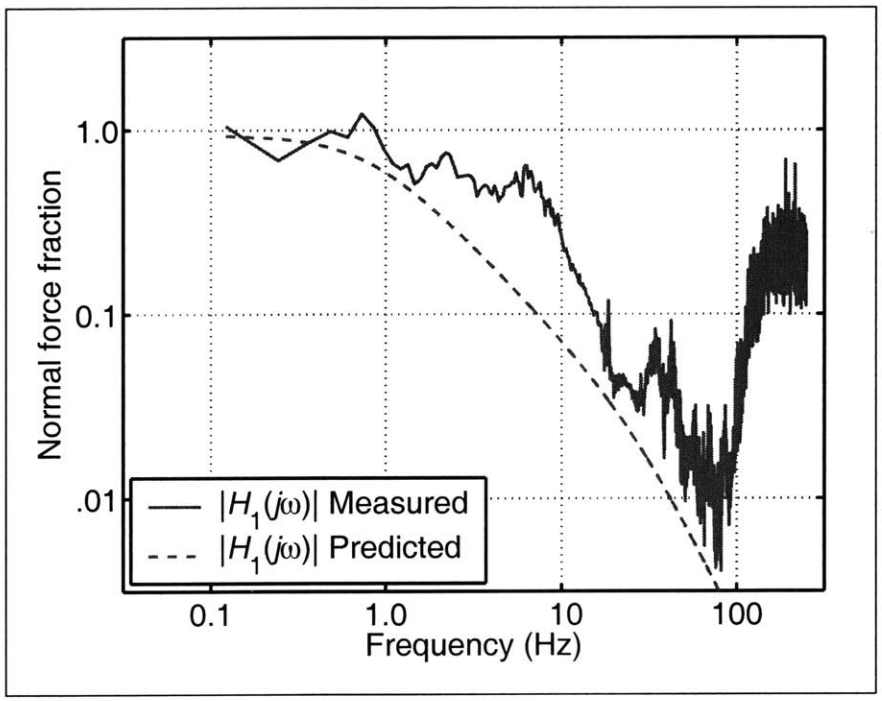

Figure 181: Performance of Suspension Displacement Sensor on Impact Road

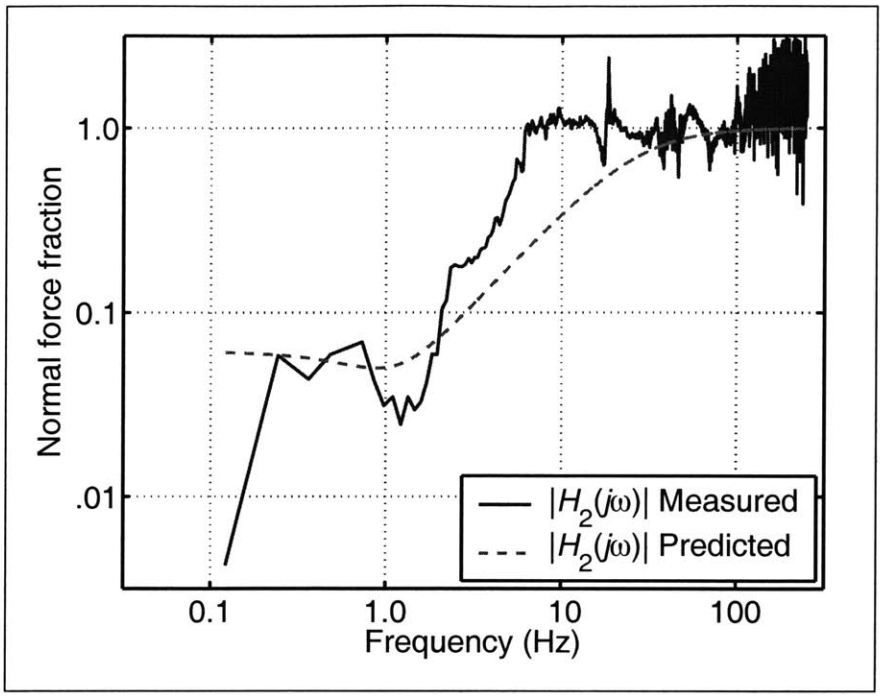

Figure 182: Performance of Wheel Acceleration Sensor on Impact Road

These results indicate that high-frequency normal force variation can be measured with a wheel acceleration sensor. Since the high frequency component of $|H_2(j\omega)|$ is roughly flat, normal force variation can be computed from the wheel acceleration sensor with knowledge of the wheel mass. Note that no inversion of system dynamics is necessary. Future work would involve analysis of a half-car model to consider all the suspension elements or estimation of the road inputs from the normal force response.